The Pennsylvania State University

The Graduate School

Department of Chemistry

Tailoring and Scaling Energetic Aluminum Clusters into Cluster Assembled Materials

A Dissertation in

Chemistry

by

Jordan Cesar Smith

Submitted in Partial Fulfillment
of the Requirements
for the Degree of

Doctor of Philosophy

August 2015

The dissertation of Jordan Cesar Smith was reviewed and approved* by the following:

A. Welford Castleman, Jr.
Eberly Distinguished Chair in Science
Evan Pugh Professor of Chemistry and Physics
Dissertation Adviser
Chair of Committee

Nicholas Winograd
Evan Pugh Professor of Chemistry

John B. Asbury
Associate Professor of Chemistry

Robert Santoro
George L. Guillet, Professor of Mechanical Engineering Emeritus

Barbara J. Garrison
Shapiro Professor of Chemistry
Head of the Department of Chemistry

*Signatures are on file in the Graduate School.

ABSTRACT

As matter decreases in size the importance of a single atom increases exponentially. The properties of clusters, molecules with less than 100 atoms, will change drastically with the addition or removal of a single atom. Clusters have been shown to have properties that mimic other elements and properties that are completely unique. Cluster assemblies could enable the tailoring of precise properties in materials, providing cheap replacements for expensive elements, or novel materials for new applications.

Aluminum clusters show great potential use in many applications including energy and catalysis. This work is focused on gaining a better understanding of how geometry and electronic structure affect aluminum cluster reactivity and how useful clusters might be successfully assembled into materials. The effects of doping aluminum cluster ions with boron atoms are reported and show that the addition of a single boron atom usually stabilizes the cluster while adding more boron atoms results in a breaking of symmetry and destabilization. A new analytical technique, matrix isolation cavity ring-down spectroscopy (MICRDS) was developed to help bridge the gap between gas phase cluster studies and condensed phase cluster materials. Molecules are trapped in an inert matrix and studied using cavity ring-down spectroscopy. MICRDS has the potential to also combine clusters into small stable units that would maintain their advantageous gas phase properties.

TABLE OF CONTENTS

LIST OF FIGURES

LIST OF TABLES

ACKNOWLEDGEMENTS

It is a difficult task to communicate the depth of my gratitude to the people who have helped me reach this point in my life and the following words are meager compared to the feelings in my heart. I would like to start by thanking my advisor, Will Castleman. I admire and marvel at his never-ending excitement for science and vast knowledge and am grateful for his support and counsel during my time as a graduate student. To the other graduate students and post-docs with whom I have worked and collaborated, thank you for your help and advice when problems arose. I must mention and thank Connie Smith, my staff assistant, who always made sure we were taken care of as graduate students. I would like to express my love and deep appreciation to my parents, Bill and Louise, who taught me the value of learning and hard work. I am most grateful to my wife, Jenny, who has supported and encouraged me throughout the last six years. She bolstered me when times were difficult and helped me to always see the bigger picture. I am also grateful to my two boys, Tanner and Alex, who remind me of the beauty of curiosity and that you can succeed as long as you rise each time you fall. There are many other, friends and family; too many to mention here but they will always be remembered. Lastly, I thanks the Air Force Office of Scientific Research and the Office of Naval Research for funding my research at The Pennsylvania State University.

Chapter 1

Introduction

1.1. The Benefits of Scaling Down

As technology advances, new materials with unique and useful properties are being developed to overcome rising challenges in today's society. In 1959, Richard Feynman gave a talk to the American Physical Society about his vision of the future and spoke about the possible ramifications and advancements that could result from a bottom-up approach to material fabrication.[1]

But I am not afraid to consider the final question as to whether, ultimately – in the great future – we can arrange the atoms the way we want; the very atoms, all the way down! What would happen if we could arrange the atoms one by one the way we want them. But we must always accept some atomic arrangement that nature gives us. What could we do with layered structures with just the right layers? What would the properties of materials be if we could really arrange the atoms the way we want them?

Richard Feynman

Though this talk had little influence on the nanotechnology movement that would occur nearly twenty years later, his thoughts mirror the direction that technology has taken in the recent past of working on a smaller and smaller scale. As materials become smaller into the nanometer scale, many new properties emerge that are not observed in the bulk.[2–]

[5] The novel properties found in nanomaterials have already led to new catalysts, electronics, medicines, and other materials (Figure 1.1).[6–8]

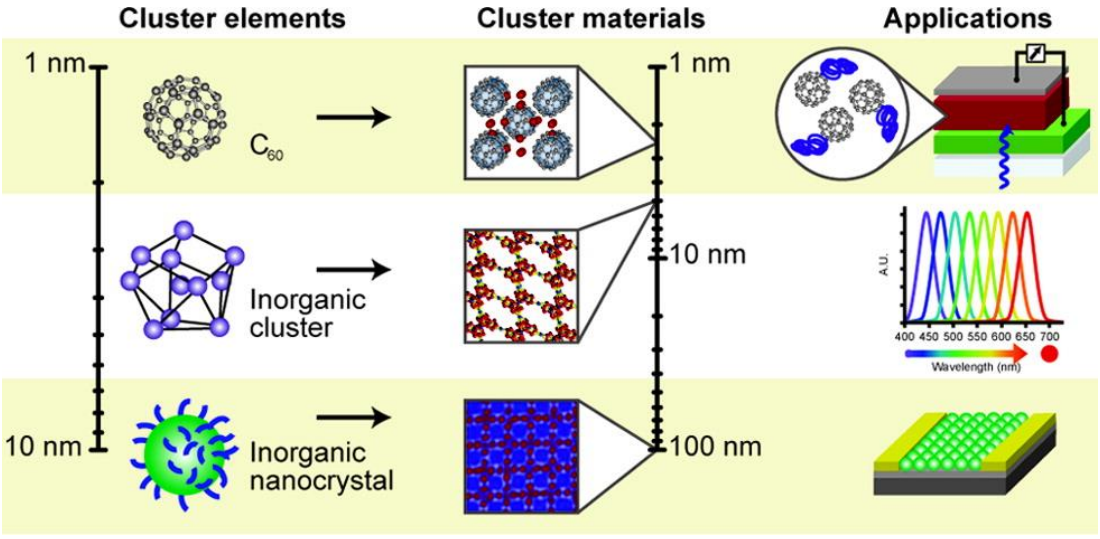

Figure 1.1. Diagram showing possible applications for fullerenes, clusters, and nanoparticles for the development of new materials with tailored materials. Reprinted from reference 8.

The physical properties of a material change significantly in the nanometer regime. As particles decrease in size, the ratio of surface area to volume increases considerably. Consider this example: Cube 1 has dimensions of 1 cm and has a total surface area of 6 cm^2, Cube 2 occupies the same volume as Cube 1 but is made of smaller cubes each with sides of 1 mm and the total surface area becomes 60 cm^2, Cube 3 occupies the same volume as Cube 1 and 2 but is made of smaller cubes each with sides of 1 nm and the total surface area becomes 60,000,000 cm^2 (Figure 1.2).[9] As the surface atoms represent a larger percentage of the overall composition of the particle, the chemistry of the particle deviates from properties seen in the bulk. This dramatic increase in surface area leads to lower melting points, increased reactivity potential, and other novel nano-properties.[10]

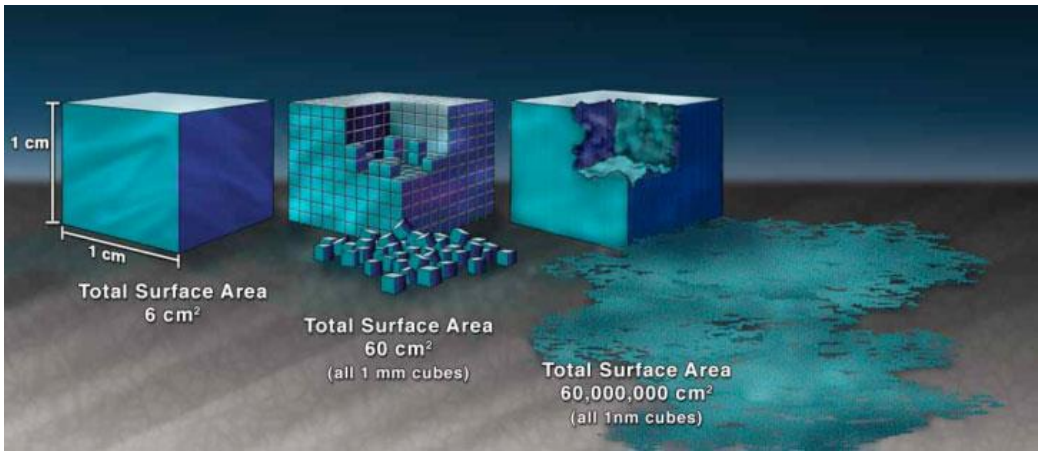

Figure 1.2. Illustration showing the drastic differences in surface area between the macro, micro, and nano scales. Reprinted from reference 9.

In addition to the changes caused by the increasing surface to volume ratio, the actual size of a nanoparticle will govern certain properties. These properties are due to quantum confinement of the electrons in the nanoparticle which begin to resemble "particles-in-a-box".[10] This confinement results in a host of new optical properties that are mainly governed by the size of the particle. Size-dependent properties are not only limited to optical applications but can extend to catalytic, magnetic, energetic, and other applications. Small nanoparticles of less than 100 atoms exemplify the breadth of possibilities that arise from size-dependent properties where the difference of a single atom can significantly alter the characteristics of a nanoparticle. These small nanoparticles are distinguished from larger nanoparticles by using the term cluster.

1.2. Cluster Basics

Across many fields of discipline, the term cluster can have many different meanings depending on context from computer servers to explosive grenades. In this work, the term cluster refers to covalently bound molecules (from 2-50 atoms) that exhibit distinct properties from the singular elemental atom and its corresponding bulk material. Not only are cluster properties distinct from those of atoms or molecules, but the properties of clusters are non-scalable in that, the removal or addition of an atom may drastically alter the properties of the cluster. It can be difficult to truly tell when a collection of atoms ceases to exhibit molecular traits and enters the cluster size regime and also when the material becomes large enough that its traits begin to assume those of the bulk material. As each element and the bonds between them are slightly different, those limits will be dependent upon the composition of the material. Aluminum, for example, has been predicted to deviate from its traditional monovalent state (one p-orbital electron) to its trivalent state (three s-p hybridized electrons found in clusters) at varying sizes: Al_3, Al_4, Al_6, Al_7, Al_8, and Al_9.[11–17] On the other end, it has been found that aluminum clusters with 20 or more atoms begin to adopt some bulk properties where the geometric structure may become more significant than the electronic structure and the effects of the difference of one atom are less substantial.[18]

Cluster chemistry provides a bridge between the chemistry of atoms and bulk material.[19–21] Figure 1.3 shows how the electronic structure evolves as a material increases in size from a single atom to the bulk.

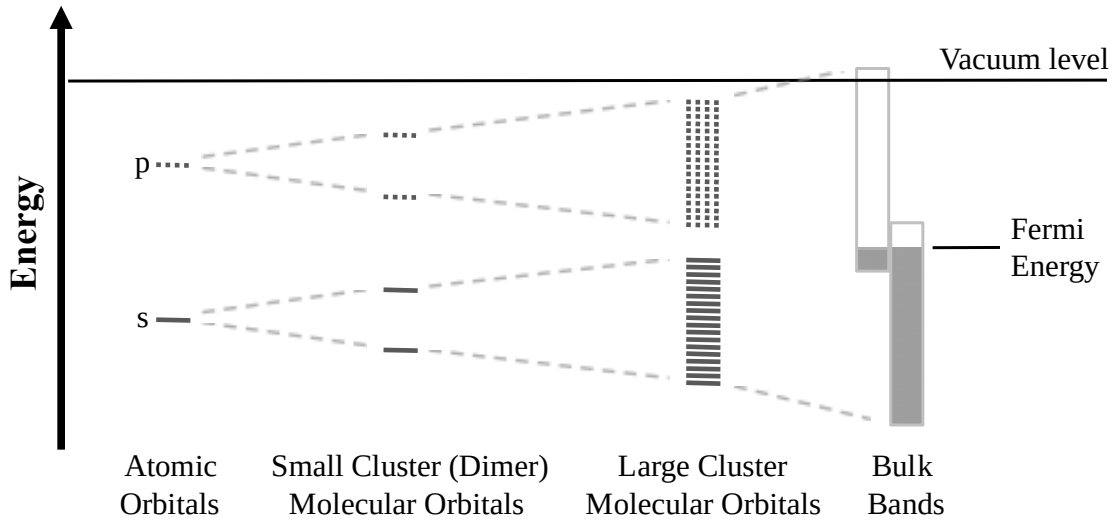

Figure 1.3. Diagram showing the evolution of electronic orbitals from atomic orbitals, to molecular orbitals, to bulk electronic bands. The density of states increases as the particle size increases until in the bulk, a pseudo-continuous density of states is observed. Reprinted from reference 11.

The properties of a cluster are governed by both its electronic and geometric structures. The impact of each structures is dependent upon many factors; however, as the density of states increases from well separated to nearly continuous energies, the electronic structure becomes less critical and the effects of the geometric structure gain prominence. The clusters studied in this work fall in the middle of this continuum, where there may be many orbitals but they are far from continuous.

As metal clusters began to gain interest in the early 1980's, it was found that the existing theoretical methods were insufficient to properly describe the electronic structure of clusters. In 1984, a study led by Walter Knight at the University of California, Berkeley, observed irregularities of the intensities in a mass spectrum of sodium clusters (from 2-100

atoms).[22] Figure 1.4 shows large differences in the mass intensities after certain sodium clusters: Na_8, Na_{20}, Na_{40}, and Na_{58}.

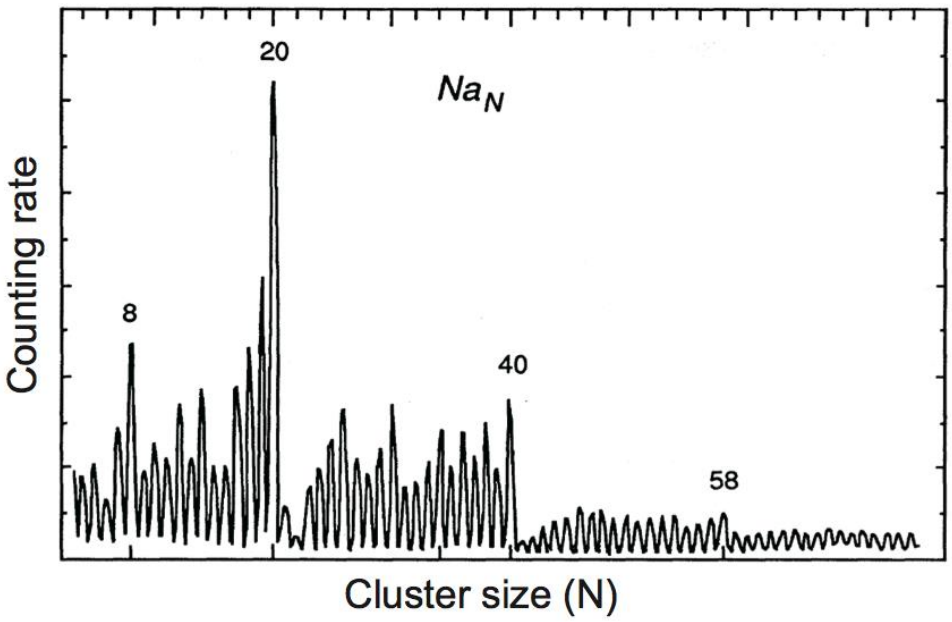

Figure 1.4. A mass spectrum of sodium clusters formed by supersonic expansion. Notice the large intensity peaks indicating enhanced stability (magic clusters) for specific Na_m clusters where m=8, 20, 40, and 58. Adapted from reference 22.

Notice the enhanced intensity of the stable "magic" clusters Na_8, Na_{20}, Na_{40}, and Na_{58}, and the steep drop-off of intensity for the clusters following each magic cluster. Knight et al. found that the sodium clusters followed the one-electron shell model and that each of the ultra-stable clusters had electronic structures with closed valence shells analogous to noble gases. This was a noteworthy observation because previous studies of noble-gas structures had all attributed the enhanced stability of certain clusters over other as being due to structural packing and not electronic structure.[23–25] Knight's sodium work was the first to observe this unique stability pattern in small metallic clusters and created a new field of

study: metal clusters.[26] The size-dependent stability was explained using the one electron shell model which had been used previously by Cini in 1975 and Ekardt in 1984 to predict the electronic structure of clusters though without the broader scope of Knight's work.[27,28] The one-electron shell model, better known as the jellium model remains the most common method for the treatment of all-metal cluster electronic structures.

1.3. The Self-Consistent Jellium Model

The jellium model is widely used to explain the electronic structure of clusters. There are three main assumptions that govern the jellium model including 1) that an atom's valence electron is delocalized over the entire cluster, 2) that the electron-core interactions result in a smooth potential curve, and 3) that the cluster is spherical.[29] Briefly, this model describes clusters as having a homogeneous positive core surrounded by shells of delocalized valence electrons.[30] This description is the basis of the unified atom theory where clusters are analogous to atoms (sometimes referred to as superatoms) in terms of their filled electron shells. A cluster with a filled valence shell will be unreactive in ways similar to a noble gas; clusters lacking one electron in the valence shell are comparable to halogens, and so forth. Previous studies of the diffusion of neutral sodium atoms in an argon matrix have shown that sodium atoms agglomerate to form valence-filled stable (magic) clusters according to the predictions made in the jellium model instead of intermediate clusters with less stable electronic configurations.[30]

To better explain the jellium model and its treatment of cluster electrons, one must first delve into quantum mechanics and consider the Hamiltonian ($\widehat{H}$) in the time-independent Schrodinger equation.

$$\widehat{H}\,\Psi = E\,\Psi \tag{1.1}$$

The exact nonrelativistic Hamiltonian for a neutral cluster with N atoms and Z electrons for each atom is

$$\widehat{H} = \sum_{\alpha} \frac{\Delta_{\alpha}^2}{2M} + \sum_{i} \frac{\Delta_{i}^2}{2} + \sum_{\alpha \neq \beta} \frac{1}{2} \frac{Z^2}{|R_{\alpha} - R_{\beta}|^2} - \sum_{\alpha,i} \frac{Z}{|r_i - R_{\alpha}|} + \frac{1}{2} \sum_{i \neq j} \frac{1}{|r_i - r_j|} \tag{1.2}$$

where α and β refer to a nucleus, i and j refer to electrons, M is the mass of a nucleus, and R and r refer to positions of a nucleus and electron, respectively. The summations run over the indexed nuclei (α, β) and electrons (i, j) of all atoms (N) and electrons (Z). The first two terms of equation 1.2 represent the nuclear and electronic kinetic energies respectively, while the third and fifth terms represent the potential energy from the coulomb repulsion between the nuclei (third) and the coulomb repulsion of the electrons (fifth), and the fourth term represents the coulomb attraction between the electrons and the nuclei. As is apparent for all except the most ambitious of mathematicians, solving this Hamiltonian is impossible for anything but the simplest elements. However, by understanding the 5 terms in the equation, the Hamiltonian may be simplified.

In 1927 Max Born and J. Robert Oppenheimer introduced the Born-Oppenheimer approximation.[31] The approximation relates how the charges associated with the nucleus and the electrons affect the motion of the nucleus and electrons. Electrons and nuclei are attracted to each other by the same magnitude of charge; however, the nucleus is

significantly larger with larger mass. The forces and momentum that act on the nucleus and electrons will be the same but the difference in mass will result in a negligible velocity of the nucleus. The first simplification is made by applying the Born-Oppenheimer approximation and neglecting the terms that deal solely with the nuclei. This leaves the three terms representing the kinetic energy of the electrons, the coulomb attraction between the electrons and nucleus, and the coulomb repulsion between the electrons.

$$\widehat{H_e} = \sum_i \frac{\Delta_i^2}{2} - \sum_{\alpha,i} \frac{Z}{|r_i - R_\alpha|} + \frac{1}{2}\sum_{i \neq j} \frac{1}{|r_i - r_j|^2} \tag{1.3}$$

Once the motion of the nuclei and electrons are separated, we are essentially left with the electronic Hamiltonian but further simplification is necessary.

The next step is to separate the valence from the core electrons.[32–34] This approximation is most accurate for cases where the valence electrons are strongly delocalized from the nucleus, such as alkali metals. The core electrons are combined with the nucleus and now can be considered a charged core which will revise the Hamiltonian terms with new interactions such as kinetic energy of valence electrons, coulomb attractions between valence electrons and the charged core, and coulomb repulsion between valence electrons. The electron-nucleus interaction term must be modified by more than just definition. This can be done by replacing the electron-nucleus interaction with a new term to describe the interaction between a valence electron and the new charged core represented by equation 1.4.

$$V_c(\mathbf{r}_i) = \sum_{\alpha=1}^{N} V_p(|\mathbf{r}_i - \mathbf{R}_\alpha|) \tag{1.4}$$

When the second term is simplified by eq. 1.4, the electronic Hamiltonian is simplified to

$$\widehat{H_e} = \sum_i \frac{\Delta_i^2}{2} + \sum_i V_c(\mathbf{r}_i) + \frac{1}{2}\sum_{i \neq j} \frac{1}{|r_i - r_j|^2} \quad (1.5)$$

where the summations now run over only the valence electrons (i, j) rather than all electrons. Knight's contribution to this approximation is that he simplified eq. 1.4 by assuming the potential, V_p, was a spherically symmetric pseudopotential, V_{ps}, which is the heart of the jellium approximation.[22,35]

$$V_{ps}(r) = \frac{V_o}{1 + e^{(r - r_o)/\epsilon}} \quad (1.6)$$

Rather than considering each ionic core individually, the cores of each atom are combined into larger positive core of the cluster and the valence electrons of each atom are delocalized over this new jellium core. It is this idea that gives rise to the idea of the unified atom or "superatom" concept where the properties of a cluster can show remarkable similarities to those of an atom (Figure 1.5).

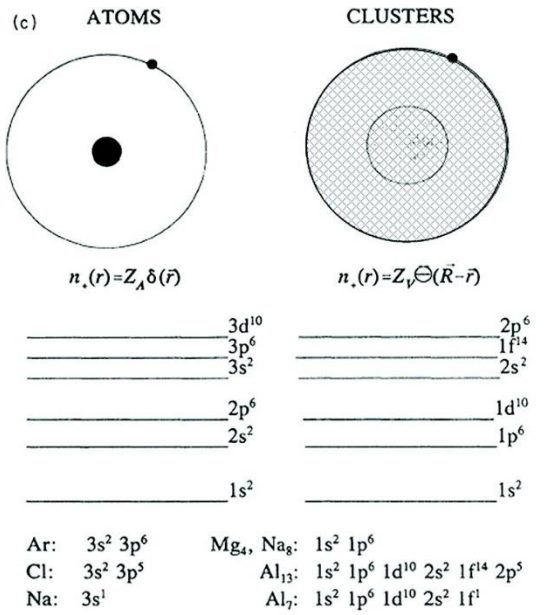

Figure 1.5. A comparison of the electronic structure of atoms and clusters showing the electron orbitals. The bottom shows corresponding elements and clusters that have analogous electron configurations. Adapted from reference 36.

Returning to eq. 1.5, complications still exist in finding the solutions of the Hamiltonian but there is one more modification that can be made to further simplify the equation. The third term in eq. 1.5 represents the electron-electron coulomb repulsion; however, this can be simplified by taking all of the inter-electron interactions and combining them into a single averaged potential, $\tilde{V}(r_i)$, where each individual electron moves independently from one another and is only influenced by the average potential.[32,33] This adjustment is called the mean-field approximation or self-consistent field approximation and is the focus of density functional theory and Hartree-Fock calculations.[26]

Returning to Knight's work on sodium clusters, he was able to correlate the stable sodium clusters with the predicted valence shell closings provided by the self-consistent jellium

model (Figure 1.6) The shell closings are very similar to atomic shell closings except that clusters will include higher orders of angular momenta, L (i.e. d, f, g, h), and larger degeneracies within those angular momenta, $2(2L+1)$ than are generally encountered with common elements. The following references present a more detailed and extensive derivation of the calculations used for treating clusters for those readers that desire further information.[34,37]

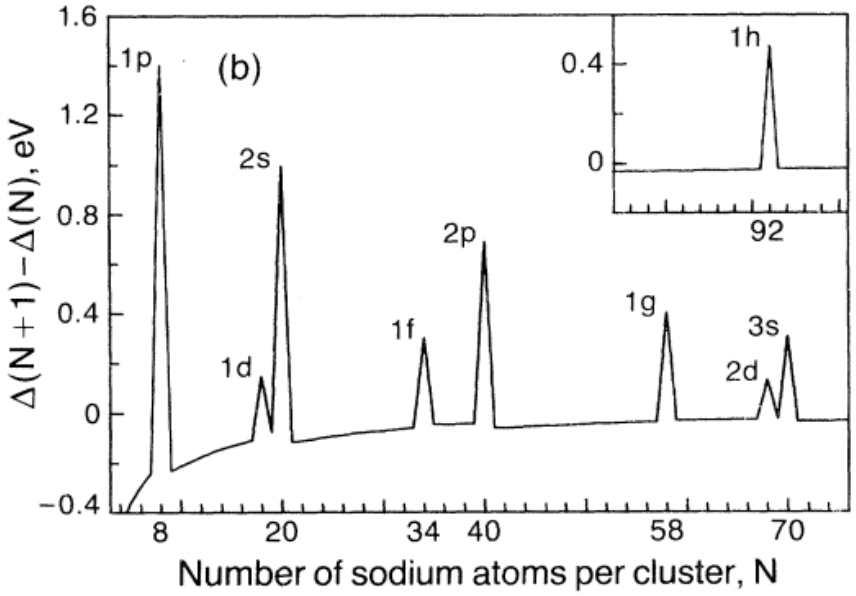

Figure 1.6. Graph showing the change in the electronic energy difference between adjacent clusters. The labeled peaks show those sodium clusters that match the filled valence shells predicted by the jellium model. Adapted from reference 22.

The mathematical treatment for clusters still relies heavily on the findings of Knight's work; however, advancements have been made as more complicated systems are explored. The assumption of using a spherically symmetrical pseudopotential may work

very well for those clusters that resemble spheres (jellium shell closings), but not every cluster will have a spherical geometry and as the geometry deviates from a sphere other models and approximations must be included for accurate theoretical results. Clemenger, one of Knight's co-researchers on the sodium work, provided a correction called the distortion parameter for non-spherical clusters.[38]

When clusters have only partially filled electronic shells, the geometry compensates to minimize the internal energy. These geometries were explained by two scientists, Hermann Jahn and Edward Teller, in the 1930s.[39] Now termed Jahn-Teller distortions, when degenerate orbitals are only partially filled, the molecule/cluster deforms in order to maximize the number of orbitals that can be filled completely. For example, three degenerate p-orbitals will alter their geometry to optimize the orbital energies and maximize the number of filled orbitals. This can result in either oblate or prolate geometries which lower the energy of the occupied orbital(s) and raise the energy of the unoccupied orbitals (figure 1.7).

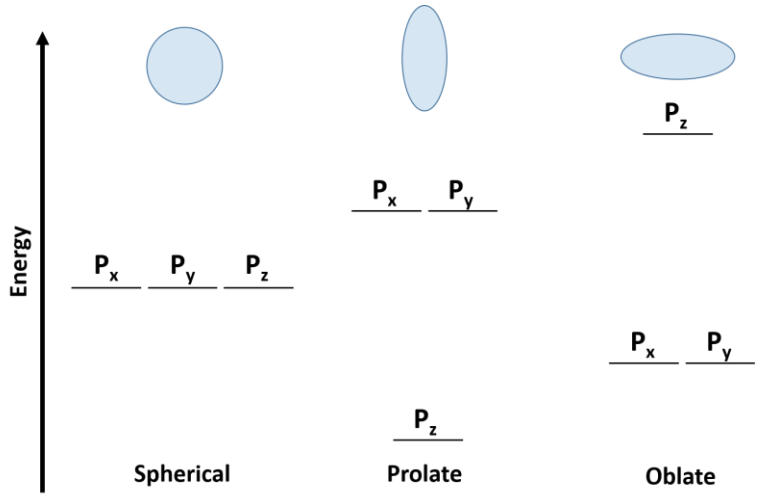

Figure 1.7. Diagram showing the Jahn-Teller distortion of p-orbitals in order to optimize the energy in a molecule or cluster that has an unfilled valence shell.

Clemenger started his approach by using a shell theory developed by Sven Nilsson that successfully described axially symmetric distortions in nuclei and applied the theory to clusters.[40] Using a distortion parameter, δ, Clemenger was able to predict sub-shell closings that matched the marginally enhanced cluster intensities (those intensities attributed to clusters such as Na_{14}, Na_{18}, Na_{26}, etc. rather than those that were considered magic such as Na_8, Na_{20}, etc.) The Clemenger-Nilsson model accurately predicts the basic shape of the cluster whether it be spherical (δ=0, prolate (δ>0), or oblate (δ<0), and correlated a changing of the sign of δ to be an altering of the electronic and geometric structure between oblate and prolate.

1.4. Cluster Research: Applications and Motivations

Beginning with Antoine Lavoisier, a French chemist who died in the latter half of the 18th-century, published the first list of chemical elements, to Mendeleev, a Russian chemist in the 19th-century, who organized the first periodic table of elements, chemists have organized elements according to their properties and characteristics.[41] Today we have a periodic table with 118 elements (though some of those elements are still unconfirmed) arranged in groups and periods organizing them by their chemical and physical properties. In 2006 and again in 2009, Castleman and Khanna proposed that valence shell similarities found between clusters and elements introduces a new (third) dimension to the periodic table of elements which correlates clusters and elements that share similar properties (Figure 1.8).[36,42]

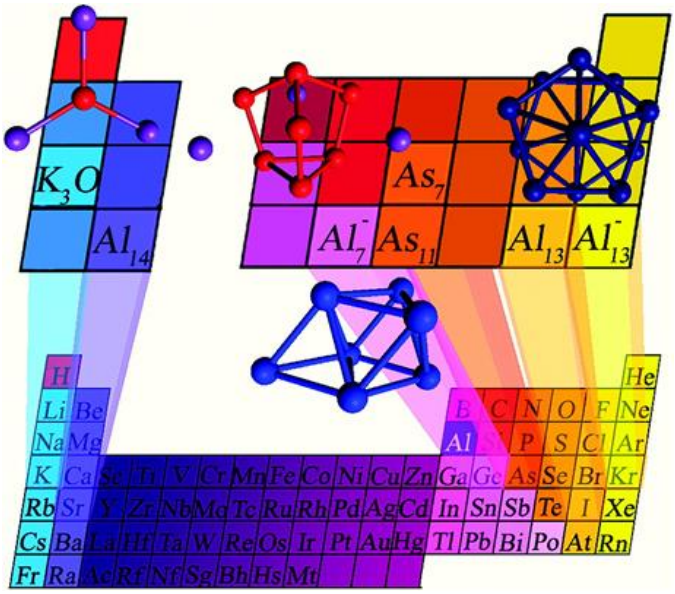

Figure 1.8. Conceptual drawing of a three-dimensional periodic table of elements. Clusters showing similar properties to those groups and periods of the table are considered superatoms and arranged accordingly. Adapted from reference 36.

The clusters included in Fig. 1.8 show various examples of clusters that mimic the properties of elements. Clusters have been shown to mimic halogens, alkali metals, noble gases, etc. in many traits ranging from reactivity, magnetism, ionization potentials, electron affinities, and more.[43–50] In addition to clusters that mimic the properties of elements, some clusters display traits that are completely unique such as fullerenes.[8] Clusters that exhibit traits that mimic other elements or that are completely unique open wide the possibilities for use in innovative materials. Clusters could enhance the next generation of new materials with novel properties or serve as cheap replacements for currently expensive materials.

One particular area of interest for cluster applications is in energy production. Metal nanoparticles already play a role as fuel additives and as explosive material because of their high energy density and the ability to tailor the combustive properties of the fuel by way of the nanoparticles.[51–53] Metal nanoparticles best suited as high-energy-density materials are most often composed of aluminum, magnesium, boron, or a mixture of these elements. Aluminum and boron can generate up to three or four times the amount of heat as TNT or RDX (RDX is the main ingredient in many of the military grade explosives such as C-4).[54]

Table 1.1 Combustion properties of energetic materials. Adapted from reference 54.

Material	Density, 10^{-3} kg/m^3	Heat of Detonation (ΔH_d) GJ/m^3	Detonation velocity, km/s
TNT	1.6	7.6	6.7
RDX	1.77	11.2	8.7
HMX	1.89	11.7	9.1
CL20	1.96	12.2	9.2
Boron	~1.8	~30	
Aluminum	~2.0	~30	

With the massive amounts of energy stored in aluminum, it appears counterintuitive that everything from beverage containers to buildings to aircraft are built from such an energetic material. There are three main factors that help make aluminum an ideal material for consumer products. First, it is the third most abundant element on Earth after silicon and oxygen. Its abundance leads to its low manufacturing cost though the refining process that resulted in its low cost and widespread use was only developed within the last 130 years.[55] Second, it is a lightweight metal that in its pure form is somewhat malleable; however, alloyed with other metals such as copper it forms a strong, lightweight material suitable for building aircraft. Third, aluminum naturally has an oxide layer that spontaneously forms when it is exposed to air. Regardless of the size of the aluminum particle, 10 nm or 10 mm, the oxide layer is generally 3 nm thick.[54] This oxide coating, rust, is what protects the remainder of the aluminum from degrading and enhances the

lifespan of aluminum structures compared to other metals, say steel. When steel rusts the oxide layer begins to flake which exposes more of the steel and if not prevented will continue until the entire structure is oxidized and loses its strength and integrity.

Though the strong oxide layer is vital to the structural durability and versatility of aluminum in consumer products, it is unfavorable when looking at the energy potential of the metal. Any portion of the particle that has oxidized is immediately useless energetically and requires additional energy in order to remove it and expose the unoxidized aluminum underneath. If the aluminum particles were large, say in the micrometer range, the surface atoms (those that are already oxidized) would only account for a small percentage of the overall particle (<0.1%). Recall the exponential increase of the surface area to volume shown in Figure 1.2 and the amount of deadweight aluminum reaches 50% for a 30 nm particle and nearly 100% oxidation for particles under 10 nm. This drawback to using small aluminum nanoparticles has resulted in further studies that explore different processes to prevent spontaneous oxidation of the particles. Examples of some promising methods include the addition of a passivated layer of ligands and the finding of oxidation resistant sizes/geometries.[56–58]

Returning to Feynman's quote at the beginning of this chapter, "*What would the properties of materials be if we could really arrange the atoms the way we want them?*" The integration of clusters into materials approaches the vision described by Feynman nearly a half century ago where the properties of a material could be tailored by arranging or altering the atomic composition by increments of only a few atoms. There are three main challenges that hinder the progress of cluster assembled materials. First, the ongoing identification of

clusters with desirable properties. Second, maintaining the geometric and electronic integrity of each cluster when brought into close proximity and begin to interact with other clusters and molecules. Third, the development of new methods for cluster synthesis and construction of the cluster assembled materials. Many research teams focus on one or all of these three issues and the goal of cluster assembled materials comes ever closer.[8,59–64]

The first challenge will never truly be completed as there are a myriad of cluster species and various properties that it will require some time before we gain a comprehensive knowledge of each. Conducting studies for each cluster species for every property is a daunting task and might be more fruitful if a targeted approach was taken. This is why theoretical models and a thorough fundamental understanding of cluster chemistry is needed. The ability to accurately predict which clusters could provide specific properties is a much better approach than simply trial and error every possibility. Great progress has been achieved for both developing models and theory to predict desirable clusters and in experimental determination of appropriate clusters for use in materials.[43,48,63,65]

The second challenge often arises because most cluster studies are conducted in the gas phase where each cluster is isolated from interactions from other clusters. The geometry and electronic structure of a cluster can vary widely between the gas and condensed phases. In one study, Nacer et al. performed molecular dynamics simulations of the deposition of 3-dimensional silver clusters onto a palladium surface at zero impact kinetic energy.[66] Despite ideal nondestructive conditions, deformation of the original clusters still occurred. Problems associated with cluster-cluster interactions include

aggregation of clusters when brought together or simply a change in the chemistry when bonded to another cluster or molecule. Attempts to maintain the original cluster properties in the presence of outside interactions ranges from various deposition techniques to the application of a protective ligand coatings.[67–69] Examples of cluster assemblies that could act as stable building blocks in new materials have been proposed by various groups, with a common thread of using large cation and anion cluster motifs to form stable cluster salts shown in Figure 1.9.[36,47]

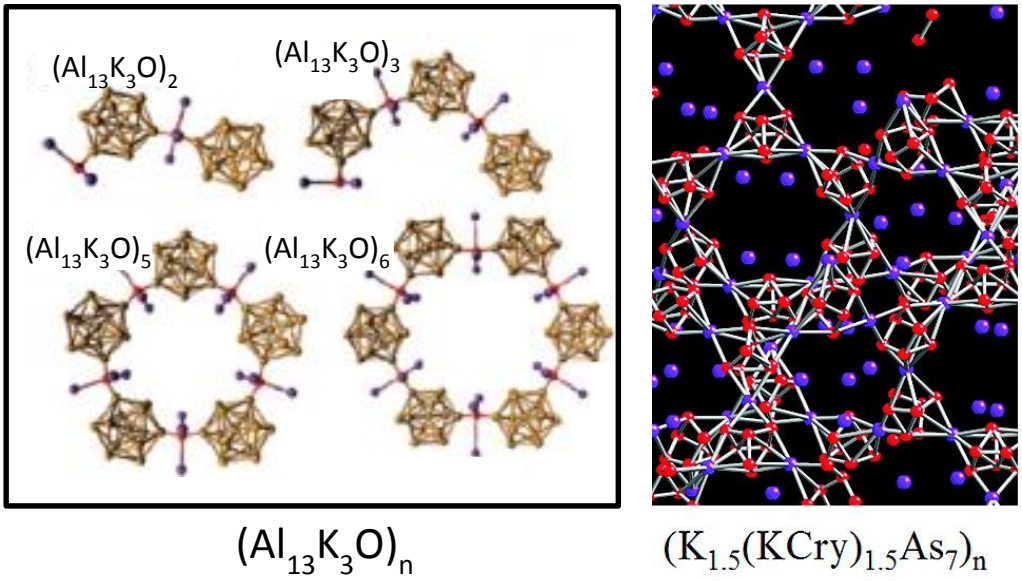

Figure 1.9. Theoretical representations of stable cluster building blocks. The left assemblies are made of $Al_{13}K_3O$ units that allow the energy-dense aluminum clusters to be paired with an oxidizer for combustion purposes. The right assemblies show an arsenic cluster paired with an alkali atom that shows semiconductor character. The band gap can be tuned by changing the alkali metal. Adapted from references 36 and 47.

The last challenge may or may not be solved in conjunction with the second challenge. There are two difficulties that arise when constructing the cluster assembled

material: the interaction problems (second challenge) and the quantities of clusters that can be made. Most gas phase cluster studies utilize similar methods as cluster sources (discussed in section 2.2). Though these cluster sources are very reliable, they often only make small quantities of clusters (~10^9 clusters per second or one mole in 3 x 10^6 years). There are other cluster formation methods, such as liquid synthesis, but with rare exception they often lack the mass selection finesse found in gas phase cluster research.[70–72] The production values may vary between sources and methods and the needs will vary between various material applications (e.g. needing kilogram amounts of clusters vs. only needing nanometer thin layers). This challenge could prove to be the smallest obstacle as when the need arises for methods to mass produce clusters for materials, the innovations will occur. This foretelling will only be validated or repudiated with time.

1.5. Outline of Dissertation/Present Research

The information above was intended to provide a brief summary of cluster chemistry and the obstacles that still remain. The focus of this dissertation is the application of clusters as high-energy-density materials, specifically aluminum and boron. The research focuses on aluminum and aluminum boride cluster reactivity and also the development of a new instrument to help bridge the gap between gas-phase studies and condensed-phase materials. The dissertation continues with an explanation of the experimental apparatus in Chapter 2. The experimental chapter includes alternative components used in other instruments to provide a general understanding of cluster instrumentation and the associated benefits and disadvantages. Chapter 3 describes the

process of making aluminum boride cluster anions ($Al_nB_m^-$) and compare their reactivity with molecular oxygen with that of pure aluminum cluster anions (Al_n^-). Chapter 4 describes the development of a new analytical technique called matrix isolation cavity ring-down spectroscopy (MICRDS). Concluding remarks regarding this work and the future direction of clusters studies are included in Chapter 5. An appendix is included which details the design and construction of two components of the MICRDS setup.

1.6. References

(1) Feynman, R. There's Plenty of Room at the Bottom, 1959.
(2) Gupta, A. K.; Gupta, M. Synthesis and Surface Engineering of Iron Oxide Nanoparticles for Biomedical Applications. *Biomaterials* **2005**, *26* (18), 3995–4021.
(3) Gao, X. H.; Cui, Y. Y.; Levenson, R. M.; Chung, L. W. K.; Nie, S. M. In Vivo Cancer Targeting and Imaging with Semiconductor Quantum Dots. *Nat. Biotechnol.* **2004**, *22* (8), 969–976.
(4) Law, M.; Greene, L. E.; Johnson, J. C.; Saykally, R.; Yang, P. D. Nanowire Dye-Sensitized Solar Cells. *Nat. Mater.* **2005**, *4* (6), 455–459.
(5) Sun, S. H.; Murray, C. B.; Weller, D.; Folks, L.; Moser, A. Monodisperse FePt Nanoparticles and Ferromagnetic FePt Nanocrystal Superlattices. *Science* **2000**, *287* (5460), 1989–1992.
(6) Stix, G. Nanotechnology Is All the Rage. but Will It Meet Its Ambitious Goals? And What the Heck Is It? *Sci. Am.* **2001**, *285* (3), 32–37.
(7) Demming, A. The State of Research After 25years of Nanotechnology. *Nanotechnology* **2013**, *25* (1), 010201–010201.
(8) Claridge, S. A.; Castleman Jr., A. W.; Khanna, S. N.; Murray, C. B.; Sen, A.; Weiss, P. S. Cluster-Assembled Materials. *Acs Nano* **2009**, *3* (2), 244–255.
(9) National Nanotechnology Initiative, What's so Special about the Nanoscale? Www.nano.gov/nanotech-101/special (accessed Jan 15, 2015.
(10) Kruis, F. E.; Fissan, H.; Peled, A. Synthesis of Nanoparticles in the Gas Phase for Electronic, Optical and Magnetic Applications - a Review. *J. Aerosol Sci.* **1998**, *29* (5-6), 511–535.
(11) Melko, J. J.; Castleman Jr., A. W. Photoelectron Imaging of Small Aluminum Clusters: Quantifying S-P Hybridization. *Phys. Chem. Chem. Phys.* **2013**, *15* (9), 3173–3178.

(12) Meier, U.; Peyerimhoff, S.; Grein, F. Abinitio Mrd-Ci Study of Neutral and Charged Ga-2, Ga-3 and Ga-4 Clusters and Comparison with Corresponding Boron and Aluminum Clusters. *Z. Phys. -At. Mol. Clust.* **1990**, *17* (3), 209–224.
(13) Li, X.; Wu, H. B.; Wang, X. B.; Wang, L. S. S-P Hybridization and Electron Shell Structures in Aluminum Clusters: A Photoelectron Spectroscopy Study. *Phys. Rev. Lett.* **1998**, *81* (9), 1909–1912.
(14) Kawamata, H.; Negishi, Y.; Nakajima, A.; Kaya, K. Electronic Properties of Substituted Aluminum Clusters by Boron and Carbon Atoms (AlnBm-/AlCm-); New Insights into S-P Hybridization and Perturbed Shell Structures. *Chem. Phys. Lett.* **2001**, *337* (4-6), 255–262.
(15) Gantefor, G.; Eberhardt, W. Shell Structure and S-P Hybridization in Small Aluminum Clusters. *Chem. Phys. Lett.* **1994**, *217* (5-6), 600–604.
(16) Akola, J.; Hakkinen, H.; Manninen, M. Ionization Potential of Aluminum Clusters. *Phys. Rev. B* **1998**, *58* (7), 3601–3604.
(17) Sommerfeld, T. Al-4(-) Cluster Anion: Electronic Structure, Excited States, and Electron Detachment. *J. Chem. Phys.* **2010**, *132* (12), 124305.
(18) Reber, A. C.; Roach, P. J.; Woodward, W. H.; Khanna, S. N.; Castleman Jr., A. W. Edge-Induced Active Sites Enhance the Reactivity of Large Aluminum Cluster Anions with Alcohols. *J. Phys. Chem. A* **2012**, *116* (30), 8085–8091.
(19) Castleman Jr., A. W.; Jena, P. Clusters: A Bridge between Disciplines. *Proc. Natl. Acad. Sci. U. S. A.* **2006**, *103* (28), 10552–10553.
(20) Reber, A. C.; Khanna, S. N.; Castleman Jr., A. W. Superatoms: From Motifs to Materials. In *Nanoclusters: A Bridge Across Disciplines*; Jena, P., Castleman Jr., A. W., Eds.; 2010; pp 365–381.
(21) Jena, P.; Castleman Jr., A. W. Introduction to Atomic Clusters. *Nanoclusters Bridge Discip.* **2010**, 1–36.
(22) Knight, W. D.; Clemenger, K.; Deheer, W. A.; Saunders, W. A.; Chou, M. Y.; Cohen, M. L. Electronic Shell Structure and Abundances of Sodium Clusters. *Phys. Rev. Lett.* **1984**, *52* (24), 2141–2143.
(23) Stephens, P.; King, J. Experimental Investigation of Small Helium Clusters - Magic Numbers and the Onset of Condensation. *Phys. Rev. Lett.* **1983**, *51* (17), 1538–1541.
(24) Echt, O.; Sattler, K.; Recknagel, E. Magic Numbers for Sphere Packings - Experimental-Verification in Free Xenon Clusters. *Phys. Rev. Lett.* **1981**, *47* (16), 1121–1124.
(25) Ding, A.; Hesslich, J. The Abundance of Ar and Kr Microclusters Generated by Supersonic Expansion. *Chem. Phys. Lett.* **1983**, *94* (1), 54–57.
(26) Ekardt, W. *Metal Clusters*; Wiley & Sons: New York, NY, 1999.
(27) Cini, M. Ionization-Potentials and Electron Affinities of Metal Clusters. *J. Catal.* **1975**, *37* (1), 187–190.
(28) Ekardt, W. Work Function of Small Metal Particles - Self-Consistent Spherical Jellium-Background Model. *Phys. Rev. B* **1984**, *29* (4), 1558–1564.
(29) Bartels, C. Angular Distributions of Photoelectrons from Cold, Size-Selected Sodium Cluster Anions. PhD Dissertation, Albert-Ludwigs-University of Freiburg: Freiburg im Breisgau, Germany, 2008.

(30) Kornath, A.; Zoermer, A.; Ludwig, R. Formation of the Magic Cluster Na-8 in Noble Gas Matrixes. *Inorg. Chem.* **2002**, *41* (24), 6206–6210.
(31) Born, M.; Oppenheimer, R. Quantum Theory of Molecules. *Ann. Phys.* **1927**, *84* (20), 0457–0484.
(32) Beck, D. Self-Consistent Calculation of the Polarizability of Small Jellium Spheres. *Phys. Rev. B* **1984**, *30* (12), 6935–6942.
(33) Beck, D. Self-Consistent Calculation of the Electronic-Structure of Small Jellium Spheres. *Solid State Commun.* **1984**, *49* (4), 381–385.
(34) Brack, M. The Physics of Simple Metal-Clusters - Self-Consistent Jellium Model and Semiclassical Approaches. *Rev. Mod. Phys.* **1993**, *65* (3), 677–732.
(35) Knight, W.; Deheer, W.; Saunders, W.; Clemenger, K.; Chou, M.; Cohen, M. Alkali-Metal Clusters and the Jellium Model. *Chem. Phys. Lett.* **1987**, *134* (1), 1–5.
(36) Castleman Jr., A. W.; Khanna, S. N. Clusters, Superatoms, and Building Blocks of New Materials. *J. Phys. Chem. C* **2009**, *113* (7), 2664–2675.
(37) Bonacic-Koutecky, V.; Fantucci, P.; Koutecky, J. Quatum-Chemistry of Small Clusters of Elements of Group-IA, Group-IB, and Group-IIA: Fundamental Concepts, Predictions, and Interpretation of Experiments. *Chem. Rev.* **1991**, *91* (5), 1035–1108.
(38) Clemenger, K. Ellipsiodal Shell Structure in Free-Electron Metal-Clusters. *Phys. Rev. B* **1985**, *32* (2), 1359–1362.
(39) Jahn, H. A.; Teller, E. Stability of Polyatomic Molecules in Degenerate Electronic States. I. Orbital Degeneracy. *Proc. R. Soc. Lond. Ser. -Math. Phys. Sci.* **1937**, *161* (A905), 220–235.
(40) Mottelson, B.; Nilsson, S. Classification of the Nucleonic States in Deformed Nuclei. *Phys. Rev.* **1955**, *99* (5), 1615–1617.
(41) Siegfried, R. From Elements to Atoms - a History of Chemical Composition. *Trans. Am. Philos. Soc.* **2002**, *92*, 1–278.
(42) Reveles, J. U.; Khanna, S. N.; Roach, P. J.; Castleman Jr., A. W. Multiple Valence Superatoms. *Proc. Natl. Acad. Sci. U. S. A.* **2006**, *103* (49), 18405–18410.
(43) Tyo, E. C.; Castleman Jr., A. W.; Reber, A. C.; Khanna, S. N. Analogous Reactivity of Pd+ and ZrO+: Comparing the Reactivity with Small Hydrocarbons. *J. Phys. Chem. C* **2011**, *115* (34), 16797–16802.
(44) Tyo, E. C.; Noessler, M.; Rabe, S.; Harmon, C. L.; Mitric, R.; Bonacic-Koutecky, V.; Castleman Jr., A. W. Exploring Similarities in Reactivity of Superatom Species: A Combined Theoretical and Experimental Investigation. *Phys. Chem. Chem. Phys.* **2012**, *14* (6), 1846–1849.
(45) Bergeron, D. E.; Roach, P. J.; Castleman Jr., A. W.; Jones, N.; Khanna, S. N. Al Cluster Superatoms as Halogens in Polyhalides and as Alkaline Earths in Iodide Salts. *Science* **2005**, *307* (5707), 231–235.
(46) Bergeron, D. E.; Castleman Jr., A. W.; Morisato, T.; Khanna, S. N. Formation of Al13I-: Evidence for the Superhalogen Character of Al-13. *Science* **2004**, *304* (5667), 84–87.
(47) Reber, A. C.; Khanna, S. N.; Castleman Jr., A. W. Superatom Compounds, Clusters, and Assemblies: Ultra Alkali Motifs and Architectures. *J. Am. Chem. Soc.* **2007**, *129* (33), 10189–10194.

(48) Luo, Z.; Berkdemir, C.; Smith, J. C.; Castleman Jr., A. W. Cluster Reaction of [Ag-8](-)/[Cu-8](-) with Chlorine: Evidence for the Harpoon Mechanism? *Chem. Phys. Lett.* **2013**, *582*, 24–30.
(49) Luo, Z.; Castleman Jr., A. W. Special and General Superatoms. *Acc. Chem. Res.* **2014**, *47* (10), 2931–2940.
(50) Cheng, S.-B.; Berkdemir, C.; Castleman Jr., A. W. Observation of D-P Hybridized Aromaticity in Lanthanum-Doped Boron Clusters. *Phys. Chem. Chem. Phys.* **2014**, *16* (2), 533–539.
(51) Gan, Y.; Qiao, L. Combustion Characteristics of Fuel Droplets with Addition of Nano and Micron-Sized Aluminum Particles. *Combust. Flame* **2011**, *158* (2), 354–368.
(52) Tyagi, H.; Phelan, P. E.; Prasher, R.; Peck, R.; Lee, T.; Pacheco, J. R.; Arentzen, P. Increased Hot-Plate Ignition Probability for Nanoparticle-Laden Diesel Fuel. *Nano Lett.* **2008**, *8* (5), 1410–1416.
(53) Lewis, W. K.; Rumchik, C. G.; Smith, M. J.; Fernando, K. A. S.; Crouse, C. A.; Spowart, J. E.; Guliants, E. A.; Bunker, C. E. Comparison of Post-Detonation Combustion in Explosives Incorporating Aluminum Nanoparticles: Influence of the Passivation Layer. *J. Appl. Phys.* **2013**, *113* (4), 044907.
(54) Dlott, D. D. Thinking Big (and Small) About Energetic Materials. *Mater. Sci. Technol.* **2006**, *22* (4), 463–473.
(55) Hall, C. M. Process of Reducing Aluminum from Its Fluoride Salts by Electrolysis. US400664, 1889.
(56) Chung, S. W.; Guliants, E. A.; Bunker, C. E.; Hammerstroem, D. W.; Deng, Y.; Burgers, M. A.; Jelliss, P. A.; Buckner, S. W. Capping and Passivation of Aluminum Nanoparticles Using Alkyl-Substituted Epoxides. *Langmuir* **2009**, *25* (16), 8883–8887.
(57) Leuchtner, R.; Harms, A.; Castleman Jr., A. Thermal Metal Cluster Anion Reactions - Behavior of Aluminum Clusters with Oxygen. *J. Chem. Phys.* **1989**, *91* (4), 2753–2754.
(58) McMahon, B. W.; Perez, J. P. L.; Anderson, S. L.; Schneider, S.; Boatz, J.; Hawkins, T.; McCrary, P. D.; Beasley, P. A.; Rogers, R. D. Dual Ligand Passivation and Homogeneous Media Ball Milling: Novel Approaches for Both the Synthesis and Capping of Air-Stable Aluminum Nanoparticles. *Abstr. Pap. Am. Chem. Soc.* **2012**, *243*.
(59) Ashman, C.; Khanna, S. N.; Liu, F.; Jena, P.; Kaplan, T.; Mostoller, M. (BAl12)Cs: A Cluster-Assembled Solid. *Phys. Rev. B* **1997**, *55* (23), 15868–15873.
(60) Berkdemir, C.; Castleman Jr., A. W.; Sofo, J. O. Metal-Substituted Ti8C12 Metallocarbohedrynes: Toward Less Reactive Clusters as Building Blocks of Cluster-Assembled Materials. *Phys. Chem. Chem. Phys.* **2012**, *14* (27), 9642–9653.
(61) Qian, M.; Reber, A. C.; Ugrinov, A.; Chaki, N. K.; Mandal, S.; Saavedra, H. M.; Khanna, S. N.; Sen, A.; Weiss, P. S. Cluster-Assembled Materials: Toward Nanomaterials with Precise Control over Properties. *Acs Nano* **2010**, *4* (1), 235–240.
(62) Perez, A.; Melinon, P.; Dupuis, V.; Jensen, P.; Prevel, B.; Tuaillon, J.; Bardotti, L.; Martet, C.; Treilleux, M.; Broyer, M.; et al. Cluster Assembled Materials: A Novel

Class of Nanostructured Solids with Original Structures and Properties. *J. Phys. - Appl. Phys.* **1997**, *30* (5), 709–721.

(63) Jena, P.; Khanna, S. N.; Rao, B. K. Stability and Electronic Structure of Cluster Assembled Materials. In *Cluster Assembled Materials*; Sattler, K., Ed.; 1996; Vol. 232, pp 1–25.

(64) Melinon, P.; Paillard, V.; Dupuis, V.; Perez, A.; Jensen, P.; Hoareau, A.; Broyer, M.; Vialle, J.; Pellarin, M.; Baguenard, B.; et al. From Free Clusters to Cluster-Assembled Materials. *Int. J. Mod. Phys. B* **1995**, *9* (4-5), 339–397.

(65) Luo, Z.; Smith, J. C.; Woodward, W. H.; Castleman Jr., A. W. The Growth of Ionic Crystals Based on the Halogenation of Copper Cluster Anions. *J. Phys. Chem. A* **2012**, *116* (9), 2012–2017.

(66) Nacer, B.; Massobrio, C.; Felix, C. Deposition of Metallic Clusters on a Metallic Surface at Zero Initial Kinetic Energy: Evidence for Implantation and Site Exchanges. *Phys. Rev. B* **1997**, *56* (16), 10590–10595.

(67) Woodward, W. H.; Blake, M. M.; Luo, Z.; Weiss, P. S.; Castleman Jr., A. W. Soft-Landing Deposition of Al-17(-) on a Hydroxyl-Terminated Self-Assembled Monolayer. *J. Phys. Chem. C* **2011**, *115* (13), 5373–5377.

(68) Castro, M.; Flores, R.; Duncan, M. A. Theoretical Study of Nascent Solvation in Ni+(Benzene)(m), m=3 and 4, Clusters. *J. Phys. Chem. A* **2013**, *117* (47), 12546–12559.

(69) Luo, Z.; Smith, J. C.; Goff, T. M.; Adair, J. H.; Castleman Jr., A. W. Gold Cluster Coatings Enhancing Raman Scattering from Surfaces: Ink Analysis and Document Identification. *Chem. Phys.* **2013**, *423*, 73–78.

(70) Desireddy, A.; Conn, B. E.; Guo, J.; Yoon, B.; Barnett, R. N.; Monahan, B. M.; Kirschbaum, K.; Griffith, W. P.; Whetten, R. L.; Landman, U.; et al. Ultrastable Silver Nanoparticles. *Nature* **2013**, *501* (7467), 399–402.

(71) Luo, Z.; Woodward, W. H.; Castleman Jr., A. W. Distinguishable Behavior of Multiple and Individual Rhodamine-6G Molecules on Spherical Ag Nanoparticles Examined Via Time Dependence of the SERS Spectra. *J. Raman Spectrosc.* **2012**, *43* (12), 1905–1912.

(72) Golightly, J. S.; Castleman Jr., A. W. Analysis of Titanium Nanoparticles Created by Laser Irradiation Under Liquid Environments. *J. Phys. Chem. B* **2006**, *110* (40), 19979–19984.

Chapter 2

Experimental Apparatus

2.1. Instrument Overview

Instruments used in gas phase metal cluster studies vary in size, shape, complexity, and purpose. The vast majority that this author has observed are all custom built and no two are identical; though all the instruments are unique, there are many shared principles and similar components. The instrument used in this work is a custom high vacuum quadrupole mass spectrometer that contains parts that have been in use for more than 25 years, but the overall instrument has been revised several times throughout its lifespan.[1–10] This chapter details the current assembly and some of the rationale as to why the instrument has been built thus.

The common name given to the instrument is MIFT standing for multiple ion flow tube. A diagram of the instrument is provided in Figure 2.1. The overall intent for this instrument is to enable the production of small metal clusters ranging in size from 2-40 atoms, expose the molecules to various reactants, and detect any products from favorable reactions. MIFT enables observation of the reactivity of an entire distribution of clusters which can provide information about specific reactions. From this information, general trends and patterns can be found that help illuminate how size and composition affect the physical and electronic characteristics of small clusters.

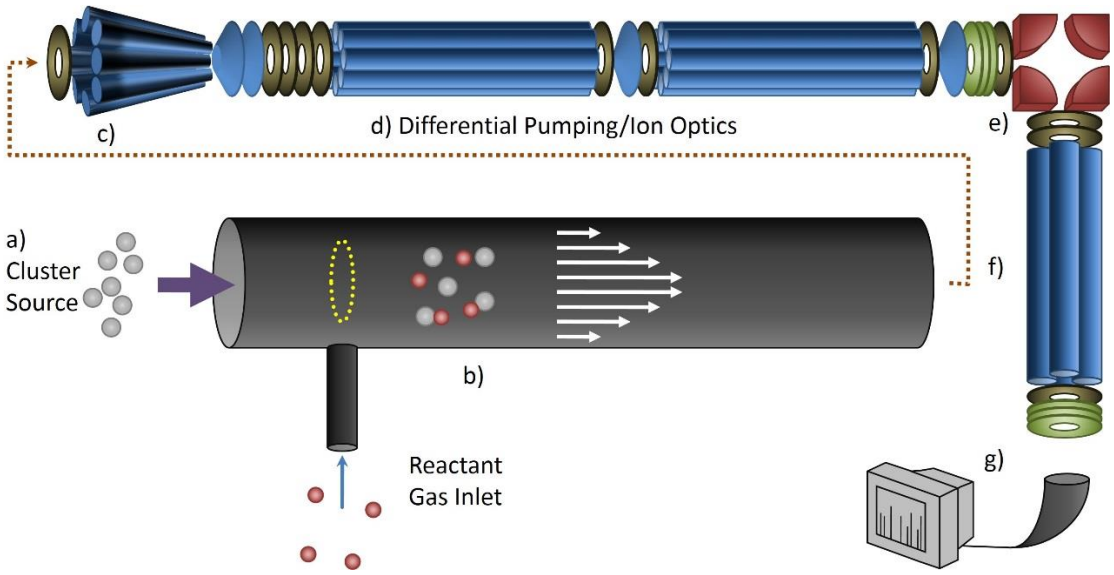

Figure 2.1. Schematic of the experimental instrument. Clusters are formed in the (a) laser vaporization source and then expanded into the (b) laminar flow-tube where they interact with reactants. From the flow-tube, the clusters are funneled and directed through the instrument by a (c) conical octopole, (d) numerous electrostatic lenses, and octopoles, a (e) quadrupole energy deflector, and a (f) mass selecting quadrupole. The clusters are then detected using a (g) channeltron electron multiplier. Adapted from reference 11.

2.2. Cluster Source

In any experiment involving metal clusters, the first consideration is how to form the desired clusters. This section briefly describes several varieties of cluster sources and some instances when one cluster source may be more advantageous than another for an experimental system. Cluster sources can vary widely depending on the requirements of the experiment; however, the output of different sources can be very similar. Nearly all sources form clusters through a similar process of nucleation where a material is atomized and then the atoms combine to form larger clusters. When deciding which source will work best for an instrument, some considerations to take into account should include cost,

whether you want ions, neutrals, or both, and the base material from which the clusters will be formed. These factors will highly influence which source is most appropriate for an experimental system. A useful and commonly cited review of cluster science written by Walt de Heer provides a general analysis of the range of cluster studies including methods of producing clusters.[12]

2.2.1. Thermal Oven Sources

Some of the earliest cluster studies utilized thermal ovens, often called Knudsen cells, to produce clusters. This is a rather simple and inexpensive method for cluster production, but does have some drawbacks. The oven technique relies upon heating a metal near its boiling point causing evaporation of the material. This drastically limits the possible metals available for study because of the rarity of low-boiling point metals one of the most common being sodium.[13] This technique produces only neutral clusters; however, additional steps can generally be incorporated if ionized clusters are desired. The evaporated atoms are ejected through a small aperture and form clusters as they are supersonically expanded into the vacuum instrument.[14] This source along with the magnetron gas aggregation source (to be discussed in the next section) both provide continuous cluster beams in contrast to other sources which are pulsed.

2.2.2. Pulsed Arc Cluster Ion Source

The pulsed arc cluster ion source (PACIS) developed in the early 1990s uses an applied voltage to generate an arc between two electrodes that ablates a metal for cluster

production.[15] This process is similar to the laser vaporization method (to be discussed in section 2.2.4) except that rather than using a large electric discharge to induce lasing which then ablates a rod, the electric discharge ablates the rod directly (Figure 2.2). The PACIS is best suited for making clusters from materials that conduct electricity, but has also been used with non-conducting materials with low melting points.[16,17] This method produces neutrals, cations, and anions of the metal and can also form metal-rare-gas clusters if seeded with the proper buffer gas.[18,19]

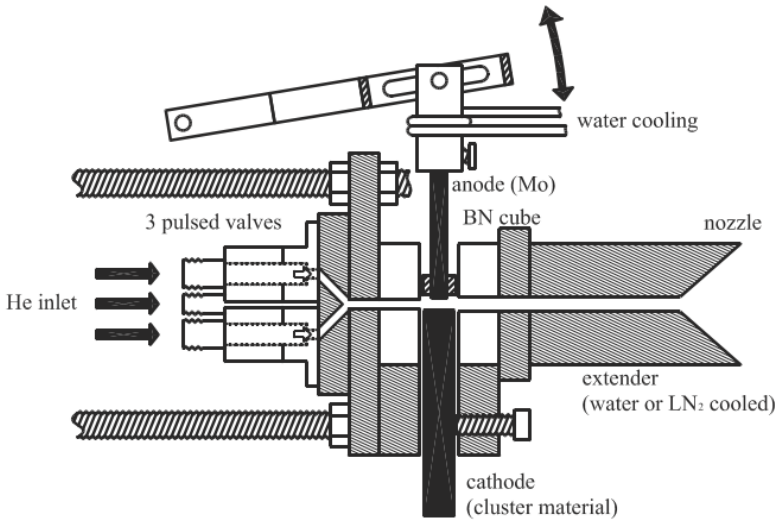

Figure 2.2. Schematic of a pulsed arc cluster source. An arc discharge from the anode to the cathode results in clusters made from the cathode material. This particular source can be operated up to 1000 Hz utilizing the three gas inlet valves. The lever mechanism attached to the anode allows the anode to be adjusted as the cathode material is etched away. Reprinted from reference [15].

2.2.3. Magnetron Gas Aggregation Source

Magnetron sputtering sources were originally developed and continue to be a useful tool for the deposition of thin films of relative uniformity and thickness onto a surface

(Figure 2.3).[20–23] A brief description of the physics behind magnetron sputtering is as follows. A potential is applied to a sputtering target and a magnetic field is used to confine charged particles to an area close to the magnetron head which enhances ionization and intensifies the plasma.[24] The target surface is bombarded by argon ions (or other charged atoms) which, when they collide with the surface, atoms (both charged and neutral) are etched away creating a circular pattern on the target metal called the "race track". Once the metal atoms are in the gas phase they collide and form clusters (this process is explained in further detail in section 2.2.4)

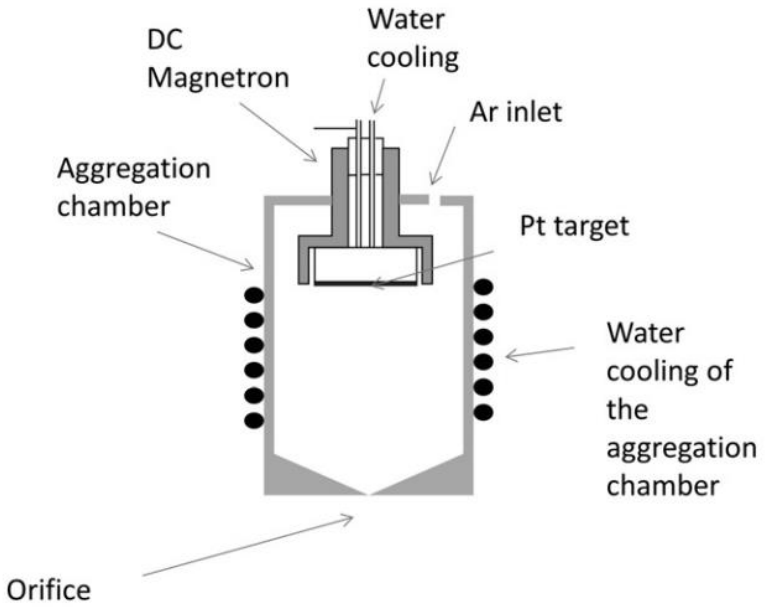

Figure 2.3. Schematic of a magnetron gas aggregation source with a platinum target. The magnetron head can be adjusted to modify the distance from the head to the orifice which alters the nucleation/aggregation time and thus the size distribution of the clusters. Reprinted from reference [21].

One unique advantage of this device is that it produces constant current of clusters and can often outperform other sources in total cluster throughput. Sputtering sources also have many parameters such as voltage, current, argon pressure, distance from the target to the source exit, etc., that can be adjusted in order to alter the resultant size distribution of products allowing a production flexibility not generally found with other cluster sources.[25] This flexibility has an added advantage in that the parameters can be altered without venting the source to atmosphere and some can be tuned concurrently with production of clusters allowing real time observation of the parameter's effects upon cluster signal.

This source has wide applicability for many metals such as copper, silver, and gold. Some radio frequency techniques have been used to create clusters from insulating materials.[24] Magnetron sputtering also produces neutrals, cations, and anions preventing the need for any additional ionizing equipment that would be needed for other sources such as the thermal evaporation source.[26] If a sputtering source is used in the cluster apparatus, several precautions must be taken to prevent damage to the magnetron head and the rest of the apparatus. First, there is a significant amount of heat generated from the plasma and the magnetron head and the walls of the source must be cooled. In most cases the cooling is achieved with liquid nitrogen; water has been used in some studies.[25] Next, the plasma may begin to etch some of the surrounding metal from the magnetron head introducing detectable amounts of contaminants in the cluster distribution. Lastly, because of the continuous nature of the magnetron sputtering source, a significant gas flow is needed which may require an additional differential pumping section between the source and the rest of the vacuum instrument. The instrument used in the present work has been adapted

to utilize both a magnetron gas aggregation source and a laser vaporization source; however, the laser vaporization source was the only source used in the work described herein.

2.4. Laser Vaporization Cluster Source

The development of the laser vaporization (LaVa) source is commonly attributed to the Smalley group at Rice University and to Vladimir Bondybey at AT&T Bell Laboratories from work accomplished in the early 1980s.[27–29] Since the inception of the Lava source nearly thirty years ago, many studies have customized the original design altering the sample shape, number of samples, gas flow, and more.[30–34] A standard LaVa source design is provided in Figure 2.4.[35]

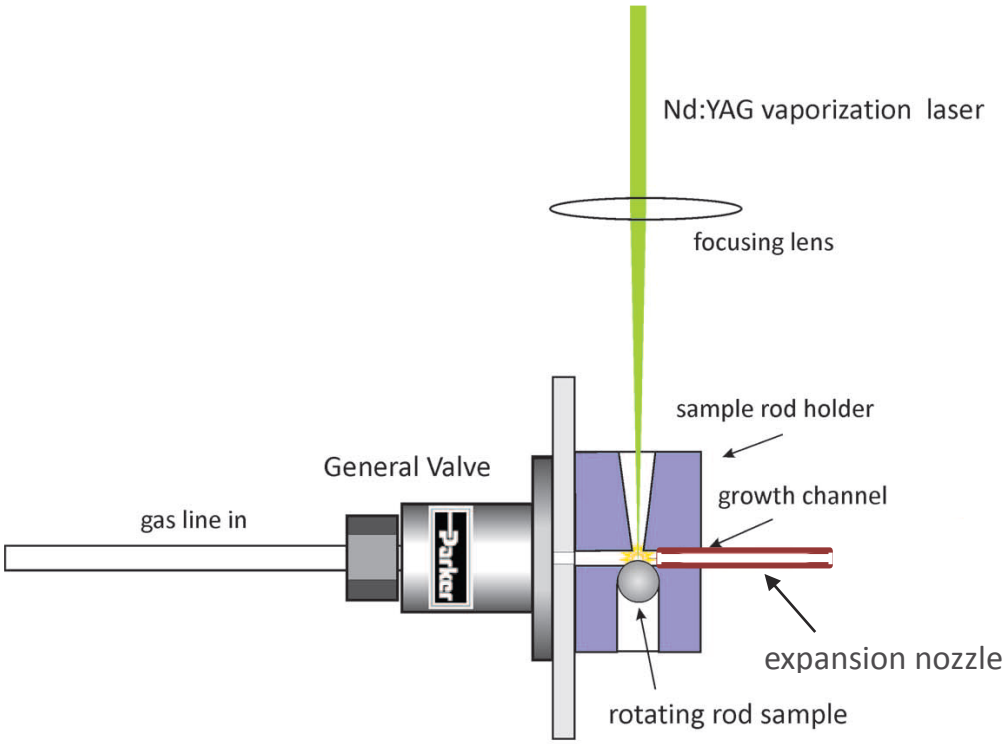

Figure 2.4. A common setup for a laser vaporization cluster source. Adapted from reference [35].

The basic premise behind a LaVa source is that when a laser beam is focused onto a metal surface, a plasma is formed. This plasma evaporates the surface and produces an atomized gaseous form of the substrate material which then condenses into a distribution of cluster sizes. These clusters are then extracted from the source into a vacuum instrument through an expansion nozzle. Because a LaVa source produced the clusters seen in this work, the specifics of this particular LaVa source and some background as to the principles that govern laser vaporization cluster sources are discussed below.

The second harmonic of a Nd-YAG laser (532 nm) with the power adjusted to between 100-250 mj/pulse is focused through a focusing lens placed such that the focal

point of the laser is located on the surface of a metal rod. The laser power needed for cluster formation can vary widely depending on the ablation material. Pulsed lasers compared to continuous lasers are the most common because continuous lasers often do not produce enough power to sustain a plasma on the target metal. A custom carriage device attached to a stepper motor provides translation and rotation of the metal rod in order to prevent ablation of only one location leading to the formation of a hole in the rod and loss of cluster signal.

Once the rod is ablated, the individual gas-phase atoms undergo many collisions with other metal atoms and/or with a buffer gas. This gas is introduced into the source in order to provide collisional cooling of the hot clusters and to carry the clusters out of the source and into the rest of the instrument. These collisions, allow the atoms to form dimers, trimers and clusters of up to hundreds of atoms. The following equations provide a simplistic view of the growth of clusters:

$$M + M \rightarrow M_2^* \tag{2.1}$$

$$M_2^* + M \rightarrow M_2 + M^* \tag{2.2}$$

$$M_n + M \rightarrow M_{n+1} \tag{2.3}$$

where M can represent either individual atoms or molecules in the collisions.

As atoms collide and combine, excess energy must be quenched or no growth will occur due to evaporation of surface atoms. The collisions depicted by equation 2.2 can either be successive collisions or three-body collisions (a combination of equations 2.1 and

2.2); however, both pathways remove excess kinetic energy from the cluster preventing evaporation. Buffer gas atoms significantly outnumber those of the ablated metal and provide most of the collisional cooling. Many different gases can be used as the buffer but they will each affect cluster cooling differently resulting in different cluster distributions. Argon and helium are some of the most common buffer gases due to being inert and their ability to efficiently cool clusters.[35] In some studies, other gases such as oxygen, nitrogen, methane, etc., are mixed with an inert gas to make cluster oxides, nitrides, and carbides.[36–39]

In many cases the buffer gas is introduced into the source through a pulsed nozzle.[40–43] The use of a pulsed nozzle reduces the gas load on the vacuum system preventing the need for additional pumping of the vacuum instrument. The laser and pulsed nozzle are usually synchronized by a pattern generator so that the time delay between the laser and gas pulses can be adjusted in order to maximize cluster signal. The exact time overlap between the laser and gas pulses are unique to each instrument as are all of the operational variants (carrier gas, backing gas pressure, pulse widths, etc.) of the experiment and tuning of the overlap should occur as new experimental conditions are introduced. The research in this work required utilizes continuous flow, which is incompatible with a pulse nozzle and required other methods, which are discussed in the following paragraphs and sections.

The size and distribution of the resultant clusters vary depending upon several factors some of which can be altered while others are inherent to the specific LaVa source. The most significant factor in determining the size distribution of the clusters formed is the

amount of time spent in the source before entering the vacuum instrument. As clusters/atoms undergo successively increasing numbers of collisions they will continue to increase in size. The expansion nozzle controls the flow of gas from the source to the rest of the instrument and is the most significant factor in determining the resultant size distribution of the clusters made in the source. By changing the inner diameter and the length of the nozzle, the nucleation/aggregation time spent in the source can be altered. For larger clusters, a nozzle with a smaller diameter and greater length would be implemented while for smaller clusters the opposite would be used. Expansion nozzles have been used to make clusters since Becker and Henkes observed condensation from supersonic jets formed from expansion nozzles in the 1950s.[44] There is no way to predict the exact diameter and length needed for a specific size range and finding the appropriate nozzle for an experiment requires the trial and error of varying nozzle dimensions until the correct size is found.[35] This method of finding the correct nozzle is quite time consuming because it requires the venting of the source and manually exchanging one nozzle for another and then pumping the source down to vacuum again before a new test can be started.

Though the specific dimensions of a nozzle that will produce a set distribution of clusters cannot be predicted, it is useful to understand how the length and inner diameter affect the conductance through the nozzle to enable educated guesses rather than blind trial and error. Conductance of a pipe is inversely proportional to its length and proportional to the fourth power of its diameter. Thus changing the diameter of the nozzle will result in substantial changes to the cluster distribution while altering the length will act as more of

a fine tuning effect.[45] The expansion nozzle used in this work is made of Teflon and is 2.5 cm long with an inner diameter of 3.2 mm.

LaVa sources all vary in size and shape but the overall process and purpose is the same: the use of a laser in the production of clusters in the gas phase. Despite all the information available about Lava sources, no two sources are exactly alike nor will they produce the exact same cluster distributions. In the Castleman group, there are four very similar LaVa sources and while one may produce clusters of a particular metal, the others may not. The reasons for this inconsistency are not apparent and perhaps further study will help elucidate the answers. Until all the intricacies are known, we must rely on the best information available. This writer suggests that a study of LaVa sources start with a review written by Mike Duncan who was a member of the Smalley group involved in some of the original LaVa source development.[35]

2.3. Laminar Flow-Tube

Once the clusters exit the source they enter the reaction flow-tube. This piece of equipment has been used in experimental studies for around 30 years and is probably the oldest piece of the entire instrument.[1,46,47] Within a few centimeters of departing the source, the cluster-buffer gas mixture reaches laminar flow and becomes thermal. Reactants can be introduced into the flow-tube through an inlet located approximately 50 cm downstream from the source. Gases are the most common reactant used in this instrument; however, solids that are easily sublimated or liquids with a sufficiently high vapor pressure are also

eligible candidates for reactivity studies and have been used in the past.[48] The flow-tube extends another 60 cm during which the clusters and reactant can interact multiple times. The flow from the source and through the flow-tube is measured at approximately 8000 standard cubic centimeters per minute (sccm) resulting in laminar flow and a stable pressure of 0.7 Torr at 245 cm from the end of the flow tube. In order to handle the high gas load through the source and flow-tube, a Stokes 1721 Mechanical Booster Pump is attached to the end of the flow-tube and is only open to the system during active cluster production. A cooling trap is used to prevent oil in the pump from contaminating the instrument.

To understand the importance of laminar flow it is first important to understand the phenomenon. Flow can be characterized using the Reynold's number which can be calculated using the following equation:

$$Re = \frac{D\upsilon\rho}{\mu} \tag{2.4}$$

where D is the diameter of the pipe, υ is the average fluid velocity, ρ is the fluid density, and μ is the fluid viscosity. The Reynold's number can be used to predict the pattern of flow whether it be laminar or turbulent (Figure 2.5). Generally, low Reynold's numbers, < 2100, predict a laminar flow, while Reynold's numbers > 2100 may be either laminar or turbulent depending on other factors of the pipe. Laminar flow of fluid in a pipe is represented by a parabolic velocity profile. The velocity at the interface between the fluid and the side walls is reduced due to friction.

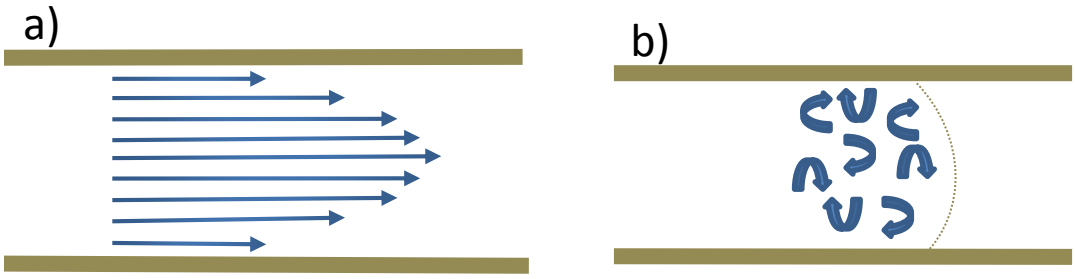

Figure 2.5. Schematic showing the different flow profiles of (a) laminar flow and (b) turbulent flow. The streamlines in laminar flow are represented by a parabolic profile. The fluid velocity of each atom or molecule in the turbulent flow regime is less predictable but the fluid propagates as a whole as it travels through the pipe.

The primary advantage of laminar flow is that the collisions between the fluid and the outer walls of the container result in thermal equilibrium within the system. Thus, by altering the temperature of the outer walls one may control the temperature of the entrained fluid. [49,50] Temperature control of gas-phase clusters has proven useful for studies of rate constants and activation energies;[51,52] however, activation energies and rate constants are outside the scope of this work.

The laminar flow-tube enables the determination of rate constants and activations energies; however, more common methods for this type of research include tandem mass spectrometry, and Fourier transform ion cyclotron mass spectrometry (FT-ICR). In tandem mass spectrometry two mass selecting quadrupoles are separated by a collision cell where a reactant can be introduced into the path of incoming ions. Using the first quadrupole, a single ion can be selected which then is exposed to a reactant in the collision cell. The products can then be sampled through the second quadrupole to determine any ionic products from the reaction. Temperature or energy dependent studies can be performed

using this method by altering the potential applied to the collision cell.[11,53] FT-ICR usually adds to the cluster's energy through resonant excitation though there are some methods that allow low-temperature studies if desired.[54,55] The availability of tandem mass spectrometry and FT-ICR begs the question of why laminar flow-tube reactivity would still be useful today. The other methods, while very advanced and efficient, are not quite as simple as using a temperature controlled flow-tube. In its most basic form a metal tube with heat tape and a thermometer could be sufficient. One benefit of the alternative methods is that they don't require the added pumping and they can mass select before and after the reaction occurs.

2.4. Differential Pumping, Ion Optics, and Cluster Detection

This instrument was most recently designed study the structure, reaction rates, and electronic properties of clusters. This is accomplished by combining two separate methods: reaction flow tube mass spectrometry and matrix isolation cavity ring down spectroscopy. The laminar flow-tube used in reactivity studies requires a higher pressure/flow of gas than most vacuum instruments and thus multiple differentially pumped vacuum chambers and a large number of alignment optics are used to navigate the cluster ions from a pressure of approximately 1 to 10^{-8} Torr. The reduction of the pressure increases the signal-to-noise ratio and prevents the deposition surface from becoming contaminated. Each individual electrostatic lens is not discussed here because comprehensively description of each lens is included in the dissertations of both Patrick Roach and William Woodward.[11,56] Because

each ion lens and flange has been described previously, this section only provides the general purpose for the chambers and ion optics.

The number of ion optics needed in the instrument are dependent upon the differential pumping. Once a low enough pressure is reached ($<10^{-3}$ mTorr), pumping capabilities are dominantly governed by the size of the connection flange between the pump and the chamber. This relates back to the discussion of gas conductance through expansion nozzles. Expansion nozzles are generally found in the viscous-flow regime where conductance is proportional to the fourth power of the diameter of the nozzle. Turbomolecular pumps operate under molecular flow conditions and conductance is proportional to the third power of the diameter of its opening.[45] Large flange sizes are used to maximize transport of molecules out of the instrument and out the exhaust. The large flange size of the pumps then impact the overall size of the instrument and distance the ions must travel necessitating more ion optics. To achieve the level of vacuum desired for our reactivity studies and especially for the deposition work three chambers are pumped individually by turbomolecular pumps each backed by an oil-free mechanical pump. Passage of molecules between the chambers is only permitted through an ion optic with a small aperture (2-5 mm in diameter) in its center.

The ions are extracted from the flow-tube through a focusing conical octopole. The conical octopole was developed and built by Uli Heiz in 2006 to help focus clusters for deposition onto a surface.[57] There are other methods by which clusters can be focused into a narrow beam such as an ion funnel. More information concerning ion focusing elements can be found in a review article by Kelly.[58] The conical octopole was integrated into this

instrument for various reasons but the main advantage in this case is that it is highly reliable under relatively high pressures (1 Torr) and a large fixed flow rate (8000 sccm). Some of its other advantages are that it does not charge from cluster buildup thereby minimizing the need to alter the applied potentials and it is relatively easy to clean.

Once directed through the conical octopole, the ions are transported through the first aperture optic and into the next chamber. An einzel stack and octopole then direct the clusters through the next aperture into the following chamber which is a duplicate of the first chamber. Octopoles provide efficient ion transport over long distances with little to no loss of signal. They are used in place of multiple einzel stacks because of their efficiency and they require less daily maintenance/tuning than would be requisite of the equivalent number of electrostatic lenses.

Once through the second chamber and the third aperture (first and second chambers) the ions are focused with another einzel stack to facilitate their transmission through a quadrupole energy deflector. The quadrupole energy deflector, sometimes termed a quad bender, changes the trajectory of the ions by 90°. The perpendicular directional change relative to the ion beam axis works as a filter to remove any neutral clusters or carrier gas atoms from the ionic cluster beam and enhance the resolution of the resultant data and reduce contamination of deposition surfaces. After the quadrupole energy deflector, the ions enter the mass selecting quadrupole. The capabilities of this quadrupole allow detection of any ion mass from 10 to 4000 amu; however, the present work focuses on small clusters and masses above 1000 amu are outside this range of interest. After the mass selecting quadrupole, a final einzel stack focuses the ions across a

small gap into the detector. The gap is present to allow a surface to be inserted between the mass selecting quadrupole and the detector for deposition studies (to be discussed in Chapter 4).

The detector used in this work is a channeltron electron multiplier (Detector Technology Inc. model# 402A-H). Clusters are directed toward a highly charged dynode (5 kV) and when they impact the dynode, electrons are ejected and funneled into a charged (1.2-2.5 kV) cornucopia shaped electron multiplier. As the electrons collide with the walls of the multiplier, successive cascades of electrons are produced, which then continue until the end of the multiplier. The charge applied to the dynode is constant and never altered; however, as the electron multiplier ages, the applied potential must be increased in order to compensate for degradation and loss of efficiency. The potential on the multiplier should be adjusted to provide appropriate signal but excessive potentials can cause accelerated degradation. Once the multiplier potential reaches 2.5 kV, the time for a new detector has arrived.

After a significant repair or cleaning, ion signal may no longer reach the detector. Typical ion signal produced in this LaVa source is not sufficient for measurement by a typical ammeter and in cases such as these a picoammeter is used in order to optimize the lens settings and direct the ions back to the detector. The method for a realignment of the system is to use each ion optic as a faraday plate connected to the picoammeter. Applying a voltage to the faraday plate (ion optic) will cause the incoming cluster ions to impact the optic and produce a signal current. Monitoring the signal current and altering the voltages applied to optics upstream will optimize cluster throughput in the instrument. The

picoammeter is attached to an optic, the upstream optic voltages are optimized, and then the process is repeated with the picoammeter attached to the next optic downstream. Knowledge of the purpose of each lens is important in this procedure as an einzel stack may be optimized to produce an intense ion signal on the following lens, but result in less signal reaching the detector. Once the proper ion optic voltages are set and signal reaches the detector, regular tuning of the voltages should occur at the start of each new trial as some optic voltages will require small alterations due to excessive contamination buildup and other miniscule daily aberrations.

2.5. References

(1) Shul, R.; Upschulte, B.; Passarella, R.; Leuchtner, R.; Keesee, R.; Castleman Jr., A. Chemiluminescent Studies of Cs2+ in a Flowing Ar Afterglow. *Abstr. Pap. Am. Chem. Soc.* **1986**, *191*, 75 – PHYS.

(2) Sigsworth, S.; Difazio, L.; Keesee, R.; Castleman Jr., A. Study of the Formation and Reactions of Clusters Involving Metal-Cations. *Abstr. Pap. Am. Chem. Soc.* **1986**, *191*, 69 – PHYS.

(3) Castleman Jr., A.; Leuchtner, R.; Harms, A. Studies of the Reactivity of Metal Cluster Ions Under Well-Defined Thermal-Reaction Conditions. *Abstr. Pap. Am. Chem. Soc.* **1990**, *199*, 28 – COLL.

(4) Sigsworth, S.; Castleman Jr., A. Reaction of Group-V and Group-VI Transition-Metal Oxide and Oxyhydroxide Anions with O2, H2O, and HCl. *J. Am. Chem. Soc.* **1992**, *114* (26), 10471–10477.

(5) Vann, W. D.; Wagner, R. L.; Castleman Jr., A. W. Gas-Phase Reactions of Nickel and Nickel-Rich Oxide Cluster Anions with Nitric Oxide. 2. The Addition of Nitric Oxide, Oxidation of Nickel Clusters, and the Formation of Nitrogen Oxide Anions. *J. Phys. Chem. A* **1998**, *102* (45), 8804–8811.

(6) Bergeron, D. E.; Castleman Jr., A. W. Insights into the Stability of Silicon Cluster Ions: Reactive Etching with O-2. *J. Chem. Phys.* **2002**, *117* (7), 3219–3223.

(7) Bergeron, D. E.; Roach, P. J.; Castleman Jr., A. W.; Jones, N. O.; Reveles, J. U.; Khanna, S. N. Reactions of Al(n)l(x)(-) with Methyl Iodide: The Enhanced Stability of Al(7)l and the Chemical Significance of Active Centers. *J. Am. Chem. Soc.* **2005**, *127* (46), 16048–16053.

(8) Roach, P. J.; Reber, A. C.; Woodward, W. H.; Khanna, S. N.; Castleman Jr., A. W. Al4H7- Is a Resilient Building Block for Aluminum Hydrogen Cluster Materials. *Proc. Natl. Acad. Sci. U. S. A.* **2007**, *104* (37), 14565–14569.
(9) Woodward, W. H.; Blake, M. M.; Luo, Z.; Weiss, P. S.; Castleman Jr., A. W. Soft-Landing Deposition of Al-17(-) on a Hydroxyl-Terminated Self-Assembled Monolayer. *J. Phys. Chem. C* **2011**, *115* (13), 5373–5377.
(10) Sigsworth, S. A Kinetic Study of Metal Ion and Metal Oxide Anion Reaction. PhD Dissertation, The Pennsylvania State University: University Park, PA, 1991.
(11) Woodward, W. H. H. Aluminum Cluster Anion Reactivity: Applications in Energetic Materials and Catalysis. PhD Dissertation, The Pennsylvania State University: University Park, PA, 2011.
(12) Deheer, W. The Physics of Simple Metal-Clusters - Experimental Aspects and Simple-Models. *Rev. Mod. Phys.* **1993**, *65* (3), 611–676.
(13) Knight, W. D.; Clemenger, K.; Deheer, W. A.; Saunders, W. A.; Chou, M. Y.; Cohen, M. L. Electronic Shell Structure and Abundances of Sodium Clusters. *Phys. Rev. Lett.* **1984**, *52* (24), 2141–2143.
(14) Hagena, O. Nucleation and Growth of Clusters in Expanding Nozzle Flows. *Surf. Sci.* **1981**, *106* (1-3), 101–116.
(15) Klipp, B.; Grass, M.; Muller, J.; Stolcic, D.; Lutz, U.; Gantefor, G.; Schlenker, T.; Boneberg, J.; Leiderer, P. Deposition of Mass-Selected Cluster Ions Using a Pulsed Arc Cluster-Ion Source. *Appl. Phys. -Mater. Sci. Process.* **2001**, *73* (5), 547–554.
(16) Gantefor, G.; Hunsicker, S.; Jones, R. Prediction and Observation of Ring and Chain Isomers in S(n)- Ions. *Chem. Phys. Lett.* **1995**, *236* (1-2), 43–49.
(17) Jones, R.; Gantefor, G.; Hunsicker, S.; Pieperhoff, P. Structure and Spectroscopy of Phosphorus Cluster Anions - Theory (simulated Annealing) and Experiment (photoelectron Detachment). *J. Chem. Phys.* **1995**, *103* (22), 9549–9562.
(18) Gantefor, G.; Siekmann, H.; Lutz, H.; Meiwes-Broer, K. Pure Metal and Metal-Doped Rare-Gas Clusters Grown in a Pulsed-Arc Cluster Ion-Source. *Chem. Phys. Lett.* **1990**, *165* (4), 293–296.
(19) Siekmann, H.; Luder, C.; Faehrmann, J.; Lutz, H.; Meiwes-Broer, K. The Pulsed-Arc Cluster Ion-Source (PACIS). *Z. Phys. -At. Mol. Clust.* **1991**, *20* (1-4), 417–420.
(20) Mattox, D. M. *The Foundations of Vacuum Coating Technology*; Noyes Publications/William Andrew Publishing: Norwich, NY, 2003.
(21) Kylian, O.; Prokes, J.; Polonskyi, O.; Cechvala, J.; Kousal, J.; Pesicka, J.; Hanus, J.; Biederman, H. Deposition and Characterization of Pt Nanocluster Films by Means of Gas Aggregation Cluster Source. *Thin Solid Films* **2014**, *571*, 13–17.
(22) Kitamoto, Y.; Abe, M.; Naoe, M. Deposition of Co-Cr Films with Excellent C-Axis Orientation and Uniform Thickness for Rigid Disks Using Compact Sputtering Apparatus. *Ieee Trans. Magn.* **1996**, *32* (5), 4547–4549.
(23) Thornton, J. Influence of Apparatus Geometry and Deposition Conditions on Structure and Topography of Thick Sputtered Coatings. *J. Vac. Sci. Technol.* **1974**, *11* (4), 666–670.
(24) Pratontep, S.; Carroll, S. J.; Xirouchaki, C.; Streun, M.; Palmer, R. E. Size-Selected Cluster Beam Source Based on Radio Frequency Magnetron Plasma Sputtering and Gas Condensation. *Rev. Sci. Instrum.* **2005**, *76* (4), 045103.

(25) Luo, Z.; Woodward, W. H.; Smith, J. C.; Castleman Jr., A. W. Growth Kinetics of Al Clusters in the Gas Phase Produced by a Magnetron-Sputtering Source. *Int. J. Mass Spectrom.* **2012**, *309*, 176–181.
(26) Ho, J.; Ervin, K.; Lineberger, W. Photoelectron-Spectroscopy of Metal Cluster Anions - Cun-, Agn-, and Aun-. *J. Chem. Phys.* **1990**, *93* (10), 6987–7002.
(27) Bondybey, V.; English, J. Laser-Induced Fluorescence of Metal-Clusters Produced by Laser Vaporization - Gas-Phase Spectrum of Pb-2. *J. Chem. Phys.* **1981**, *74* (12), 6978–6979.
(28) Dietz, T.; Duncan, M.; Powers, D.; Smalley, R. Laser Production of Supersonic Metal Cluster Beams. *J. Chem. Phys.* **1981**, *74* (11), 6511–6512.
(29) Powers, D.; Hansen, S.; Geusic, M.; Puiu, A.; Hopkins, J.; Dietz, T.; Duncan, M.; Langridgesmith, P.; Smalley, R. Supersonic Metal Cluster Beams - Laser Photo-Ionization Studies of Cu2. *J. Phys. Chem.* **1982**, *86* (14), 2556–2560.
(30) Nonose, S.; Sone, Y.; Onodera, K.; Sudo, S.; Kaya, K. Structure and Reactivity of Bimetallic Convm Clusters. *J. Phys. Chem.* **1990**, *94* (7), 2744–2746.
(31) Guo, B.; Kerns, K.; Castleman Jr., A. Ti8C12+-Metallo-Carbohedrenes - a New Class of Molecular Clusters. *Science* **1992**, *255* (5050), 1411–1413.
(32) O'Brien, S.; Liu, Y.; Zhang, Q.; Heath, J.; Tittle, F.; Curl, R.; Smalley, R. Supersonic Cluster Beams of III-V Semiconductors - Gaxasy. *J. Chem. Phys.* **1986**, *84* (7), 4074–4079.
(33) Milani, P.; Deheer, W. Improved Pulsed Laser Vaporization Source for Production of Intense Beams of Neutral and Ionized Clusters. *Rev. Sci. Instrum.* **1990**, *61* (7), 1835–1838.
(34) Roach, P. J.; Woodward, W. H.; Castleman Jr., A. W.; Reber, A. C.; Khanna, S. N. Complementary Active Sites Cause Size-Selective Reactivity of Aluminum Cluster Anions with Water. *Science* **2009**, *323* (5913), 492–495.
(35) Duncan, M. A. Invited Review Article: Laser Vaporization Cluster Sources. *Rev. Sci. Instrum.* **2012**, *83* (4), 041101.
(36) Johnson, G. E.; Mitric, R.; Noessler, M.; Tyo, E. C.; Bonacic-Koutecky, V.; Castleman Jr., A. W. Influence of Charge State on Catalytic Oxidation Reactions at Metal Oxide Clusters Containing Radical Oxygen Centers. *J. Am. Chem. Soc.* **2009**, *131* (15), 5460–5470.
(37) Knappenberger, K. L.; Jones, C. E.; Sobhy, M. A.; Iordanov, I.; Sofo, J.; Castleman Jr., A. W. Anion Photoelectron Spectroscopy and Density Functional Investigation of Vanadium Carbide Clusters. *J. Phys. Chem. A* **2006**, *110* (47), 12814–12821.
(38) Berkdemir, C.; Cheng, S.-B.; Castleman Jr., A. W. Assigning the Mass Spectrum of NbN-: Photoelectron Imaging Spectroscopy and Nominal-Mass Counterpart Analysis. *Int. J. Mass Spectrom.* **2014**, *365*, 222–224.
(39) Gunaratne, K. D. D.; Berkdemir, C.; Harmon, C. L.; Castleman Jr., A. W. Probing the Valence Orbitals of Transition Metal-Silicon Diatomic Anions: ZrSi, NbSi, MoSi, PdSi and WSi. *Phys. Chem. Chem. Phys.* **2013**, *15* (16), 6068–6079.
(40) Liverman, M.; Beck, S.; Monts, D.; Smalley, R. Fluorescence Excitation Spectrum of the 1au (npi-])]-1ag (o-O) Band of Oxalyl Fluoride in a Pulsed Supersonic Free Jet. *J. Chem. Phys.* **1979**, *70* (1), 192–198.

(41) Gentry, W.; Giese, C. 10-Microsecond Pulsed Molecular-Beam Source and a Fast Ionization Detector. *Rev. Sci. Instrum.* **1978**, *49* (5), 595–600.
(42) Adams, T.; Rockney, B.; Morrison, R.; Grant, E. Convenient Fast Pulsed Molecular-Beam Valve. *Rev. Sci. Instrum.* **1981**, *52* (10), 1469–1472.
(43) Cross, J.; Valentini, J. High Repetition Rate Pulsed Nozzle Beam Source. *Rev. Sci. Instrum.* **1982**, *53* (1), 38–42.
(44) Becker, E.; Bier, K.; Henkes, W. Strahlen Aus Kondensierten Atomen Und Molekeln Im Hochvakuum. *Z. Phys.* **1956**, *146* (3), 333–338.
(45) Moore, J. H.; Davis, C. C.; Coplan, M. A.; Greer, S. A. *Building Scientific Apparatus*; Cambridge University Press: MA, 2009.
(46) Castleman Jr., A.; Weil, K.; Sigsworth, S.; Leuchtner, R.; Keesee, R. Considerations of the Rates and Lifetimes of Intermediate Complexes for the Association of Various Ligands to Metal-Ions - Ag+ and Cu+. *J. Chem. Phys.* **1987**, *86* (7), 3829–3835.
(47) Guo, B.; Wei, S.; Chen, Z.; Kerns, K.; Purnell, J.; Buzza, S.; Castleman Jr., A. Generation of Metal-Carbon and Metal-Nitrogen Clusters with a Laser-Induced Plasma Technique. *J. Chem. Phys.* **1992**, *97* (7), 5243–5245.
(48) Luo, Z.; Smith, J. C.; Woodward, W. H.; Castleman Jr., A. W. Reactivity of Aluminum Clusters with Water and Alcohols: Competition and Catalysis? *J. Phys. Chem. Lett.* **2012**, *3* (24), 3818–3821.
(49) Adams, N.; Smith, D. Selected Ion Flow Tube (SIFT) - Technique for Studying Ion-Neutral Reactions. *Int. J. Mass Spectrom. Ion Process.* **1976**, *21* (3-4), 349–359.
(50) Ferguson, EE; Fehsenfeld, FC; Schmeltekopf, AL. Flowing Afterglow Measurements of Ion-Neutral Reactions. *Adv. At. Mol. Phys.* **1969**, *5*, 1–56.
(51) Vann, W. D.; Bell, R. C.; Castleman Jr., A. W. Gas-Phase Reactions of Nickel and Nickel Oxide Clusters with Nitrogen Oxides. 3. Reactions of Cations with Nitric Oxide. *J. Phys. Chem. A* **1999**, *103* (50), 10846–10850.
(52) Vann, W. D.; Castleman Jr., A. W. Gas-Phase Reactions of Nickel and Nickel Oxide Clusters with Nitrogen Dioxide. 4. Continued Kinetic and Mechanistic Investigation of Nickel Cluster Reactions with NOx Gases. *J. Phys. Chem. A* **1999**, *103* (7), 847–857.
(53) Shukla, A. K.; Futrell, J. H. Tandem Mass Spectrometry: Dissociation of Ions by Collisional Activation. *J. Mass Spectrom.* **2000**, *35* (9), 1069–1090.
(54) Guan, S. Generation of Optimal Excitation Pulses for 2 Energy-Level Systems Using. *J. Chem. Phys.* **1992**, *96* (11), 7959–7964.
(55) Guan, S.; Kim, H.; Marshall, A.; Wahl, M.; Wood, T.; Xiang, X. Shrink-Wrapping an Ion Cloud for High-Performance Fourier-Transform Ion-Cyclotron Resonance Mass-Spectrometry. *Chem. Rev.* **1994**, *94* (8), 2161–2182.
(56) Roach, P. J. The Reactivity of Aluminum Clusters as a Function of Atom Number. PhD Dissertation, The Pennsylvania State University: University Park, PA, 2009.
(57) Rottgen, M. A.; Judai, K.; Antonietti, J. M.; Heiz, U.; Rauschenbach, S.; Kern, K. Conical Octopole Ion Guide: Design, Focusing, and Its Application to the Deposition of Low Energetic Clusters. *Rev. Sci. Instrum.* **2006**, *77* (1), 013302.
(58) Kelly, R. T.; Tolmachev, A. V.; Page, J. S.; Tang, K.; Smith, R. D. The Ion Funnel: Theory, Implementations, and Applications. *Mass Spectrom. Rev.* **2010**, *29* (2), 294–312.

Chapter 3

Boron Substitution in Aluminum Cluster Anions: Magic Clusters and Reactivity with Oxygen

3.1. Introduction

As matter decreases in size the significance of substituting a single atom increases dramatically. Cluster studies have shown that the addition or removal of a single atom can change the geometry and electronic structure of the cluster, which results in drastic changes in the reactive and electronic properties.[1–11] This size-dependent reactivity in simple metal clusters can be understood because their electronic structure can be reconciled within a confined nearly free valence electron picture that leads to grouping of electronic states into shells similar to the case of atoms. The jellium model, where the valence electrons respond to a uniform positive background of the size of the cluster, has been found to provide a fairly realistic framework for understanding the electronic structure of metallic clusters.[12–18]

Bimetallic clusters or clusters with multiple different elements increase the variety of possibilities for new properties and creating new materials.[19–24] However, it is sometimes difficult to predict or even explain the effects of substituting one or more atoms of a different element into a cluster. Significant changes can occur when one atom is substituted with a different element.[25–29] One instance where substitution causes significant changes is in the case of AlB_8^-.[25] Small boron clusters are known to form molecular wheel

geometries; however, the substitution of one aluminum atom for a boron in B_9^- causes the wheel shape to deform into an umbrella shape with the aluminum atom acting as the umbrella handle. Despite the isovalent character and similar properties of boron and aluminum atoms, this substitution drastically changes the properties of the boron cluster. Although we have examples of substitution and its effects, further study is needed to help elucidate the complexities involved on the atomic scale.

Materials composed of aluminum and boron are highly energetic and are often examined to determine how modifying their properties can increase their effectiveness in explosives and propellants.[30–34] Because of their application toward combustion, studies examining the oxidation and these metals can further our progress toward the next generation of advanced combustible nanomaterials. Oxygen is a useful tool in many cluster studies because the ground state of an O_2 molecule is a spin triplet, where the majority spin states have a pair of unpaired electrons while the minority states are unfilled. Any activation of the O_2 molecule therefore requires filling of the minority states and hence a spin transition from the triplet to the singlet state. For the reactivity of clusters in singlet ground states, the above activation entails a spin transition of the metal cluster from spin singlet to spin triplet configuration. This energy is roughly determined by the gap between the highest occupied molecular orbital (HOMO) and the lowest unoccupied molecular orbital (LUMO), and our previous studies have shown that clusters with HOMO-LUMO gap exceeding 1.2 eV are generally nonreactive to oxygen. Consequently, the reactivity with oxygen can probe the shell structure of the clusters and can help identify species, which are highly stable, often termed magic clusters.[15–18,35–40] Magic clusters composed of

energetic materials such as aluminum and boron could provide a safer more controllable combustible that reacts only when provided with precise conditions.

The reaction between oxygen and aluminum cluster anions results in the formation of two Al_2O molecules and an $Al_{(n-4)}^-$ cluster.[8,41–44] Successive reactions with oxygen result in the formation of magic clusters such as Al_{13}^- and Al_{23}^- from once larger clusters. Not only do stable clusters resist the reaction with oxygen but also they are a product of the etching reaction causing their intensity in a mass spectrum to increase.

In the present study, we explored oxygen reactivity with aluminum boride composite clusters. We made a series of Al_n^-, $Al_{n-1}B^-$, and $Al_{n-2}B_2^-$ clusters and compared their reactivity in the presence of oxygen. Those clusters composed of 13 atoms, namely, Al_{13}^-, $Al_{12}B^-$, and $Al_{11}B_2^-$, were all highly resistant to oxidation because of their icosahedral geometry and filled jellium valence shells. Our work shows that the substitution of a boron atom into an aluminum cluster causes the molecule to be slightly less reactive toward oxygen and more stable overall with a larger HOMO-LUMO gap. In addition, boron substitutions do not change the “magic” character of the 13-atom clusters. Other boron-substituted clusters have been studied, and we find that the boron atoms prefer to substitute into the center of the cluster, and this work exemplifies the potential to tailor clusters to desired reactivity or stability by modifying not only the size but also the composition of the cluster.

3.2. Methods

3.2.1. Experimental Methods

The apparatus used in this experiment has been previously described in detail;[8,45,46] however, a brief description is provided in this section. Clusters were formed using a laser vaporization (LaVa) source consisting of the second harmonic of a Nd:YAG laser (532 nm) ablating a rotating aluminum rod (95% aluminum, 5% copper, McMaster Carr). Two inlets allowed the simultaneous introduction of both helium (high purity, Praxair) and diborane (1% diborane in He, Solkatronic) gases to assist in the $Al_nB_m^-$ cluster formation and carry the clusters through a room-temperature laminar flow tube and through a series of electrostatic lenses, octopoles, and quadrupoles (Extrel CMS). Molecular oxygen (compressed, Messer) was introduced to the room temperature laminar flow tube 30 cm downstream from the source and reacted with the clusters over a distance of 60 cm (7.8 ms). To compare the effects of diborane and oxygen, we conducted trials under the following conditions: only helium; helium and oxygen; helium and diborane; and helium, diborane, and oxygen. The total pressure in the flow tube was maintained at ~0.7 Torr with oxygen and diborane (if they were used) set to 0.03 and 0.01 Torr, respectively, while the helium was adjusted to maintain the overall total pressure.

3.2.2. Theoretical Calculations

The electronic structure calculations were carried out using the PBE gradient-corrected density-functional formalism[47] with orbitals represented by a linear combination

of Slater-type orbitals (STO) located at the atomic sites. The particular implementation we have used is the Amsterdam density functional (ADF) set of codes.[48] All structures were allowed full variational freedom and fully optimized without constraint or symmetry. Relativistic effects were taken into account using the zeroth-order regular approximation while employing a TZ2P all-electron basis.[49,50]

3.3. Results and Discussion

Figure 3.1 shows two cluster anion distributions; the distribution in Figure 3.1a is generated by ablating an aluminum rod in helium, while the distribution in Figure 3.1b shows the spectrum while ablating an aluminum rod in helium while a small amount of diborane gas is introduced into the LaVa source. Peaks in the mass spectrum corresponding to the Al_n^-, Al_nB^-, and $Al_nB_2^-$ series (designated by the numbers, lowercase a, and lowercase b, respectively) are formed with the addition of diborane into the cluster source; however, no significant peaks with more than two boron atoms are observed (Figure 3.1b).

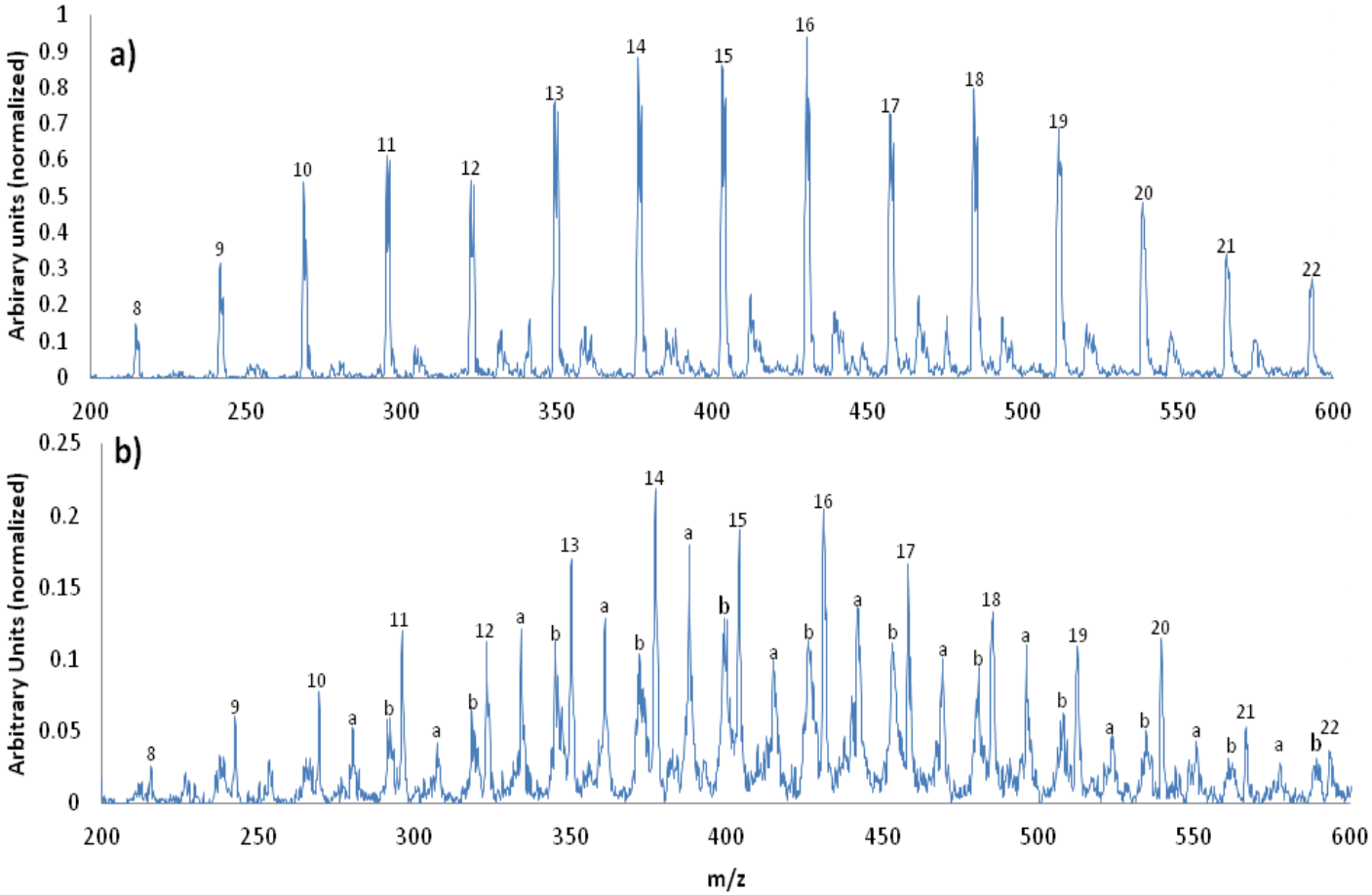

Figure 3.1. a) Distribution of pure aluminum clusters, Al_n^- (minor intensity peaks between the Al_n^- peaks are Cu and Cu_2 additions due to copper contamination), and (b) an aluminum boride spectrum. In panel b, the lowercase a and b denote $Al_nB_1^-$ and $Al_nB_2^-$, respectively, where n is equal to the nearest aluminum cluster to the left.

Because the addition of borane introduces hydrogen as well as boron, there are cluster hydride species in the distribution; however, the resolution of our instrument is sufficient to distinguish between a cluster and its associated hydride. The most prominent peaks in the spectrum are due to pure aluminum or aluminum boride clusters. The metal hydride peaks are not within the scope of this work and are not discussed.

We note that there are mass degeneracies between the peaks of some aluminum boride and pure boron clusters. For example, $Al_{11}B^-$ and B_{28}^- both have a m/z of 308; however, because of the absence of the continuous boron cluster spectrum, B_n^-, and the fact that primary observed peaks are all consistent with Al_n^-, Al_nB^-, and $Al_nB_2^-$, we attribute the mass degenerate peaks in Figure 3.1b to all be aluminum boride species. Further evidence of our peak assignments is found in the oxygen etching experiment shown in Figure 3.2.

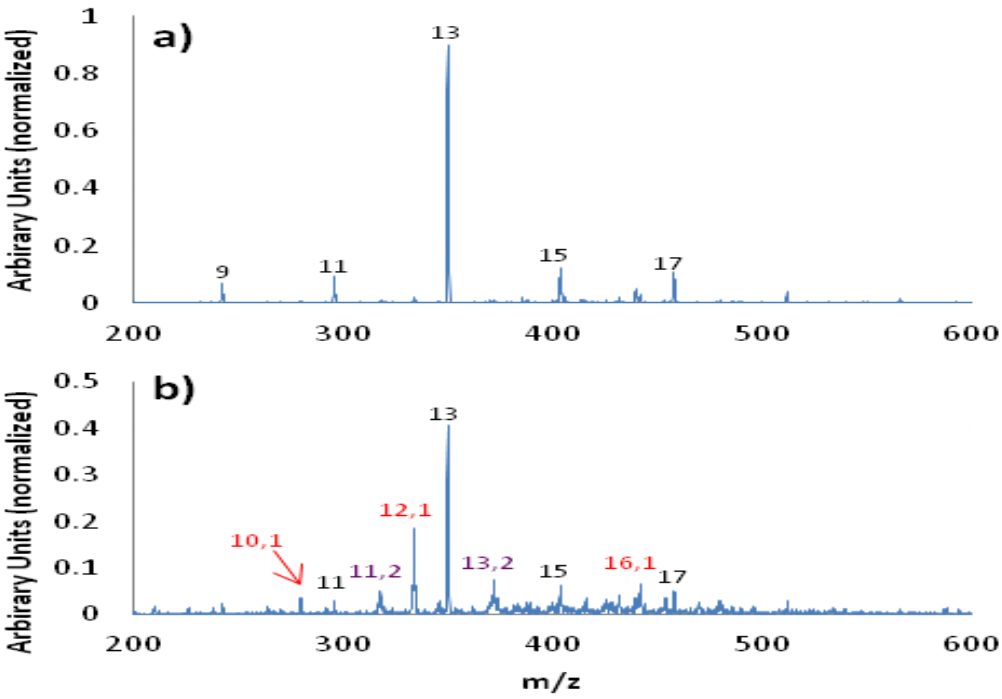

Figure 3.2. Reaction of (a) aluminum and (b) aluminum boride clusters with oxygen. The only species remaining after exposure to oxygen are those clusters with an even number of electrons, although most peaks have still diminished in intensity. Y axis values are arbitrary units.

Products from the reaction of aluminum clusters or aluminum boride clusters and oxygen are displayed in Figure 3.2a, b, respectively. Reactivity between aluminum clusters and oxygen has been previously reported[41–43,51] and the aluminum data collected for this study are provided for a comparison only and not as new information. We see in Figure 3.2a that aluminum clusters with an odd number of atoms (even number of electrons) are more stable in the presence of oxygen, with Al_{13}^- being the most stable due to it having a closed electronic shell. Many previous studies have found the reactivity between clusters with an even number of electrons and an odd number of electrons to differ greatly because of spin conservation effects.[30,43,52–55] A similar pattern is observed in Figure 3.2b, in that

the clusters with an odd number of atoms are less reactive toward oxygen for both pure aluminum clusters and clusters that have incorporated boron atoms.

Because of the geometric and electronic stability of Al_{13}^-, many larger aluminum clusters are etched down to form this as a product. In Figure 3.2b, Al_{13}^-, $Al_{12}B^-$, and $Al_{11}B_2^-$ all show increased intensities after the introduction of oxygen into the flow tube. Interestingly, we see no $Al_{10}B_3^-$ peak in the oxygen reactivity spectrum (Figure 3.2b). If $Al_nB_3^-$ species were present, we suspect that the larger species in the series would etch down to produce the $Al_{10}B_3^-$, and because it is not present in the spectrum we conclude that the source conditions are not favorable to form $Al_nB_3^-$ clusters. All three of the 13-atom clusters are isoelectronic, have large HOMO-LUMO gaps indicating that they should be resistant to oxygen etching, and share similar icosahedral geometries, as shown in Figure 3.3. This provides further evidence of the creation of aluminum boride clusters versus pure boron clusters.

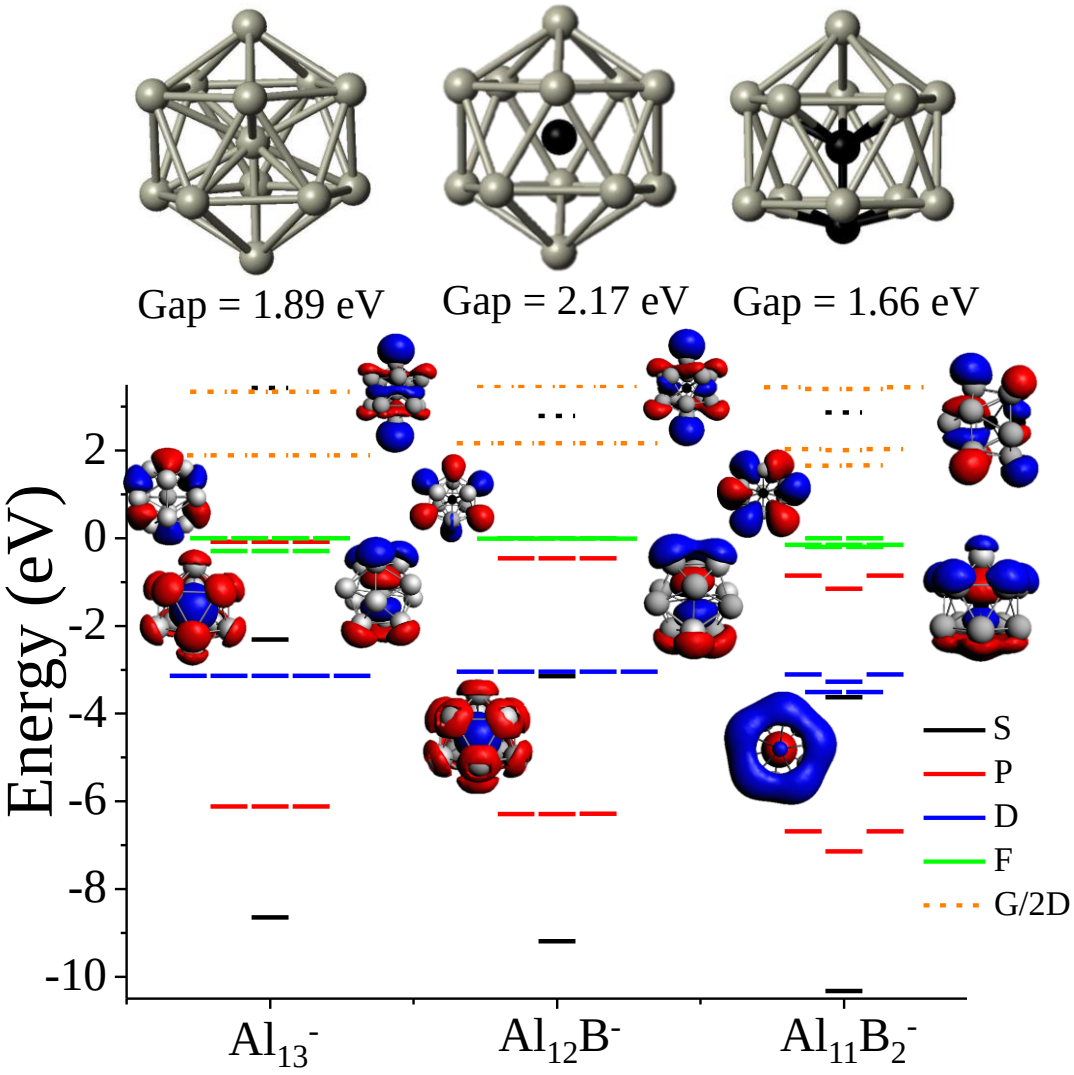

Figure 3.3. Theoretical structures, HOMO-LUMO gaps, and molecular orbital diagrams of Al_{13}^-, $Al_{12}B^-$, and $Al_{11}B_2^-$. Molecular orbitals representative of the 2S, $2P_z$, HOMO, and LUMO are shown.

Figure 3.3 shows the effect of single and double boron substitutions on the electronic shell structure of the 13-atom icosahedral clusters. The substitution of the central aluminum atom with a boron atom increases the HOMO-LUMO gap from 1.89 to 2.17 eV because the boron atom is smaller than the aluminum atom, and it allows the icosahedral structure to contract. The bond length from the central atom to a surface

aluminum atom in Al_{13}^- is 2.65 Å, and the B-Al bond length in $Al_{12}B^-$ is 2.55 Å. However, once a second boron atom is introduced, the HOMO-LUMO gap decreases to 1.66 eV. To understand the effect on the electronic shell structure, we have plotted the one-electron levels in Figure 3.3. All three clusters show well-defined shell structures consistent with the jellium model. Al_{13}^- and $Al_{12}B^-$ both belong to the I_h point group. The main difference in the filled orbitals between Al_{13}^- and $Al_{12}B^-$ is the 2S and 2P shells are slightly lower in energy for $Al_{12}B^-$, which is caused by the central boron atom stabilizing electronic shells with n=2 quantum numbers. A second difference is seen in that the 1G LUMO is pushed up in energy for $Al_{12}B^-$. This is caused by the smaller size of $Al_{12}B^-$, which destabilizes this orbital with a large number of nodes along the surface and explains the larger HOMO-LUMO gap of $Al_{12}B^-$. $Al_{11}B_2^-$ has reduced symmetry of C_{5v} that broadens the 1F and 1G shells. This splitting causes the reduction in the HOMO-LUMO gap of $Al_{11}B_2^-$. The second boron atom also lowers the position of the electronic shells with high n quantum number, 2S, and 2P. The electron affinity of the Al_{13}, $Al_{12}B$, and $Al_{11}B_2$ are 3.35, 3.27, and 3.13 eV, all consistent with these clusters having closed electronic shells.

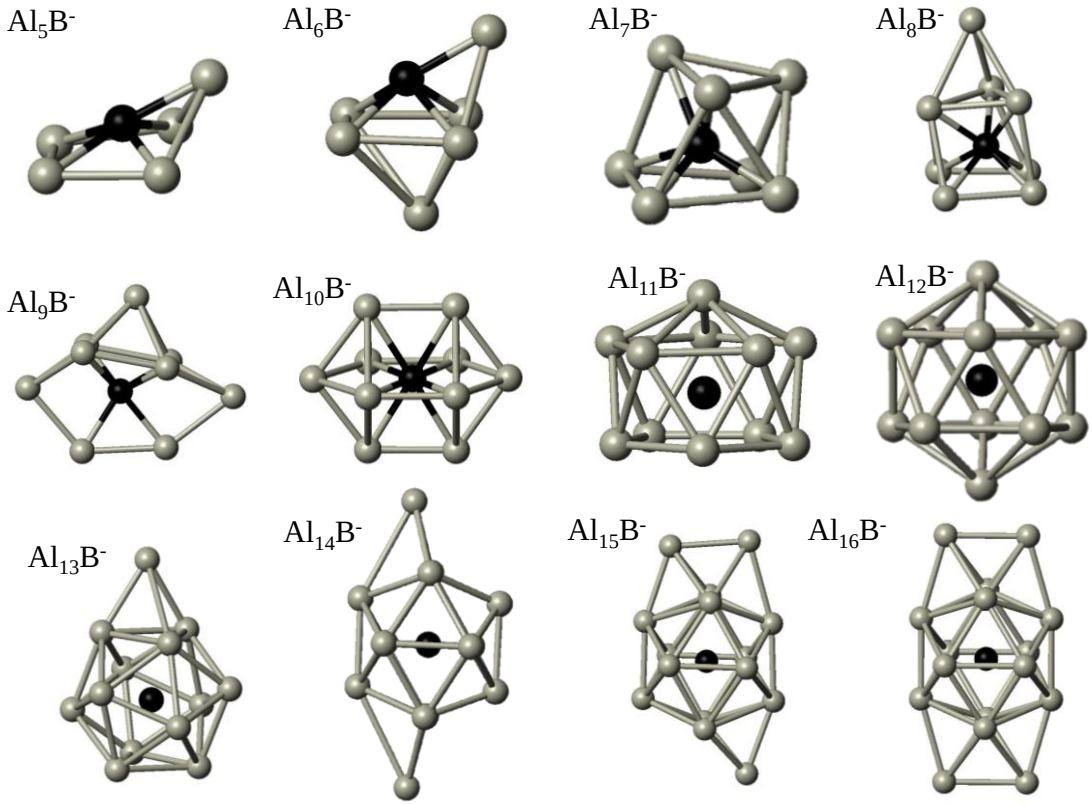

Figure 3.4. Lowest energy structures for Al_nB^-, n=5-16. The Al atoms are gray, and the B atoms are black.

To understand the observed variations in $Al_nB_m^-$ clusters, we have undertaken theoretical investigations of the Al_nB^- and $Al_nB_2^-$ clusters. The lowest energy structures of the Al_nB^- clusters, n=5-16, are shown in Figure 3.4. Al_5B^- has a pseudoplanar geometry, with the aluminum atoms forming a five-membered ring. Al_6B^- has octahedral structure with an aluminum atom decorating one of the boron faces of the octahedron. For the remaining clusters, the boron atom is found to be endohedral, with aluminum surrounding the boron atom. $Al_{10}B^-$ has a highly symmetric structure, with boron sitting at the center of a cuboctahedral structure with vacancies. $Al_{11}B^-$ has an icosahedral structure with a missing face. $Al_{12}B^-$ is the previously discussed icosahedral structure, and the remaining clusters

have icosahedral cores with additional Al atoms decorating their surface. The Al_nB^- clusters for n=11-16 are isostructural with the pure Al_{n+1}^- clusters.

Figure 3.5 shows the lowest energy structures of the $Al_nB_2^-$ series for n=4-15. In all of the cases studied here, the B dimer remains intact. $Al_4B_2^-$ has a planar structure, while $Al_5B_2^-$ is the smallest 3d structure. $Al_8B_2^-$ is the smallest cluster in which both boron atoms are encapsulated inside of the aluminum atoms. $Al_9B_2^-$ has a cuboctahedral structure with one boron on the outside of the cluster, while $Al_{10}B_2^-$ has a double endohedral structure with both boron atoms inside of the aluminum cage. $Al_{11}B_2^-$ has been discussed previously. $Al_{12}B_2^-$, $Al_{14}B_2^-$, and $Al_{15}B_2^-$ are the Al_{14}^-, Al_{16}^-, and Al_{17}^-, clusters with two aluminum atoms replaced by boron.

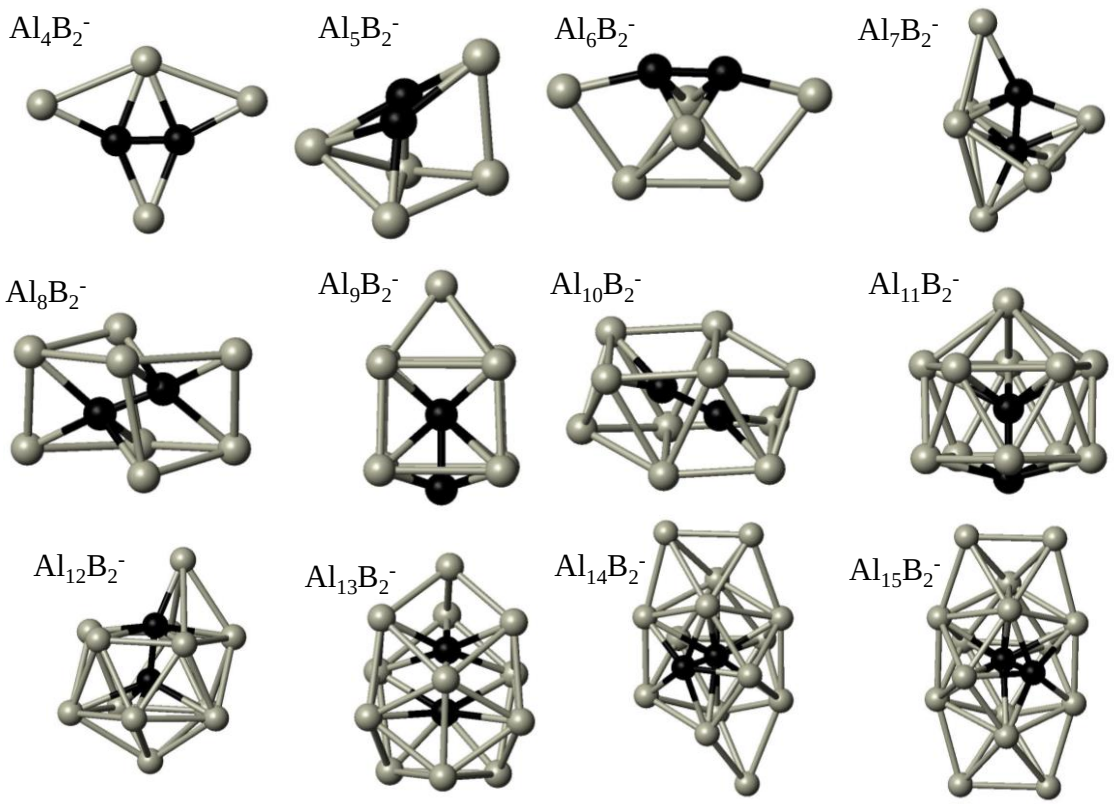

Figure 3.5. Lowest energy structures for $Al_nB_2^-$, n=4-15. The Al atoms are gray and the B atoms are black.

To understand the observed etching spectra in $Al_nB_m^-$ (n+m=1-17, m=0-2) clusters, we next look at their HOMO-LUMO gaps. The Al_n^-, Al_nB^-, and $Al_nB_2^-$ clusters reveal a well-defined even-odd pattern, with the clusters with an odd number of electrons (even number of atoms) having small HOMO-LUMO gaps due to the presence of an unpaired electron, while the clusters with an even number of electrons have varying HOMO-LUMO gaps. The largest HOMO-LUMO gaps are found, as expected, in the closed electronic shell Al_{13}^-, $A_{12}B^-$, and $Al_{11}B_2^-$ clusters. B_2^- has a quartet multiplicity and a HOMO-LUMO gap of 1.59 eV. $Al_{10}B^-$ and $Al_{14}B^-$ have HOMO-LUMO gaps of 1.12 and 1.15 eV, respectively

(Figure 3.6). $Al_{10}B^-$ is observed in the mass spectra; however, no significant peak consistent with $Al_{14}B^-$ is observed. The absence of $Al_{14}B^-$ is likely due to the presence of a particularly reactive isomer in the spectra. Figure 3.7 shows that there is a second isomer of $Al_{14}B^-$ that has two unpaired electrons that is 0.05 eV lower in energy than the lowest energy structure. It is likely that a significant population of the $Al_{14}B^-$ clusters forms this triplet isomer and reacts rapidly with O_2. $Al_{13}B_2^-$ is also observed as a peak in the oxygen etching spectrum, and with a 0.76 eV HOMO-LUMO gap and no unpaired electrons, it is expected to be moderately stable in reaction with O_2.

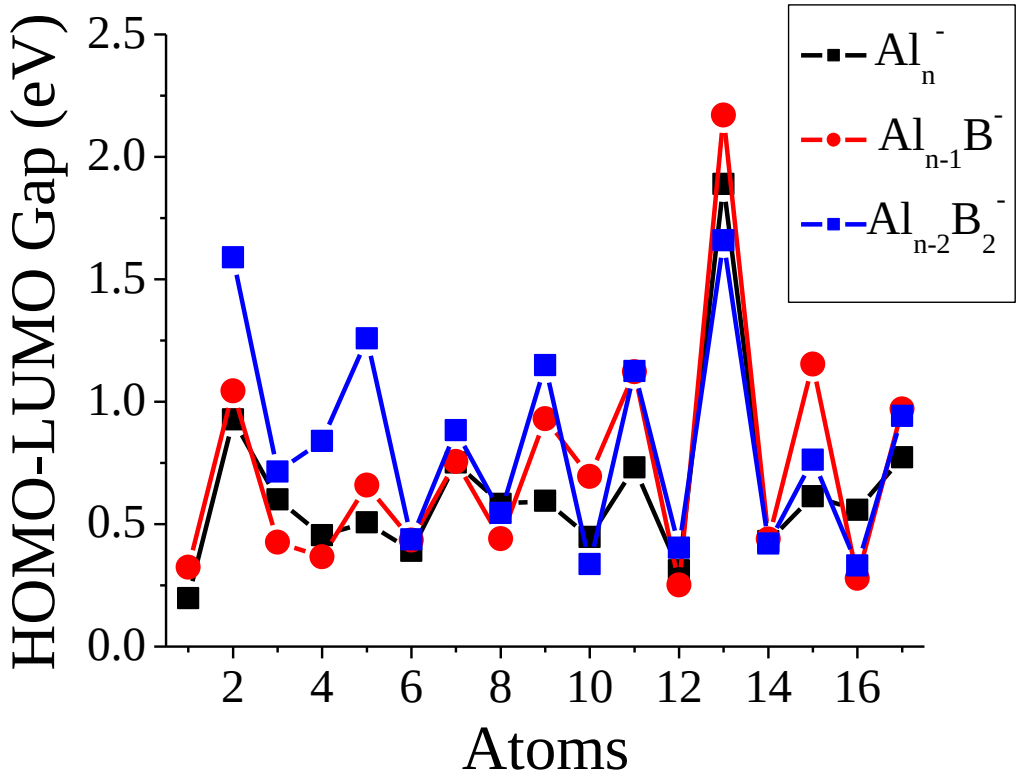

Figure 3.6. HOMO-LUMO gap energies of Al_n^-, Al_nB^-, and $Al_nB_2^-$ for clusters up to 17 atoms.

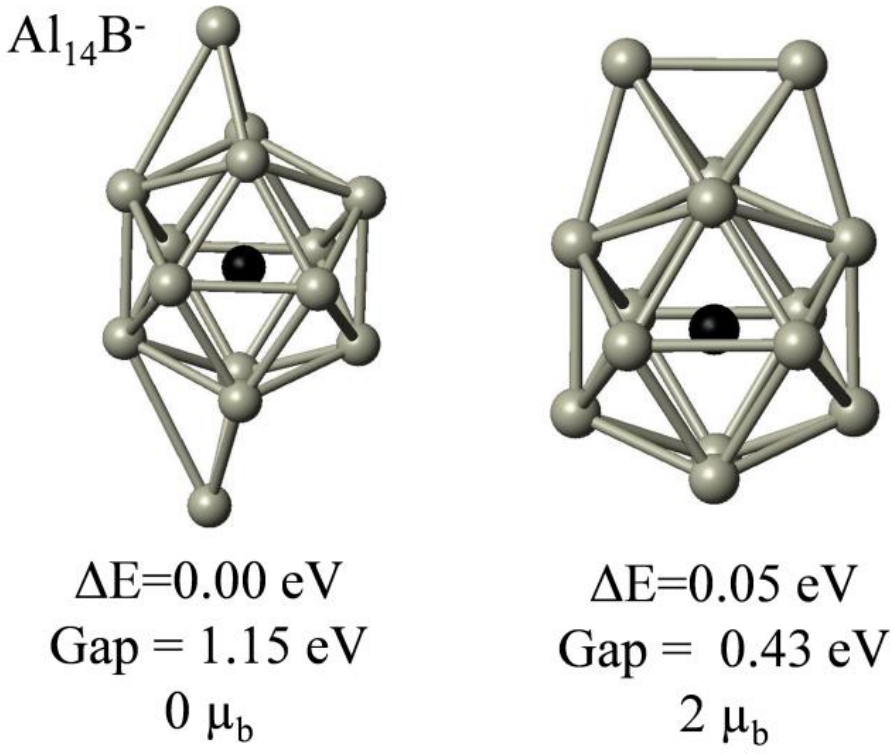

Figure 3.7. Structures, HOMO-LUMO gaps, and number of unpaired electrons in two low-lying isomers of $Al_{14}B^-$.

To understand the stability of the aluminum boride clusters, we have also calculated the energy loss by removing an Al or B atom from the cluster. The removal energy is given by eq. 1. and 2.

$$\Delta E_{Al} = E(Al_nB_m^-) + Al_{n-1}B_m^- + E(Al) \quad (3.1)$$

$$\Delta E_B = E(Al_nB_m^-) + Al_nB_{m-1}^- + E(B) \quad (3.2)$$

Figure 3.8 shows that the B removal energy is significantly larger than the Al removal energy in virtually all of the clusters. A large removal energy corresponds to a cluster with enhanced stability. The most distinct feature in the spectra is the maximum in stability seen

for all of the 13-atom clusters. $Al_{12}B^-$ has the largest Al and B removal energies of all of the clusters considered here. The 11-atom and 17-atom clusters show a small enhancement as compared with neighboring sizes.

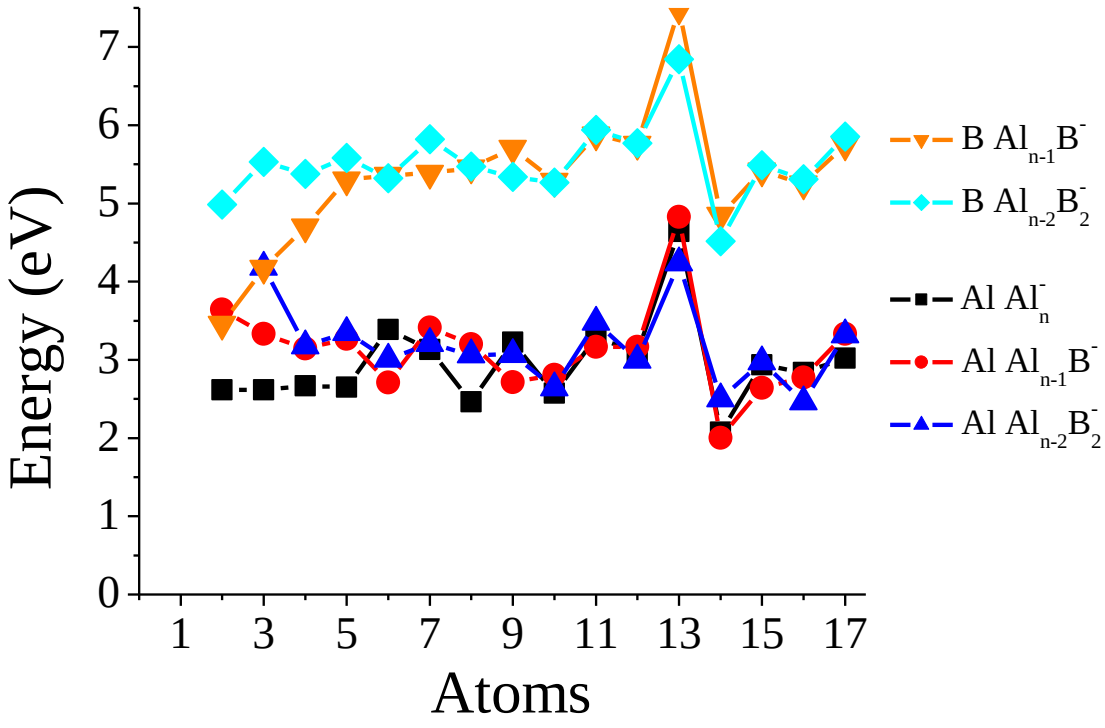

Figure 3.8. Calculated removal energies for B and Al atoms from the Al_n^-, Al_nB^-, and $Al_nB_2^-$ clusters.

The presence of boron poses a new question about the products of an aluminum boride cluster anion reacting with oxygen. Previous work has shown that the most likely products when oxidizing aluminum cluster anions are Al_{n-4}^- and two Al_2O molecules.[8,41] As boron is introduced into the aluminum cluster, will the reaction now yield AlBO or B_2O leaving groups or do the aluminum atoms remain the preferred binding and reactive sites? Figure 3.9 provides the oxidation energy released from the reaction of the aluminum and

aluminum boride clusters with oxygen as a function of the most likely products. With the exception of small aluminum boride clusters (Al_nB^-, n<4), the most energetically favorable leaving group for the boride clusters is the loss of two Al_2O molecules. So energetically, the oxygen etching is expected to remove Al from the cluster and results in smaller clusters with the same number of boron atoms. The boron atom in these clusters is generally protected from direct reaction with oxygen due to its central location within the cluster. Smaller $Al_nB_2^-$ clusters often have boron atoms in the surface positions and will no longer be protected by a layer of aluminum atoms, which may yield different results for the most favorable leaving group.

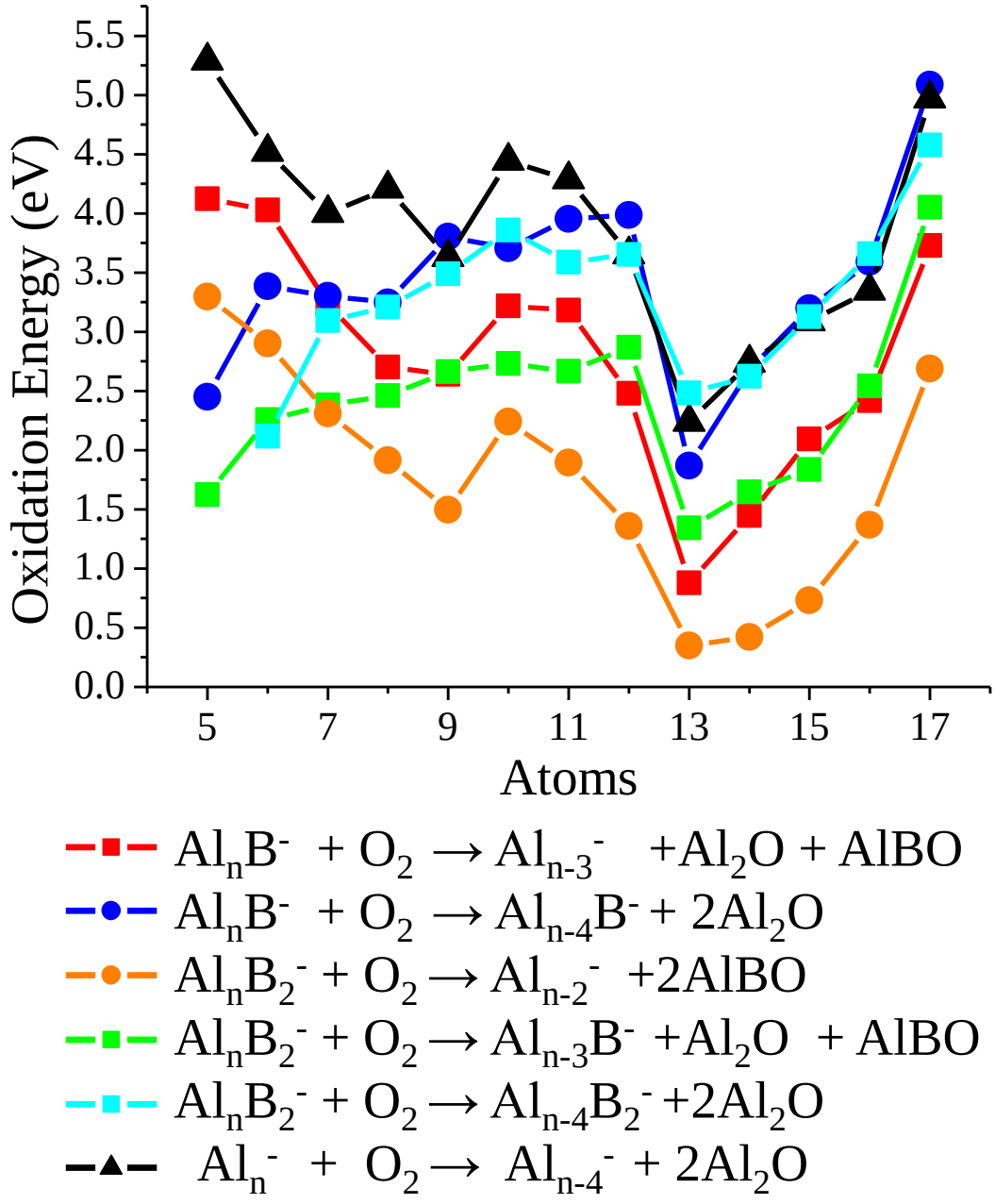

Figure 3.9. Comparison of the oxidation energy released from the reactions of aluminum and aluminum boride with different possible leaving groups (Al_2O and AlBO).

It is interesting to note that the even-odd pattern found in the HOMO-LUMO gaps (Figure 3.6) that control the kinetics of the oxidation of the clusters is not apparent in the

oxidation energy of the different clusters. These clusters are all metastable with respect to reaction with oxygen; however, the clusters with a large spin excitation energy are protected from reaction because of spin accommodation. The 13-atom icosahedral clusters have the lowest oxidation energy, and the 17-atom clusters that are expected to form the 13-atom clusters after oxidation have the largest oxidation energies. While the kinetics of the reactivity of aluminum boride clusters with oxygen are primarily due to the spin excitation energy the reaction products for the reacting species are determined primarily by the energetics of the reaction that involves both geometric and electronic components.

3.4. Conclusions

We have investigated the reactivity of aluminum boride cluster anions with oxygen and demonstrated that the introduction of boron atoms into aluminum clusters decreases their reactivity with O_2. $Al_{12}B^-$ and $Al_{11}B_2^-$ are found to be resistant to reactivity with O_2 due to their closed electronic shell. The ground state of an Al_{13}^- is a perfect icosahedron where the surface bonds are ~2.79 Å and the radial bonds are 2.65 Å, while in $Al_{12}B^-$ the surface bonds are 2.68 Å and the radial bonds are 2.55 Å. The substitution of the central Al by the smaller B relieves the surface strain and the compact structure pushes the 1G LUMO shell up in energy, resulting in the BAl_{12}^- cluster having a larger HOMO-LUMO gap than Al_{13}^-. $Al_{11}B_2^-$ breaks the icosahedral symmetry, resulting in the broadening of the electronic shell structure and a smaller HOMO-LUMO gap. Previous studies have shown that the enhanced stability and high electron affinity of $Al_{12}B$ make it a potential candidate to form cluster assembled solids, such as $(Al_{12}B)Cs$.[56]

3.5. References

(1) Castleman Jr., A. W.; Khanna, S. N. Clusters, Superatoms, and Building Blocks of New Materials. *J. Phys. Chem. C* **2009**, *113* (7), 2664–2675.

(2) Li, X.; Wu, H. B.; Wang, X. B.; Wang, L. S. S-P Hybridization and Electron Shell Structures in Aluminum Clusters: A Photoelectron Spectroscopy Study. *Phys. Rev. Lett.* **1998**, *81* (9), 1909–1912.

(3) Sanchez, A.; Abbet, S.; Heiz, U.; Schneider, W.-D.; Häkkinen, H.; Barnett, R. N.; Landman, U. When Gold Is Not Noble: Nanoscale Gold Catalysts. *J Phys Chem A* **1999**, *103* (48), 9573–9578.

(4) Hagen, J.; Socaciu, L. D.; Le Roux, J.; Popolan, D.; Bernhardt, T. M.; Wöste, L.; Mitrić, R.; Noack, H.; Bonačić-Koutecký, V. Cooperative Effects in the Activation of Molecular Oxygen by Anionic Silver Clusters. *J. Am. Chem. Soc.* **2004**, *126* (11), 3442–3443.

(5) Li, X.; Grubisic, A.; Eustis, S.; Wang, D.; Lectka, T.; Gantefoer, G. F.; Bowen, K. H.; Burgert, R.; Schnoeckel, H. The Reaction of Aluminum Cluster Anions with Tetrakis(dimethylamino)ethylene (TDMAE): Insertion of an Aluminum Anion into a C-N Bond. *Chem. Phys. Lett.* **2009**, *481* (4-6), 190–193.

(6) Kaden, W. E.; Wu, T.; Kunkel, W. A.; Anderson, S. L. Electronic Structure Controls Reactivity of Size-Selected Pd Clusters Adsorbed on TiO2 Surfaces. *Science* **2009**, *326* (5954), 826–829.

(7) Grubisic, A.; Li, X.; Gantefoer, G.; Bowen, K. H.; Schnoeckel, H.; Tenorio, F. J.; Martinez, A. Reactivity of Aluminum Cluster Anions with Ammonia: Selective Etching of Al-11(-) and Al-12(-). *J. Chem. Phys.* **2009**, *131* (18), 184305.

(8) Roach, P. J.; Woodward, W. H.; Castleman Jr., A. W.; Reber, A. C.; Khanna, S. N. Complementary Active Sites Cause Size-Selective Reactivity of Aluminum Cluster Anions with Water. *Science* **2009**, *323* (5913), 492–495.

(9) Luo, Z.; Smith, J. C.; Woodward, W. H.; Castleman Jr., A. W. Reactivity of Aluminum Clusters with Water and Alcohols: Competition and Catalysis? *J. Phys. Chem. Lett.* **2012**, *3* (24), 3818–3821.

(10) Li, W.-L.; Romanescu, C.; Galeev, T. R.; Wang, L.-S.; Boldyrev, A. I. Aluminum Avoids the Central Position in AlB9- and AlB10-: Photoelectron Spectroscopy and Ab Initio Study. *J. Phys. Chem. A* **2011**, *115* (38), 10391–10397.

(11) Reber, A. C.; Roach, P. J.; Woodward, W. H.; Khanna, S. N.; Castleman, A. W. Edge-Induced Active Sites Enhance the Reactivity of Large Aluminum Cluster Anions with Alcohols. *J. Phys. Chem. A* **2012**, *116* (30), 8085–8091.

(12) Bellary, V. P.; Balasubramanian, T. K.; Shetty, B. J. On the Wigner-Witmer Correlation Rules for a Homonuclear Diatomic Molecule with the like Atoms in Identical Atomic States. *Pramana-J. Phys.* **1998**, *51* (3-4), 445–452.

(13) Ahlrichs, R.; Ehrhardt, C.; Lakenbrink, M.; Schunck, S.; Schnockel, H. Molecular Po2cl - Matrix Ir Investigations and Abinitio Scf Calculations. *J. Am. Chem. Soc.* **1986**, *108* (13), 3596–3602.

(14) Bergeron, D. E.; Roach, P. J.; Castleman Jr., A. W.; Jones, N.; Khanna, S. N. Al Cluster Superatoms as Halogens in Polyhalides and as Alkaline Earths in Iodide Salts. *Science* **2005**, *307* (5707), 231–235.
(15) Deheer, W. The Physics of Simple Metal-Clusters - Experimental Aspects and Simple-Models. *Rev. Mod. Phys.* **1993**, *65* (3), 611–676.
(16) Knight, W. D.; Clemenger, K.; Deheer, W. A.; Saunders, W. A.; Chou, M. Y.; Cohen, M. L. Electronic Shell Structure and Abundances of Sodium Clusters. *Phys. Rev. Lett.* **1984**, *52* (24), 2141–2143.
(17) Brack, M. The Physics of Simple Metal-Clusters - Self-Consistent Jellium Model and Semiclassical Approaches. *Rev. Mod. Phys.* **1993**, *65* (3), 677–732.
(18) Perdew, J.; Tran, H.; Smith, E. Stabilized Jellium - Structureless Pseudopotential Model for the Cohesive and Surface-Properties of Metals. *Phys. Rev. B* **1990**, *42* (18), 11627–11636.
(19) Nößler, M.; Mitrić, R.; Bonačić-Koutecký, V.; Johnson, G. E.; Tyo, E. C.; Castleman, A. W. Generation of Oxygen Radical Centers in Binary Neutral Metal Oxide Clusters for Catalytic Oxidation Reactions. *Angew. Chem.* **2010**, *122* (2), 417–420.
(20) Claridge, S. A.; Castleman, A. W.; Khanna, S. N.; Murray, C. B.; Sen, A.; Weiss, P. S. Cluster-Assembled Materials. *ACS Nano* **2009**, *3* (2), 244–255.
(21) Roach, P. J.; Woodward, W. H.; Reber, A. C.; Khanna, S. N.; Castleman, A. W. Crystal Field Effects on the Reactivity of Aluminum-Copper Cluster Anions. *Phys. Rev. B* **2010**, *81* (19), 195404.
(22) Luo, Z.; Grover, C. J.; Reber, A. C.; Khanna, S. N.; Castleman, A. W. Probing the Magic Numbers of Aluminum–Magnesium Cluster Anions and Their Reactivity toward Oxygen. *J. Am. Chem. Soc.* **2013**, *135* (11), 4307–4313.
(23) Roy, X.; Lee, C.-H.; Crowther, A. C.; Schenck, C. L.; Besara, T.; Lalancette, R. A.; Siegrist, T.; Stephens, P. W.; Brus, L. E.; Kim, P.; et al. Nanoscale Atoms in Solid-State Chemistry. *Science* **2013**, *341* (6142), 157–160.
(24) Mandal, S.; Reber, A. C.; Qian, M.; Weiss, P. S.; Khanna, S. N.; Sen, A. Controlling the Band Gap Energy of Cluster-Assembled Materials. *Acc. Chem. Res.* **2013**, *46* (11), 2385–2395.
(25) Galeev, T. R.; Romanescu, C.; Li, W.-L.; Wang, L.-S.; Boldyrev, A. I. Valence Isoelectronic Substitution in the B-8(-) and B-9(-) Molecular Wheels by an Al Dopant Atom: Umbrella-Like Structures of AlB7- and AlB8-. *J. Chem. Phys.* **2011**, *135* (10), 104301.
(26) Jian-Bing, G.; Xiang-Dong, Y.; Huai-Qian, W.; Hui-Fang, L. Structural, Electronic, and Magnetic Properties of Boron Cluster Anions Doped with Aluminum: BnAl- (2 <= N <= 9). *Chin. Phys. B* **2012**, *21* (4), 043102.
(27) Cheng, S.-B.; Berkdemir, C.; Castleman Jr., A. W. Observation of D-P Hybridized Aromaticity in Lanthanum-Doped Boron Clusters. *Phys. Chem. Chem. Phys.* **2014**, *16* (2), 533–539.
(28) Jiang, Z. Y.; Yang, C. J.; Li, S. T. Structures and Stability of B-Doped Al Clusters: AlnB and AlnB2 (n=1-7). *J. Chem. Phys.* **2005**, *123* (20), 204315.

(29) Huynh, M. T.; Alexandrova, A. N. Persistent Covalency and Planarity in the BnAl6-n2- and LiBnAl6-N- (n=0-6) Cluster Ions. *J. Phys. Chem. Lett.* **2011**, *2* (16), 2046–2051.
(30) Reber, A. C.; Khanna, S. N.; Roach, P. J.; Woodward, W. H.; Castleman Jr., A. W. Spin Accommodation and Reactivity of Aluminum Based Clusters with O-2. *J. Am. Chem. Soc.* **2007**, *129* (51), 16098–16101.
(31) Bazyn, T.; Krier, H.; Glumac, N.; Shankar, N.; Wang, X.; Jackson, T. L. Decomposition of Aluminum Hydride Under Solid Rocket Motor Conditions. *J. Propuls. Power* **2007**, *23* (2), 457–464.
(32) Risha, G. A.; Son, S. F.; Yetter, R. A.; Yang, V.; Tappan, B. C. Combustion of Nano-Aluminum and Liquid Water. *Proc. Combust. Inst.* **2007**, *31* (2), 2029–2036.
(33) Nakajima, A.; Kishi, T.; Sugioka, T.; Kaya, K. Electronic and Geometric Structures of Aluminum-Boron Negative Cluster Ions (AlnB−m). *Chem. Phys. Lett.* **1991**, *187* (3), 239–244.
(34) Kawamata, H.; Negishi, Y.; Nakajima, A.; Kaya, K. Electronic Properties of Substituted Aluminum Clusters by Boron and Carbon Atoms (AlnBm−/AlnCm−); New Insights into S–p Hybridization and Perturbed Shell Structures. *Chem. Phys. Lett.* **2001**, *337* (4–6), 255–262.
(35) Castleman Jr., A.; Guo, B.; Wei, S. Metallo-Carbohedrenes - a New Class of Molecular Clusters. *Int. J. Mod. Phys. B* **1992**, *6* (23-24), 3587–3594.
(36) Pedersen, J.; Bjornholm, S.; Borggreen, J.; Hansen, K.; Martin, T.; Rasmussen, H. Observation of Quantum Supershells in Clusters of Sodium Atoms. *Nature* **1991**, *353* (6346), 733–735.
(37) Pilgrim, J.; Duncan, M. Metallo-Carbohedrenes - Chromium, Iron, and Molybdenum Analogs. *J. Am. Chem. Soc.* **1993**, *115* (15), 6958–6961.
(38) Gong, X.; Kumar, V. Enhanced Stability of Magic Clusters - a Case-Study of Icosahedral Al12X, X=B, Al, Ga, C, Si, Ge, Ti, As. *Phys. Rev. Lett.* **1993**, *70* (14), 2078–2081.
(39) Liu, R. S.; Liu, F. P.; Dong, K. J.; Zheng, C. X.; Liu, H. R.; Peng, P.; Li, J. Y. Size Distributions and Magic Number Characteristics of Cluster Configurations Formed During Solidification Processes of Liquid Metal Al. *Sci. China Ser. E-Technol. Sci.* **2006**, *49* (2), 172–187.
(40) Desireddy, A.; Kumar, S.; Guo, J.; Bolan, M. D.; Griffith, W. P.; Bigioni, T. P. Temporal Stability of Magic-Number Metal Clusters: Beyond the Shell Closing Model. *Nanoscale* **2013**, *5* (5), 2036–2044.
(41) Leuchtner, R.; Harms, A.; Castleman Jr., A. Aluminum Cluster Reactions. *J. Chem. Phys.* **1991**, *94* (2), 1093–1101.
(42) Leuchtner, R.; Harms, A.; Castleman Jr., A. Thermal Metal Cluster Anion Reactions - Behavior of Aluminum Clusters with Oxygen. *J. Chem. Phys.* **1989**, *91* (4), 2753–2754.
(43) Burgert, R.; Schnoeckel, H.; Grubisic, A.; Li, X.; Stokes, S. T.; Bowen, K. H.; Gantefor, G. F.; Kiran, B.; Jena, P. Spin Conservation Accounts for Aluminum Cluster Anion Reactivity Pattern with O(2). *Science* **2008**, *319* (5862), 438–442.

(44) Woodward, W. H.; Reber, A. C.; Smith, J. C.; Khanna, S. N.; Castleman, A. W. Carbonyl Bond Cleavage by Complementary Active Sites. *J. Phys. Chem. C* **2013**, *117* (15), 7445–7450.
(45) Guo, B.; Wei, S.; Chen, Z.; Kerns, K.; Purnell, J.; Buzza, S.; Castleman Jr., A. Generation of Metal-Carbon and Metal-Nitrogen Clusters with a Laser-Induced Plasma Technique. *J. Chem. Phys.* **1992**, *97* (7), 5243–5245.
(46) Castleman Jr., A.; Weil, K.; Sigsworth, S.; Leuchtner, R.; Keesee, R. Considerations of the Rates and Lifetimes of Intermediate Complexes for the Association of Various Ligands to Metal-Ions - Ag+ and Cu+. *J. Chem. Phys.* **1987**, *86* (7), 3829–3835.
(47) Perdew, J. P.; Burke, K.; Ernzerhof, M. Generalized Gradient Approximation Made Simple. *Phys. Rev. Lett.* **1996**, *77* (18), 3865–3868.
(48) Te Velde, G.; Bickelhaupt, F. M.; Baerends, E. J.; Fonseca Guerra, C.; van Gisbergen, S. J. A.; Snijders, J. G.; Ziegler, T. Chemistry with ADF. *J. Comput. Chem.* **2001**, *22* (9), 931–967.
(49) Lenthe, E. van; Baerends, E. J.; Snijders, J. G. Relativistic Regular Two-component Hamiltonians. *J. Chem. Phys.* **1993**, *99* (6), 4597–4610.
(50) Van Lenthe, E.; Ehlers, A.; Baerends, E.-J. Geometry Optimizations in the Zero Order Regular Approximation for Relativistic Effects. *J. Chem. Phys.* **1999**, *110* (18), 8943–8953.
(51) Woodward, W. H.; Eyet, N.; Shuman, N. S.; Smith, J. C.; Viggiano, A. A.; Castleman Jr., A. W. Aluminum Cluster Anion Reactivity with Singlet Oxygen: Evidence of Al-9(-) Stability. *J. Phys. Chem. C* **2011**, *115* (20), 9903–9908.
(52) Behler, J.; Delley, B.; Lorenz, S.; Reuter, K.; Scheffler, M. Dissociation of O-2 at Al(111): The Role of Spin Selection Rules. *Phys. Rev. Lett.* **2005**, *94* (3), 036104.
(53) Schwarz, H. On the Spin-Forbiddeness of Gas-Phase Ion-Molecule Reactions: A Fruitful Intersection of Experimental and Computational Studies. *Int. J. Mass Spectrom.* **2004**, *237* (1), 75–105.
(54) Ashman, C.; Khanna, S. N.; Pederson, M. R. Reactivity of AlnC Clusters with Oxygen: Search for New Magic Clusters. *Chem. Phys. Lett.* **2000**, *324* (1-3), 137–142.
(55) Ahlrichs, R.; Elliott, S. D. Clusters of Aluminium, a Density Functional Study. *Phys. Chem. Chem. Phys.* **1999**, *1* (1), 13–21.
(56) Ashman, C.; Khanna, S. N.; Liu, F.; Jena, P.; Kaplan, T.; Mostoller, M. (BAl12)Cs:mA Cluster-Assembled Solid. *Phys. Rev. B* **1997**, *55* (23), 15868–15873.

Chapter 4

Matrix Isolation Cavity Ring-down Spectroscopy

4.1. Introduction

As discussed earlier in Chapter 1, the transition of incorporating gas-phase clusters into condensed-phase materials while still retaining their advantageous gas-phase properties, remains an obstacle in the development of cluster assembled materials. A more thorough understanding of cluster interactions in a controlled environment is needed to reveal how the properties of clusters of different size and composition are affected when brought into contact with other species. Understanding cluster-cluster interactions and also cluster-molecule interactions will help bridge the gap that remains between gas-phase studies and materials.

There two questions that arise when designing an experiment for the controlled interaction between clusters. First, how do you collect and contain the subject matter; and second, how do you study the subject matter? Clusters have been deposited on surfaces in many studies, but the electronic and geometric structures are perturbed or completely changed from the gas-phase due to the interactions with the surface.[1–6] A common technique used to isolate and control reactive species is matrix isolation which uses an inert matrix to encapsulate the desired molecule with limited perturbation to its geometry or electronic structure. Matrix isolation also allows the controlled diffusion of molecules for study of interactions. These two properties make matrix isolation an appealing choice for the study of cluster interactions and formation of cluster assembled materials. Choosing an

appropriate analytical technique requires that the sensitivity of the technique is appropriate for the number density of the clusters contained and can provide the information necessary to differentiate individual clusters from those bonding or interacting with other species. The total number of clusters made in many cluster sources would not be sufficient for most analytical detection techniques. Common cluster production ranges in the pico ampere range which equates to roughly 10^5 - 10^7 clusters per second. Some instruments report cluster currents into the nano or micro ampere range but often those do not have the low pressures required for clean depositions.[7] The high sensitivity needed for such small amounts of clusters limits the analytical techniques sufficient for this experimentation. Spectroscopy can be a highly sensitive technique and a useful tool in understanding and differentiating the electronic properties of small molecules and clusters. The sensitivity required excludes many spectroscopic methods; however, cavity ring-down spectroscopy is one method that is highly sensitive and the setup is relatively simple and inexpensive.

Background information on both matrix isolation and cavity ring-down spectroscopy are provided in this chapter along with the prospects of their union into matric isolation cavity ring-down spectroscopy (MICRDS). The experimental design is discussed along with the evolution of MICRDS experimentation. This novel technique is not found in the literature and holds great potential to help bridge the gap between gas-phase cluster studies and cluster assembled materials.

4.2 Matrix Isolation

In the 1950s George Pimentel, of University of California, Berkeley, developed the technique of matrix isolation to study reactive and unstable species.[8,9] In the last 60 years, matrix isolation has grown from a technique mainly used in physical chemistry to incorporating many chemistry fields including inorganic, organic, and biochemistry.[10] The main purpose of matrix isolation began as a way to contain and control reactive and unstable species. Matrix isolation continues to expand to more molecules and has extended to study the interactions between molecules as they diffuse throughout the matrix.

The general setup of a matrix isolation experiment is fairly straightforward. It begins with a cryogenically cooled surface onto which a mixture of matrix molecules and the molecules to be studied are deposited. As the molecules collide with the surface, they are cooled and trapped preventing diffusion or evaporation (Figure 4.1). There are many factors associated with successful matrices including temperature, matrix composition, diffusion, evaporation, and others.

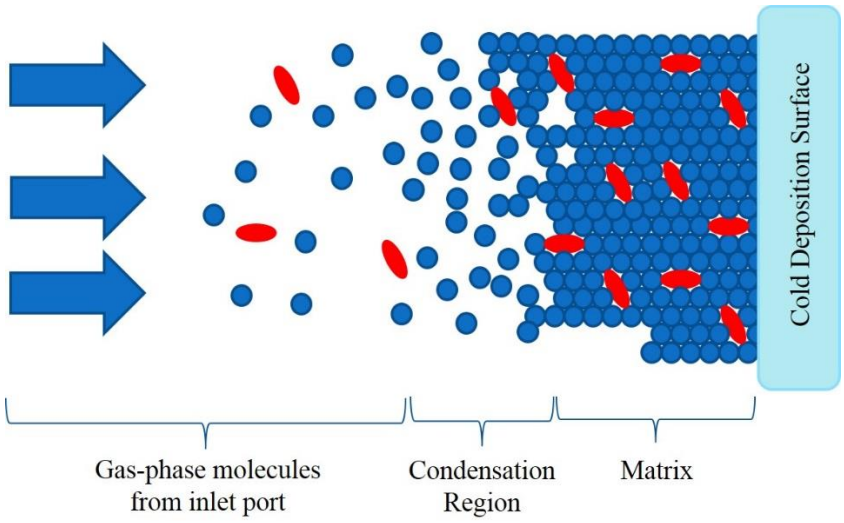

Figure 4.1. Diagram of the growth of a rigid matrix of inert molecules and trapped species. When the atoms/molecules collide with the cold surface their orientations and positions are fixed in the manner upon arrival.

The first consideration in matrix isolation is the composition of the matrix. Typical matrix materials are noble gasses because they are highly inert, relatively inexpensive, and they are spectroscopically invisible for much of the electromagnetic spectrum. In addition to the noble gasses, molecules such as CO, CCL_4, SF_6, N_2, and CO_2 have been used as matrix materials.[11] Noble gasses are often preferred because many matrix isolation studies are performed in the infrared region where the atomic nature of the gas lacks vibrational modes. The other gases are more often used when liquid nitrogen rather than liquid helium is used as the coolant.

The rigidity of the matrix is an important consideration for matrix isolation studies. The general rule among practitioners of matrix isolation is that the temperature of the deposition surface must be below one half of the melting point of the matrix gas ($0.5T_m$ in Kelvin) in order to prevent excess diffusion and sublimation.[10,11] A sufficiently low

temperature around one third the melting point will prohibit almost all diffusion of the reactive or unstable molecules. Raising the temperature of the matrix to a point between $0.3T_m$ and $0.5T_m$ initiates diffusion and the trapped molecules are allowed to interact. Temperatures above 0.5Tm result in the diffusion of trapped molecules to the boundaries of microcrystalline structures within the matrix and rapid sublimation rates. The deposition rate can affect the temperature and diffusion within the matrix. If material is deposited too quickly, the heat transfer between the cryostat and the matrix will be insufficient and the matrix will become non-rigid. Optimal matrix deposition rates range between 2-5 mmol/hour.[12]

To exploit the benefits of controlled diffusion within a matrix, trapped molecules should be isolated from any other trapped species. If all of the trapped molecules are isolated from each other the original data will be free of any complex or reaction products, thus making identification of those products that much easier after the matrix is annealed to allow diffusion. Table 4.1 shows the percentage of isolated trapped molecules according to various mixing ratios.

Table 4.2. Probability of isolation of trapped molecules in a matrix. Table adapted from reference **[11]**.

Matrix Ratio (Matrix/Trapped)	**100**	**1000**	**10000**
% Trapped Isolated	88.6	98.8	99.9
% Tapped Non-Isolated	11.4	1.2	0.1

These percentages are statistical estimates and will vary depending on the size of the trapped molecules, whether they occupy a single or multiple sites, and the strength of the

interactions between the trapped molecules. Performing sets of trials with varying matrix ratios can result in similar results as trials with diffusion.

4.3 Cavity Ring down Spectroscopy

Cavity ring-down spectroscopy (CRDS) originally arose from a technique that measured the reflectivity of mirrors. In the early 1980s Herbelin et al. and Anderson et al. developed the original techniques that measured the reflectivity of a pair of high-reflectivity mirrors.[13,14] As mirror development progressed, with higher reflectivities, these techniques were adapted and honed to allow more accurate and precise reflectivity measurements. Reflectivities were obtained by measuring the amount of light lost in the cavity between the set of mirrors. This method led scientists to adapt cavity lossmeters which measured mirror reflectivity to the study of dilute gaseous samples.

Traditional single-pass absorption spectroscopies are very effective and accurate when the concentration and molar absorptivities of the sample lie within a particular range. A solution with too high of an absorbance and there is no distinction between the small amount of transmission and zero transmission. On the other hand, a solution with too small of an absorbance will result in an undetectable difference between the incident light and the transmitted light. The concentration limits will vary widely depending on the molar absorptivities of the analytes. Smaller concentrations can and must be used for those samples with high absorptivities and the opposite is true for samples with low absorptivities.

Trace and ultra-trace analysis are needed for production/determination of pure materials, environmental monitoring, genetic engineering, biotechnology, and others.[15] Several trace analysis methods are available with varying levels of difficulty and cost, some examples include laser induced fluorescence, inductively coupled plasma mass spectrometry, second harmonic generation spectroscopy, surface-enhanced Raman spectroscopy, and others.[15–20] Analytical chemistry continues to strive for lower and lower detection limits to satisfy new manufacturing demands, governmental regulations, and unknown analysis/identification.

CRDS is a unique absorption spectroscopy in that it does not measure the direct absorption of a sample but the rate of absorption within an optical cavity. It is most commonly used to measure the absorption spectrum of static gas-phase samples but recently has been used in other applications including solid samples and surface characterization.[21–23] There are several reasons for using CRDS rather than some other spectroscopic method in this section: 1) CRDS is a relatively inexpensive and easy technique experimentally, 2) CRDS is immune to laser power fluctuations, 3) CRDS is a direct, linear technique which simplifies the determination of absorption cross sections and concentrations.

The basic setup of a CRD spectrometer consists of two highly reflective mirrors aligned such that they create an optical cavity as shown in Figure 4.2.

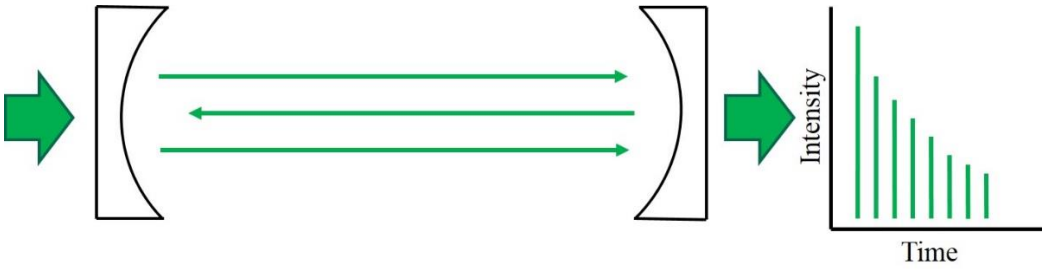

Figure 4.2. Diagram showing an optical cavity created by two highly reflective mirrors. A laser pulse enters through one of the mirrors and then is reflected back and forth through the cavity. The graph on the right shows the exponential decay of the intensity of the light that escapes the cavity for each round trip.

Optical cavities vary in arrangement using pairs of plane or concave mirrors or sometimes using two different plane, concave, or convex mirrors. The only requirement for a stable optical cavity is that the mirrors satisfy the requirement

$$0 \leq g_1 g_2 \leq 1 \tag{4.1}$$

where g_1 and g_2 are the mirrors that define the cavity and g represents

$$g_n = 1 - \frac{L}{R_n} \tag{4.2}$$

where L is the distance between the mirrors and Rn is the radius of curvature of each mirror. Light enters through the back of one mirror and then is reflected back and forth between the two mirrors. As the light travels between the mirrors, some light is transmitted through the mirrors and detected most often with a photomultiplier tube. The intensity of the light inside the cavity decreases following an exponential decay that corresponds to the reflectivity of the mirror set. The distance between each detected pulse corresponds to the time it takes the original light pulse to travel one round trip within the cavity (Figure 4.3).

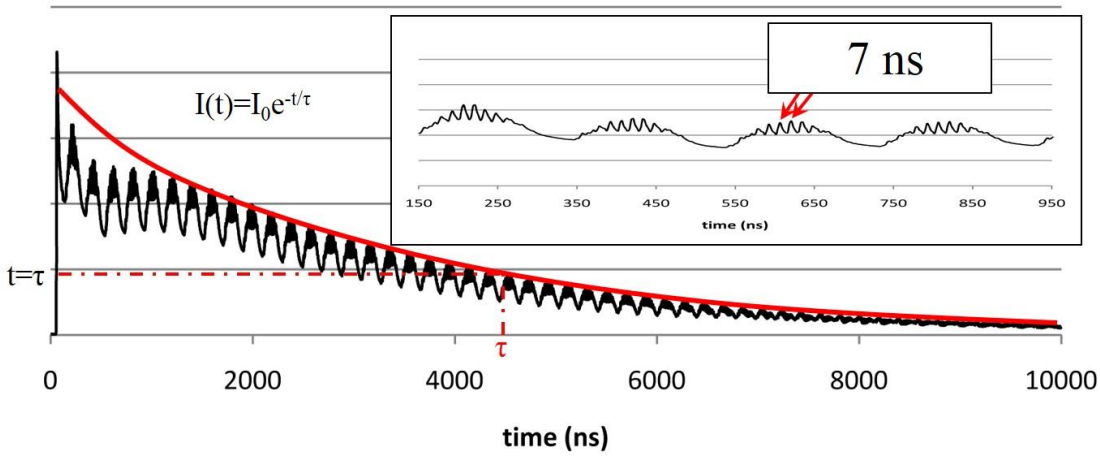

Figure 4.3. A cavity ring down spectrum showing the exponential decay and the ring-down time where t=τ. The inset is an enlarged portion of the decay showing the distance between the peaks is 7ns which corresponds to our cavity length.

The principles that govern CRDS originate from the same that govern any traditional absorption spectroscopy. The Beer-Lambert law describes the relationship between the absorption cross section of the analyte, its concentration, and the amount of light that is lost:

$$I_t = I_0 \exp(-\sigma LN) \tag{4.3}$$

where it is the transmitted light, Io the incident light, σ is the absorption cross section of the analyte, L is the path length of the absorbing medium, and N is the number density of the analyte. The total amount of light lost in eq. 4.3 is represented by the term σLN. The term must be altered for CRDS to account for the light lost for each round trip through the

optical cavity. Taking into account two reflections per round trip and the number of round trips in an empty optical cavity, eq. 4.3 can be modified to fit the conditions of CRDS.

$$I(t) = I_0 \exp\left\{-(2)(1-R)\left(\frac{tc}{2L}\right)\right\} \tag{4.4}$$

R is the reflectivity of the mirrors, t is time, c is the speed of light, and L is the length of the cavity (distance between the mirrors). The ring-down time constant τ, is defined as the time when $I_t = I_0 e^{-1}$, leaving

$$\tau = \frac{L}{c(1-R)} = \frac{t_r}{2(1-R)} \tag{4.5}$$

where t_r is the round trip time of the cavity. This constant provides us with the equation seen in Figure 4.3:

$$I(t) = I_0 e^{\frac{-t}{\tau}} \tag{4.6}$$

When an absorbing species is introduced in the optical cavity a new source of light loss must be factored into eq. 4.4. In this explanation only light absorbed by the analyte will be discussed, there may be light loss due to scattering processes but it will not be addressed in this section. The amount of light lost due to the absorber is dependent upon the absorbance cross section and the number density of the absorber found within the volume of the light within the cavity. Introducing this new method of light loss eq. 4.4 evolves into

$$I(t) = I_0 \exp\left\{-(2)[(1-R) + (\alpha L)]\left(\frac{tc}{2L}\right)\right\} \tag{4.7}$$

where α is the absorption coefficient (σN) of the system. The new ring-down time is expressed as

$$\tau = \frac{t_r}{2[(1-R)+\alpha L]} \tag{4.8}$$

and combining eq. 4.5 and 4.8 we can solve for the absorption coefficient

$$\alpha = \sigma N = \frac{1}{c}\left(\frac{1}{\tau_1} - \frac{1}{\tau_2}\right) \tag{4.9}$$

where τ_1 and τ_2 represent the ring-down times for the cavity with the absorbing analyte and the empty cavity, respectively.

4.4 MICRDS

4.4.1 Experimental

The experimental setup for MICRDS has gone through several stages of redesign through trial and error as would be expected for most new analytical instruments. The original idea began as a technique to perform MICRDS on cluster ions mass selected from the current instrument described in Chapter 2. The instrument from Chapter 2 was modified to include a cryostat for matrix isolation deposition and an optical cavity for CRDS. To begin the coupling of matrix isolation and cavity ring-down spectroscopy, several experimental questions were considered. What matrix will be used and how will it affect the clusters contained? How will having a surface rather than a gas influence CRDS and what can be done to minimize its effects?

4.4.1.1 The Matrix

A cryostat suitable for both liquid helium and nitrogen was acquired from Janis Research Company (Janis St-400) which is connected to a temperature controller (LakeShore Model 331). The controller provides a current of electricity to the cryostat which allows a range of temperatures, the lower limit controlled by the temperature of the cryogen and the upper limit determined by the material components of the cryostat (much higher than would ever be necessary in matrix isolation). This cryostat is designed and incorporated to accomplish two tasks. First, a surface attached to the cryostat must be able cool and capture any incident atoms or molecules that collide with the deposition surface. Second, to transfer the sample between the ion beam and the optical cavity while maintaining the vacuum integrity. The separation of the cluster ion beam and the optical cavity requires that the deposition surface be moved up to 18" and rotated at least 90° to successfully intercept both the ion and optical beams. The rotation and translation of the surface are manipulated by stepper-motors controlled by computer software.

One of the most important factors regarding matrix isolation is the composition of the matrix. Most matrix isolation experiments use a compressed helium cryostat which allows surface temperatures of 10-30 K, this enables the use of gases such as argon, krypton, and nitrogen as the matrix. Liquid helium is an expensive cryogen and its lower temperatures sometimes result in matrices that scatter more light. Liquid nitrogen, however, is relatively inexpensive and due to its higher temperature may facilitate in the formation of more optically transparent matrices. The main problem with using liquid nitrogen is that the majority of matrix gases have melting temperatures that are too low to

properly solidify at 77 K. Of the remaining candidates, sulfur hexafluoride (SF_6) seemed the best candidate.

SF_6 is not commonly used as a matrix gas anymore because of the availability of recirculated helium cryostats. The lower temperatures enables use of the noble gases which are atomic and do not interfere with vibrational spectroscopy. Though SF_6 would not be suitable for IR spectroscopy, it is optically transparent over the wavelength range intended for cluster study (UV-vis). Other advantages of SF_6 are its high ionization energy and low electron affinity which would prevent charge transfer between the clusters and the matrix. SF_6 is inert and very stable and has two crystal structures. The freezing temperature of SF_6 is reported at 222 K; however, at 95 K the solid changes from a body centered cubic (bcc) lattice to a monoclinic structure (Figure 4.4).[24–26] The monoclinic structure is much denser and more rigid leading to the potential that slight annealing of a SF_6 matrix to the phase boundary may allow increased diffusion within the matrix.

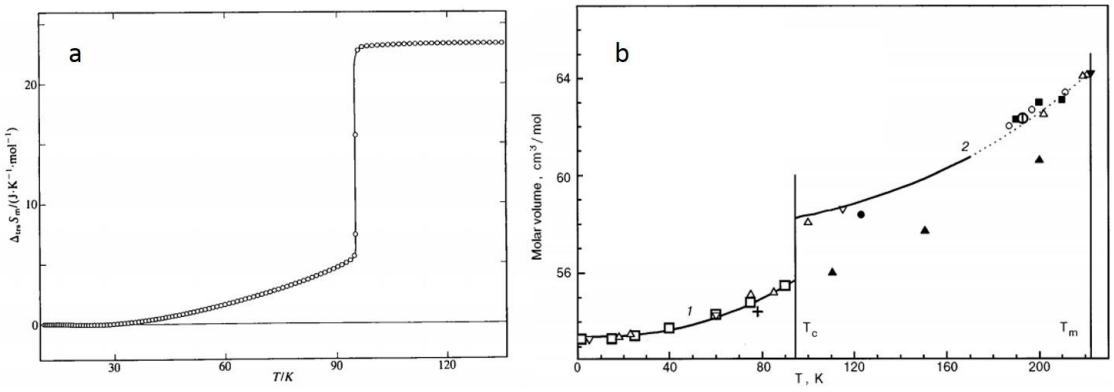

Figure 4.4. a) The temperature dependence of SF6 molar entropy and b) the temperature dependence of molar volume. Notice that each breaks continuity at 95 K where the crystal structure of SF_6 changes from bcc to a monolithic structure. Figure adapted from references [24,26].

4.4.1.2 Cavity Ring-down Chamber

An additional chamber was added to the mass spectrometer and serves as the cavity ring-down chamber. The chamber is approximately one meter in length and is enclosed by two 8" flanges each with a quartz optical window allowing light to enter and exit the cavity. The third harmonic of a Nd-YAG laser (Spectra Physics Quanta Ray Pro-250) pumps a Spectra Physics Master Oscillator Power Oscillator (MOPO-730) which can provide coherent light from 200-1800 nm with the power of 100 mj/pulse and a linewidth of 0.2 cm^{-1} is coupled into the optical cavity by a collection of broadband mirrors (Edmund NT48-016) and irises which are used to align the beam through the center of the two optical windows in the flanges. High reflectivity mirror sets (reflectivity >99.99%, and radius of curvature 1 m) were obtained from CRD Optics Inc. ranging in wavelengths from 355-550 nm. These mirrors are mounted in a custom designed and built mirror exchanger that allows up to nine sets of CRD mirrors to be interchanged and individually aligned without ever breaking vacuum (Figure 4.5).

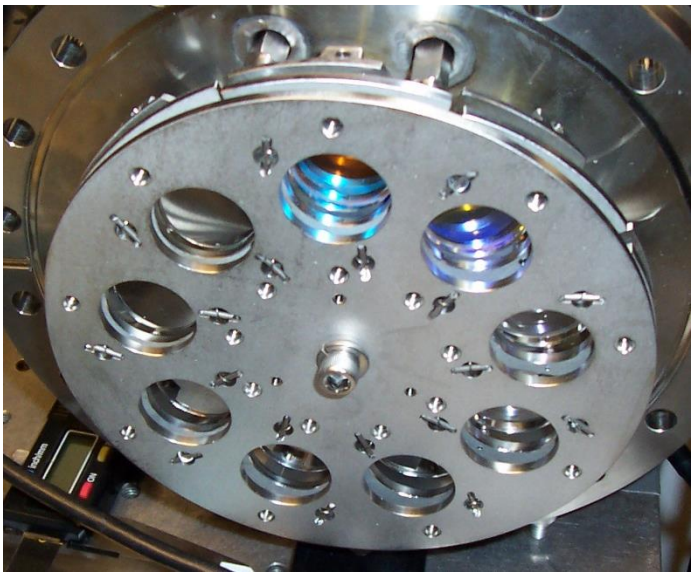

Figure 4.5. A picture of the mirror exchanger. It is made up of an attachment plate, 9 wedges, and 9 sub-wedges. Each wedge and sub-wedge are attached to the plate by a spring which also acts as counter-pressure during alignment. A wedge and sub-wedge are connected as a gimbal mount.

Drawings and further details of the mirror exchanger are included in the appendix. The total distance between the two mirrors is 1.055 m. The reflectivities of the mirrors and the length of the optical cavity result in an effective path length of 21 km enabling much more sensitive measurements than a traditional UV-vis spectrometer with common path lengths of 1 cm. The light which exits the back of the cavity is detected using a photomultiplier tube (Hamamatsu H6780). The gain of the detector is modified to accommodate reflectivity losses with respect to wavelength by a custom LabVIEW program which controls and synchronizes the laser, MOPO, and data collection.

4.4.1.3 The Deposition Surface

The application of CRDS was only recently expanded to the study of solid samples.[27–33] One of the main reasons that solid sample studies are not widespread in the CRDS community is that the addition of multiple surfaces and larger structures (larger than gas phase molecules) often results in more light scatter, reflections, and ultimately light loss. If those obstacles can be overcome, CRDS has shown itself as a useful analytical tool. Great consideration must be taken when selecting the substrate material and its position/orientation within the optical cavity.

The orientation of the window will limit the possible choices in substrate material. Currently, there are two common arrangements for CRDS solid sample studies. The first being a total internal reflection spectroscopy, where the optical cavity passes through a prism onto which a sample is deposited. The light never passes through the sample, but the sample is exposed to the evanescent wave when the light reflects within the prism, this is strictly a surface probing technique. The second method is to have the light pass through a sample with direct absorbance of the entire sample. Different methods will call for different substrate materials. For example, birefringence in the optical material will render it useless for some arrangements such as in a total internal reflection or if the window is at the Brewster's angle. The choice of using the Brewster's angle or orienting the window perpendicular to the optical axis of the cavity is a competition between ease of alignment and loss of light. The Brewster's angle will be more forgiving if only slightly misaligned; however, only p-polarized light is transmitted through the window which reduces total signal. Birefringent materials will change the polarization of the light with each round trip

which will quickly deplete the light in the cavity. If the substrate is parallel to the optical axis of the cavity, polarization can be neglected. The concern that arises when the substrate is perpendicular is the light lost through reflectivity. However, if the substrate should be positioned such that its front and back surfaces satisfy eq. 4.1 and form stable optical cavities with the two mirrors, any light that is reflected from the surface rather than transmitted will remain in the cavity. Essentially, the substrate is dividing the original optical cavity into six: two between the front mirror and each of the substrate faces (front and back), one between the faces of the substrate, two between the rear mirror and each face of the substrate, and one between the two mirrors.

Generally speaking, the addition of a perpendicular surface in the optical cavity should not affect the overall ring-down times because the light will be maintained within the optical cavity made by the two mirrors and the light will still have the same number of interactions with the mirrors.[34,35] One effect worthy of notice is that the initial portion of the exponential decay will not fit the rest of the decay. The decay normalizes once the amount of light on each side of the window equilibrates. This effect only impacts the ring-down times and not the calculated absorbance cross sections or the concentration as the error will cancel out. Accurate ring-down times can be determined by setting a delay-time for the data collection to bypass the inaccurate portion of the exponential decay. The delay-time should be determined by the reflectivity of the window.

One last comment on the position of the window within the cavity should be mentioned. The placement of the window should be in the middle of the cavity in order to

maximize the ring-down times. This was determined experimentally with the data shown in Figure 4.6.

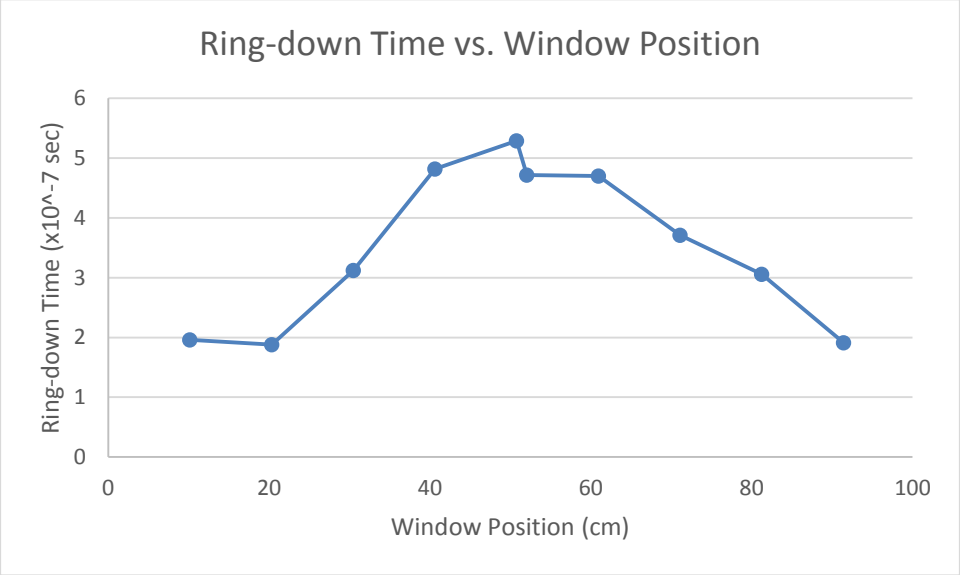

Figure 4.6. The effect of window position on ring down time. As the window approaches the center of the cavity, the maximum ring-down time is observed. The position is reported in distance away from the first mirror, with the total distance between the two mirrors being 1 m.

The data was only to confirm that as the window approaches one of the two mirrors, the number of interactions between the light and the mirrors and windows increases which in turn increases the rate at which light is lost.

Several materials have been successfully incorporated into optical cavities. The window must be of the highest caliber so as to have minimal light scatter from imperfections. Some examples that have been used are silica (SiO_2), BK7 glass, and yttria stabilized zirconia (YSZ).The appropriate material must be transparent (non-absorbing) for

the intended spectroscopy. For the purposes of this work and the instrumental setup, a sapphire window (Meller Optics, SCD1717-01A) is used as the deposition substrate

An ion pump (Varian Star Cell) was initially used to attain a higher vacuum for cleaner deposition. Despite higher vacuum conditions, the ion pump introduced other negative effects that more than outweighed the benefits of higher vacuum. The primary reason for the discontinued use of the ion pump was a resulting etched pattern on the cryostat and the sapphire surface after SF_6 was introduced into the chamber. After one of the initial matrix generation trials, it was found that irreparable damage was done to the sapphire substrate and the only conditions that have ever caused this effect was an engaged ion pump during SF_6 deposition. Without the ion pump, pressures of 10^{-9} Torr are normal and the benefits of higher vacuum were offset by the optical damage to the transparent deposition surface. Further details regarding the design and effectiveness of the above system are described in the next section (section 4.4.2).

4.4.2 MICRDS Trials

The purpose of this section in to guide the reader through the various MICRDS approaches taken and how the initial idea of MICRDS has evolved to its current form. Some of the more prominent experimental failures are also discussed to show how they instructed and provided course corrections in the process of MICRDS development and to educate others so the same mistakes will not be made. A quote often attributed to Thomas Edison seems very appropriate to describe the process involved in the development of a new technique and instrument, “I have not failed 10,000 times. I have not failed once. I

have succeeded in proving that those 10,000 ways will not work. I will find the way that will work."[36]

Initial trials of the MICRDS system included a systematic approach to ensure that each part functioned properly. A drawing of the MICRDS instrument is provided in Figure 4.7.

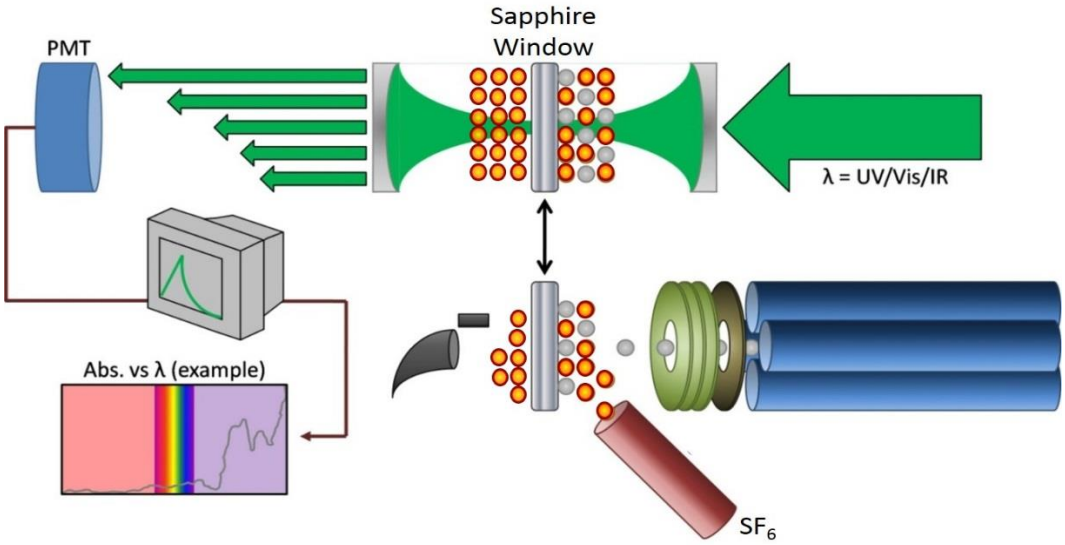

Figure 4.7. Drawing of the MICRDS instrument. This is coupled to the detection portion of the instrument from Chapter 2. The matrix and the clusters are co-deposited on the cold sapphire window, which is then transported into the optical cavity.

The cavity ring-down system was the first checked to confirm that absorbing species on the sapphire window would be detected. Fluorescein 548 (Exciton) is a common laser dye that has high absorptivity around 500nm. The sapphire window was dipped into a dilute solution of fluorescein 548 in methanol and the methanol allowed to evaporate. The sapphire was then secured to the cryostat in the vacuum chamber. The instrument was

pumped down to vacuum and a cavity ring down spectrum of the fluorescein was taken. A spectrum of a more concentrated solution of fluorescein (>0.1 M) was taken using a commercial UV-vis spectrometer to provide a reference spectrum. Figure 4.8 shows the normalized spectra of both the CRD and UV-vis instruments.

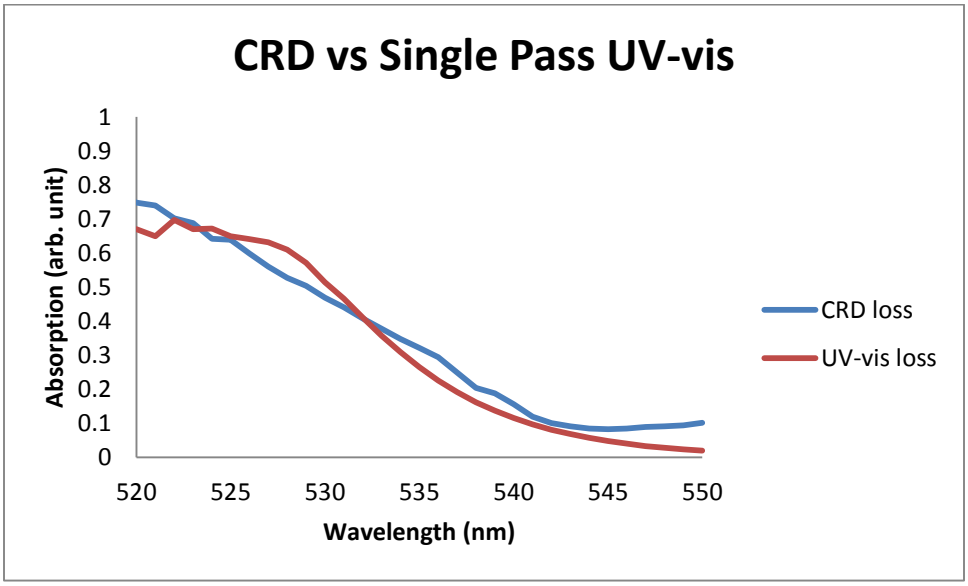

Figure 4.8. Absorption spectra taken using both single pass and CRD techniques. In the wavelength range of 490-520, both samples were too concentrated; however, the drop from almost total absorption to total transmission, beginning around 520 nm, is seen for both techniques.

The fluorescein trials confirmed the accuracy of the CRD spectrometer in detecting absorbing molecules on the sapphire surface. Once the CRD was successful, depositions of aluminum cluster anions in a matrix were attempted

Original efforts in MICRDS were focused on observing Al_{13}^- clusters deposited in a SF_6 matrix. Al_{13}^- was chosen for three reasons. First, Al_{13}^- has remarkable stability and resists reactivity with most reagents including oxygen. Second, some peaks in the

theoretical absorption spectrum (Figure 4.9) overlap the applicable wavelength range of the CRD mirrors and the laser (450-600 nm). Finally, the intensity of Al_{13}^- can be inflated by introducing oxygen in the flow tube to increase its number density in the matrix.

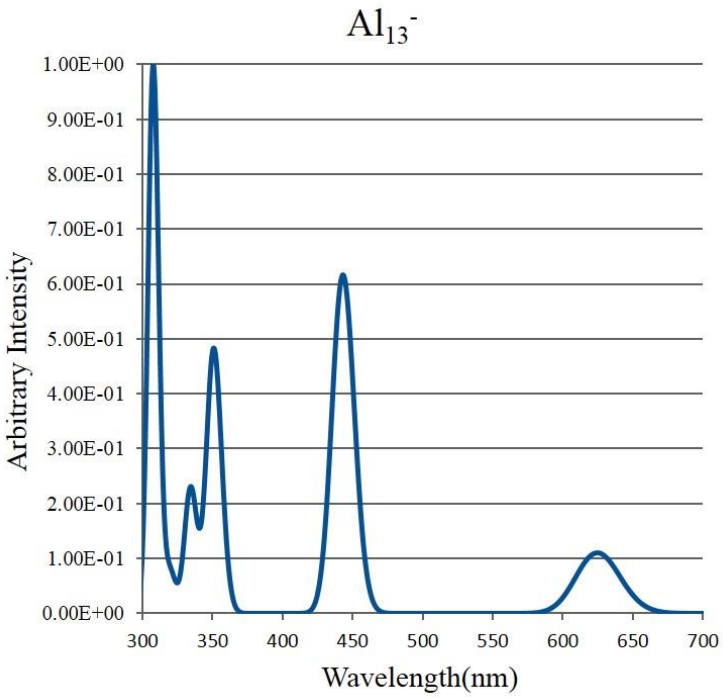

Figure 4.9. The theoretical UV-vis absorption spectrum of Al_{13}^-. This information was provided by collaborations with Shiv Khanna from Virginia Commonwealth University.

Previous studies have shown that when Al_n^- clusters are exposed to molecular oxygen an etching effect occurs where each oxygen atom will strip two aluminum atoms from the cluster.[37–39] This process repeats as often as oxygen collides with the clusters until a stable cluster is formed. These clusters are stabilized either by their geometry or their electronic structure or both and resist further etching by oxygen. Exposing Al_n^- clusters to oxygen can

increase the Al_{13}^- signal by several orders of magnitude. As mentioned at the beginning of this chapter, we may expect as many as 10^8 Al_{13}^- clusters per second. The sensitivity requirements of the instrument require between 10^{11}-10^{13} total clusters for detectable absorption (resulting in 10s to 100s ppm light lost). Without any strategies to increase signal a 10 hour deposition would require 10^8 clusters per second, the upper limit of cluster production. If less than perfect conditions exists days may be required for accumulation of enough clusters. The ability to increase signal by even one order of magnitude drastically reduces deposition times and makes Al_{13}^- a prime candidate for deposition.

Unfortunately, no Al_{13}^- trials resulted in any observable absorption in a SF_6 matrix. The first question that arose was if there was sufficient signal. Most depositions lasted 8 hours or more. Increasing the signal using oxygen was attempted with no noticeable effects. In a different attempt to increase the number of clusters deposited onto the surface, the mass selection feature was disabled and all cluster anions were allowed to intercept the deposition surface. A single trial resulted in the data shown in Figure 4.10.

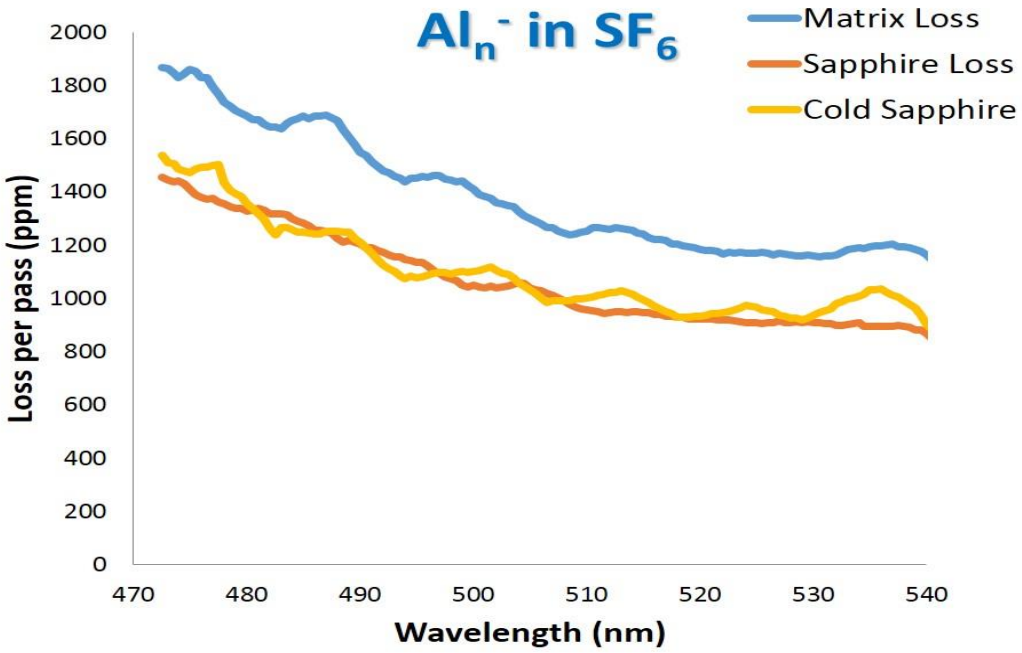

Figure 4.10. Absorption spectrum of Al_n^- in a SF_6 matrix. The yellow spectrum represents a blank of the sapphire at liquid nitrogen temperatures, the blue the spectrum with the Aln- and SF6 matrix, and the orange represents the sapphire after the sapphire has returned to room temperature and the matrix has sublimed.

The data in Figure 4.10 could have represented an ensemble absorption of many different clusters or Mie scattering of clusters that are of similar size with the wavelengths of light. However, these data were never reproducible with most depositions resulting in no absorption due to a matrix and is most likely an artifact of some portion of the experiment. This conclusion is further justified by exploring the effects of charge buildup inside a matrix as more clusters are trapped.

If the charges of the anions trapped in the matrix are not neutralized, how many clusters can be trapped before the total charge within the matrix begins to repel incoming

clusters? Originally this threshold was thought to be far above the concentrations needed for CRD detection but on further investigation charge buildup presents a formidable challenge. Because our matrix is deposited onto a circular window the charge buildup will most closely follow the example of an electric field generated by a charged disk. The electric field produced by a flat, non-conducting, circular disk can be calculated using[40]

$$E = \frac{\sigma}{2\varepsilon_0}\left(1 - \frac{z}{\sqrt{z^2 - R^2}}\right) \tag{4.10}$$

where σ is the charge density, ε_0 is the permittivity constant, R is the radius of the disk, and z is the distance from the charged disk (along the central axis). Using this equation, once 2.5×10^6 clusters are accumulated, incoming clusters will experience ≈1 V of electric potential 1 nm away from the charged disk. If we look at the potential created by the number of clusters needed in the matrix, 10^{11}, the potential raises to >4 kV. This field is surely enough to deflect any incoming clusters considering that the clusters have been thermalized to <1 eV.

Electric charge buildup in a matrix is a significant obstacle in any attempt to study cluster ions using MICRDS. Ions are commonly studied using matrix isolation; however, they are deposited as neutrals and using various processes are ionized after contained in the matrix.[41–43] Other groups have studied cluster neutrals by neutralizing clusters as they are deposited with excess electrons.[44–47] There are several ways the charge buildup could be overcome in our instrument. An electron gun could be used if the instrument was altered for cation study and resulting in a study of neutral clusters. Additional potentials could be added nearby (voltages applied to nearby ion optics) to counteract the potential built up

within the matrix. Co-depositions of oppositely charged ions would also prevent a charge buildup within the matrix. Despite these various ways to overcome a problem of charge buildup, time and resource constraints prevented any immediate alterations to the instrument. Confirmation of successful matrices with absorbing molecules in this instrument would be needed before altering the instrument further.

Consideration of possible analytes that could successfully be introduced in the instrument and deposited in a matrix led to a wide search of candidate gasses, liquids, and solids. Interestingly, very few gasses or liquids absorb in the visible wavelength ranges that were successfully used in the fluorescein trials. Some halogens have absorption peaks in the visible range; however, they are quite detrimental to the other experiments conducted on the instrument by other student so could not be used. Pure liquids are almost all colorless except for a very few with some very harmful health and explosive effects, as well as being rather restricted. Not many solids have vapor pressures sufficiently high enough to be expanded into vacuum and other means of transport into the instrument would be required. The best candidate for a matrix trial appeared to be NO_2.

Nitrogen dioxide is a common pollutant found in car exhaust. Toxic to inhale but readily identified by its odor and brown-orange color, NO_2 is a promising candidate for MICRDS study. A mixing tank (≈2 L in volume) was made with ≈1% NO_2 in SF_6. This mixture was introduced into the deposition chamber until the chamber pressure was raised to between 10^{-4}-10^{-5} Torr. Deposition times varied between 1 and 3 hours or until the mixing tank was empty. After the depositions were completed spectra revealed no change in absorption. The absence of any absorption could be a result of two problems. First,

perhaps the matrix never built up and captured NO_2. Second, at low temperatures (< 290 K), NO_2 dimerizes to form N_2O_4 which is transparent in the visible spectrum. At 1% NO_2 in SF_6 there should be approximately 90% isolation of the NO_2 molecules; however, it could be that the matrix is not sufficiently rigid to prevent the diffusion of NO_2 molecules combining in the matrix and becoming colorless.

After several failed approaches using mixing tanks, it seemed that the best method to test MICRDS would be to introduce a solid into the chamber for deposition. As a means of providing a proof of concept and only a stepping stone on the path to MICRDS of clusters, the changes to the instrument to accommodate solid samples needed to be minimal and reversible if necessary. A group which had previously been consulted about the cavity ring-down chamber provided the inspiration for the next trials. The Freedman group performs CRD experiments on aerosol particles the closely resemble atmospheric conditions. The same process that provided their aerosol particles seemed compatible with this instrumentation with minimal changes to the current setup.

The Freedman group graciously loaned their atomizer (aerosol generator) until a custom atomizer could be built (for details see the appendix). An atomizer uses a small aperture to pressurize a gas which then “atomizes” a solution (Figure 4.11).[48]

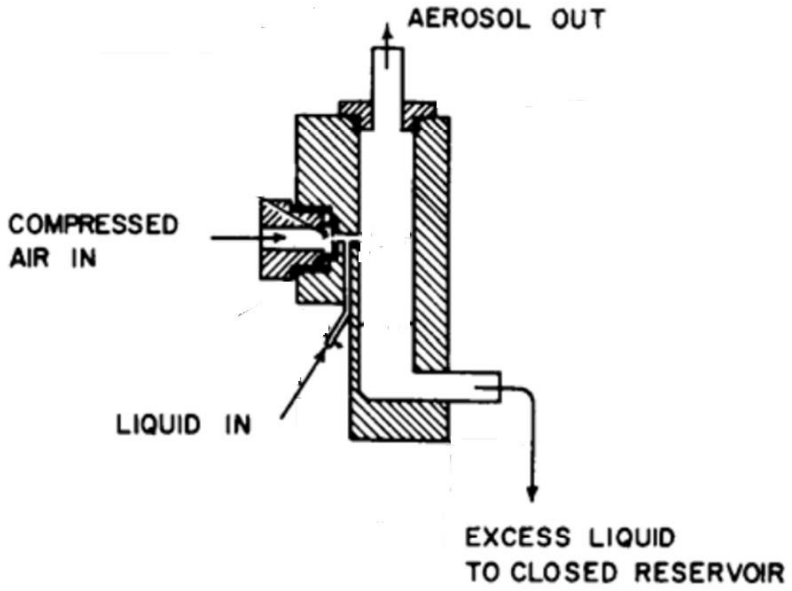

Figure 4.11. Diagram of an atomizer designed by Liu and Lee. The compressed air obliterates droplets of the liquid and then carries aerosol particles into the rest of the system. This design is based on positive pressures and connected to systems with positive pressures. Figure adapted from reference [48].

The aerosol particles are then carried through the rest of the plumbing by the flow of gas. Traditionally, the aerosol particles are sent through dryers which remove any of the solvent from the particles, leaving small nanocrystals.[49] This process seems a perfect method for taking solid samples and introducing them into the vacuum chamber to be deposited. If the drying step is removed, the entire aerosol particle, solute and solvent, can be deposited as matrix and analyte. Water was chosen as the solvent because its melting point was acceptable for the cryogenic temperatures, does not absorb in the visible range, and many possible analyte candidates have high solubility in water. Also, no significant changes were required to the instrument in that the atomizer can be connected directly to the SF_6 inlet shown in Figure 4.7.

The atomizer built followed the general dimensions of that shown in Figure 4.11 but more closely followed the commercial product TSI Aerosol Generator 3076. Small modifications were made to the setup in order to maintain vacuum throughout the system. The custom atomizer was tested using the Freedman group setup to ensure the output of aerosol particles was as expected. Figure 4.12 shows the sized distribution of aerosol particles produced using a flow rate of 1.3 L/m and a 0.04 wt% solution of ammonium sulfate.

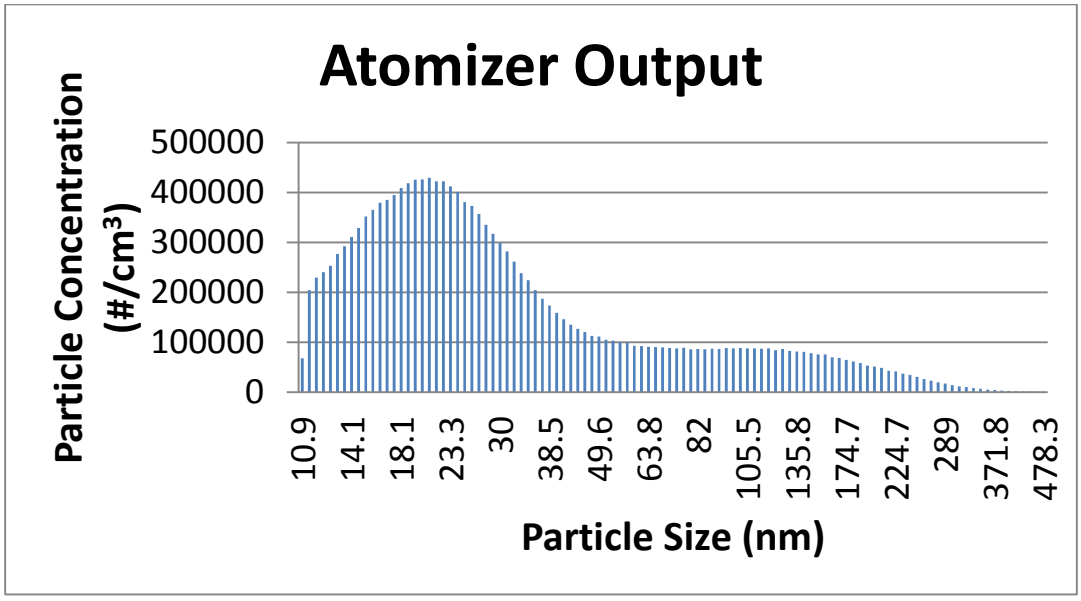

Figure 4.12. A histogram showing the aerosol particle size distribution of the atomizer. The particle concentration numbers are not accurate in an absolute sense, but only relative between particle sizes.

The particle concentration in the figure is not accurate in the absolute scale numbers. Concentration is highly dependent upon flow rate and will be altered when connected to the deposition chamber. The first several aerosol trials were performed using a borrowed

atomizer and the rest using the custom version, but as the two are nearly identical in make and output, the trials will not be differentiated and only the term atomizer will be used.

The aerosol attempts have resulted in inconclusive findings. A solution of nigrosin dye in water was used as the deposition analyte and matrix, respectively. Two trials resulted in discernible absorption spectra for the nigrosin solution. Nigrosin is a black dye composed of multiple constituents. Figure 4.13 shows the absorption spectra obtained for two nigrosin trials.

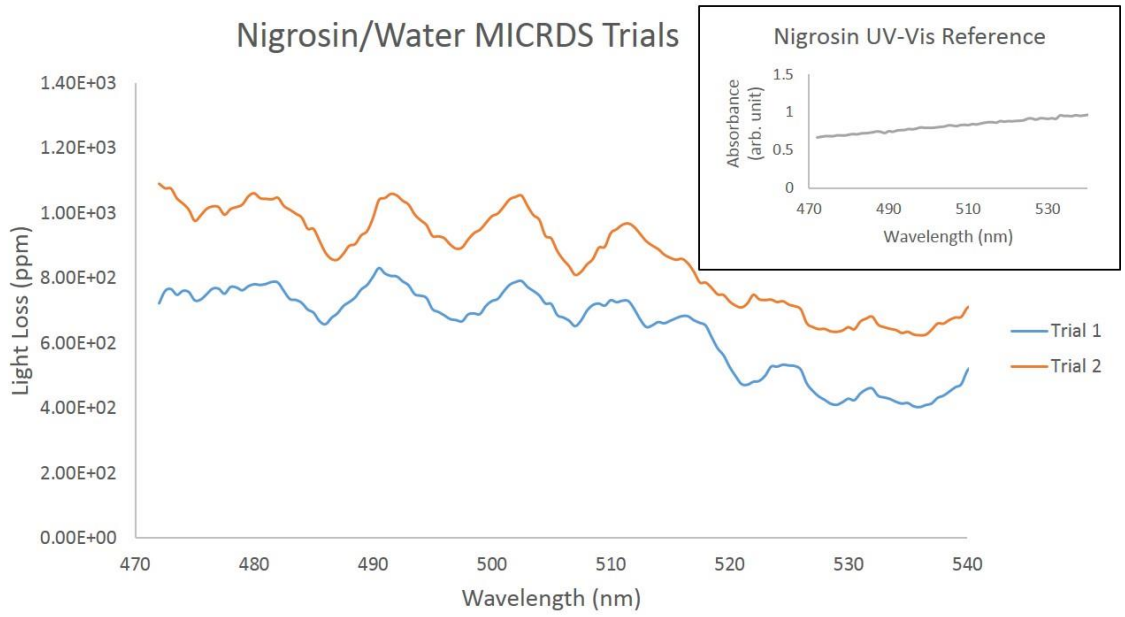

Figure 4.13. MICRDS spectra taken after deposition of nigrosin/water aerosol particles. Both trials match closely; however, they do not match a reference spectrum of a water/nigrosin solution taken by a commercial UV-vis spectrometer (inset).

Both trials resulted in spectra which are nearly identical. The absolute light lost is slightly less for trial 1 which corresponds to a shorter deposition time, only two hours rather than

three for trial 2. The main problem with these results is that it does not match the reference spectrum of nigrosin in water taken with a commercial spectrometer. To better understand the results, the same process was repeated with only water and no other absorbing molecule. Many attempts were made with widely varying results. Figure 4.14 displays the erratic results for two trials.

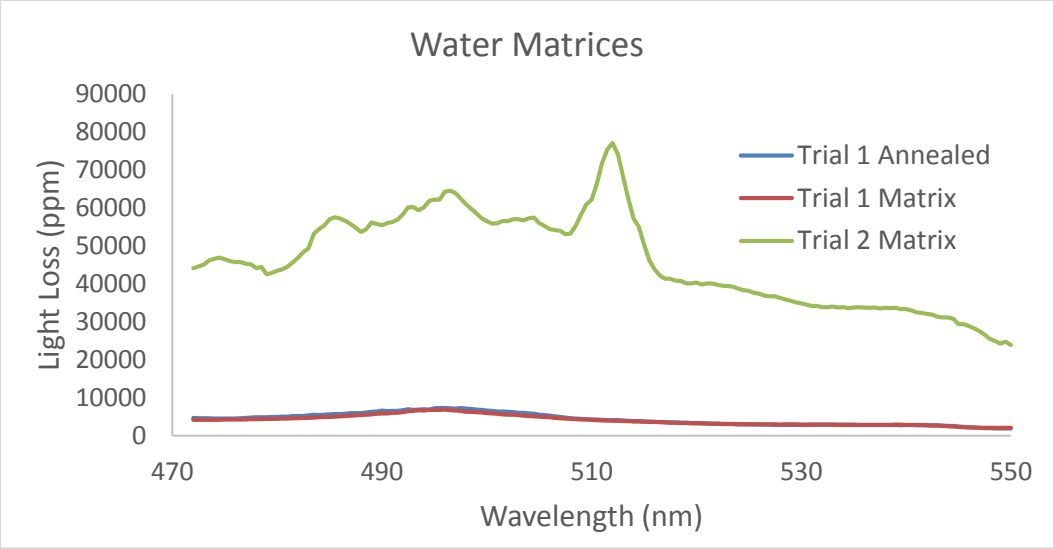

Figure 4.14. Water matrix spectra for two separate trials. Trial 1 includes spectra of the matrix before and after an annealing procedure. The annealing resulted in no significant difference in the spectrum. Notice the difference of one order of magnitude difference in absorption between the two trials.

The absorption differs by an order of magnitude between these two trials. Many water trials were performed with many different results. Some resulted in cloudy matrices that had no recordable ring-down times due to visibly cloudy matrices. No observable benefits arose from altering experimental conditions such as deposition lengths, annealing, and deposition rates. Reproducibility in matrices can be a difficult obstacle. In discussions with other

researchers, one to two years of calibration, trial and error, and modifications were needed to standardize an already proven instrumental setup.[12] Additionally, few matrix isolation instruments are designed for UV-vis wavelengths because of the difficulties involved in obtaining visibly clear matrices.[50–52] The quality of the matrix is one reason that many matrix isolation studies are coupled to FTIR instruments. If the matrix is a noble gas (no vibrations), all signal comes from only the molecules trapped in the matrix and the matrix quality is determined only by how well it separates the trapped species.

The nigrosin MICRDS spectra do not appear to match the reference solution spectrum; however, the matching of the features in the spectra indicate some wavelength dependent process of light loss (absorption) in the matrix. Further studies will help elucidate the meanings behind the nigrosin spectra and how to achieve better reproducibility in matrix depositions.

4.5 Summary and Future of MICRDS

The development of new analytical techniques continues to further the knowledge of molecules, bonding, and interaction. Throughout the development process of MICRDS, many obstacles have been found, and some overcome. The main difficulties that arise from cluster MICRDS seem to be matrix clarity, and the containment of cluster ions in the matrix. Successful studies of neutral clusters in inert matrices have been reported though the real goal of this technique is not simply the study of clusters but the development of cluster assembled materials.[53,54]

MICRDS has great potential in the development of cluster assembled materials because it provides a method to both capture and combine clusters and molecules while observing their interactions spectroscopically. Various other properties could be studied by integrating lamps for photoreactivity studies. The high sensitivity of CRD allows the detections of minute amounts of either the initial material deposited or any species produced through interactions (van der Waals complexes or reaction products). Development of MICRDS could lead to the co-deposition of two or even several different substances and the possible products from their reactions. Co-depositing of different species may lead to a pathway for cluster assembled materials. Cluster salt crystals may be formed from anions and cations deposited in the matrix such as those proposed by Reber et al.[55] The benefits and potential of MICRDS will hopefully encourage other scientists to consider its application in many areas of materials science.

4.6 References

(1) Nacer, B.; Massobrio, C.; Felix, C. Deposition of Metallic Clusters on a Metallic Surface at Zero Initial Kinetic Energy: Evidence for Implantation and Site Exchanges. *Phys. Rev. B* **1997**, *56* (16), 10590–10595.

(2) Nacer, B.; Massobrio, C. Surface Alloying in Cluster Deposition Experiments: Ag/Pd(100). *Comput. Mater. Sci.* **1997**, *8* (1-2), 213–218.

(3) Woodward, W. H.; Blake, M. M.; Luo, Z.; Weiss, P. S.; Castleman Jr., A. W. Soft-Landing Deposition of Al-17(-) on a Hydroxyl-Terminated Self-Assembled Monolayer. *J. Phys. Chem. C* **2011**, *115* (13), 5373–5377.

(4) Vandoni, G.; Felix, C.; Monot, R.; Buttet, J.; Harbich, W. Mass-Selected Deposition of Ag-7 on Pd(100) - Evidence for Implantation and Strong Fragmentation. *Chem. Phys. Lett.* **1994**, *229* (1-2), 51–56.

(5) Cleveland, C.; Landman, U. Dynamics of Cluster-Surface Collisions. *Science* **1992**, *257* (5068), 355–361.

(6) Francis, G. M.; Goldby, I. M.; Kuipers, L.; vonIssendorff, B.; Palmer, R. E. Deposition and Growth of Noble Metal Clusters on Graphite. *J. Chem. Soc.-Dalton Trans.* **1996**, No. 5, 665–671.
(7) Weissler, G. L.; Carlson, R. W. *Methods of Experimental Physics: Vacuum Physics and Technology*; Academic Press, 1979; Vol. 14.
(8) Whittle, E.; Dows, D.; Pimentel, G. Matrix Isolation Method for the Experimental Study of Unstable Species. *J. Chem. Phys.* **1954**, *22* (11), 1943–1943.
(9) Becker, E.; Pimentel, G. Spectroscopic Studies of Reactive Molecules by the Matrix Isolation Method. *J. Chem. Phys.* **1956**, *25* (2), 224–228.
(10) Dunkin, I. R. *Matrix-Isolation Techniques: A Practical Approach*; Oxford University Press, 1998.
(11) Cradock, S.; Hinchcliffe, A. J. *Matrix Isolation: A Technique for the Study of Reactive Inorganic Species*; Cambridge University Press, 1975.
(12) Amicangelo, J. Amicangelo Labratory Visit and Discussion, 2015.
(13) Herbelin, J.; McKay, J.; Kwok, M.; Ueunten, R.; Urevig, D.; Spencer, D.; Benard, D. Sensitive Measurement of Photon Lifetime and True Reflectances in an Optical Cavity by a Phase-Shift Method. *Appl. Opt.* **1980**, *19* (1), 144–147.
(14) Anderson, D.; Frisch, J.; Masser, C. Mirror Reflectometer Based on Optical Cavity Decay Time. *Appl. Opt.* **1984**, *23* (8), 1238–1245.
(15) Namiesnik, J. Trace Analysis - Challenges and Problems. *Crit. Rev. Anal. Chem.* **2002**, *32* (4), 271–300.
(16) Bondybey, V.; English, J. Laser-Induced Fluorescence of Metal-Clusters Produced by Laser Vaporization - Gas-Phase Spectrum of Pb-2. *J. Chem. Phys.* **1981**, *74* (12), 6978–6979.
(17) Liu, Y.; Hu, Z.; Gao, S.; Guenther, D.; Xu, J.; Gao, C.; Chen, H. In Situ Analysis of Major and Trace Elements of Anhydrous Minerals by LA-ICP-MS Without Applying an Internal Standard. *Chem. Geol.* **2008**, *257* (1-2), 34–43.
(18) Simpson, G. J.; Westerbuhr, S. G.; Rowlen, K. L. Molecular Orientation and Angular Distribution Probed by Angle-Resolved Absorbance and Second Harmonic Generation. *Anal. Chem.* **2000**, *72* (5), 887–898.
(19) Luo, Z.; Woodward, W. H.; Castleman Jr., A. W. Distinguishable Behavior of Multiple and Individual Rhodamine-6G Molecules on Spherical Ag Nanoparticles Examined Via Time Dependence of the SERS Spectra. *J. Raman Spectrosc.* **2012**, *43* (12), 1905–1912.
(20) Brown, R. J. C.; Milton, M. J. T. Analytical Techniques for Trace Element Analysis: An Overview. *Trac-Trends Anal. Chem.* **2005**, *24* (3), 266–274.
(21) Okeefe, A.; Scherer, J.; Cooksy, A.; Sheeks, R.; Heath, J.; Saykally, R. Cavity Ring down Dye-Laser Spectroscopy of Jet-Cooled Metal-Clusters - Cu2 and Cu3. *Chem. Phys. Lett.* **1990**, *172* (3-4), 214–218.
(22) Gilb, S.; Hartl, K.; Kartouzian, A.; Peter, J.; Heiz, U.; Boyen, H. G.; Ziemann, P. Cavity Ring-down Spectroscopy of Metallic Gold Nanoparticles. *Eur. Phys. J. D* **2007**, *45* (3), 501–506.
(23) Everest, M. A.; Black, V. M.; Haehlen, A. S.; Haveman, G. A.; Kliewer, C. J.; Neill, H. A. Hemoglobin Adsorption to Silica Monitored with Polarization-Dependent

Evanescent-Wave Cavity Ring-down Spectroscopy. *J. Phys. Chem. B* **2006**, *110* (39), 19461–19468.
(24) Isakina, A. P.; Prokhvatilov, A. I.; Rodriguez-Carvajal, J. Structure and Thermal Expansion of the Low-Temperature Phase of SF6. *Low Temp. Phys.* **2000**, *26* (4), 296–304.
(25) Sasaki, S.; Tomida, Y.; Shimizu, H. High-Pressure Raman-Study of Sulfur-Hexafluoride Up to 10 Gpa. *J. Phys. Soc. Jpn.* **1992**, *61* (2), 514–518.
(26) Ohta, T.; Yamamuro, O.; Suga, H. Heat Capacity and Enthalpy of Sublimation of Sulfur Hexafluoride. *J. Chem. Thermodyn.* **1994**, *26* (3), 319–331.
(27) Pipino, A. C. R.; Woodward, J. T.; Meuse, C. W.; Silin, V. Surface-Plasmon-Resonance-Enhanced Cavity Ring-down Detection. *J. Chem. Phys.* **2004**, *120* (3), 1585–1593.
(28) Antonietti, J. M.; Michalski, M.; Heiz, U.; Jones, H.; Lim, K. H.; Rosch, N.; Del Vitto, A.; Pacchioni, G. Optical Absorption Spectrum of Gold Atoms Deposited on Sio2 from Cavity Ringdown Spectroscopy. *Phys. Rev. Lett.* **2005**, *94* (21), 213402.
(29) Engeln, R.; Berden, G.; vandenBerg, E.; Meijer, G. Polarization Dependent Cavity Ring down Spectroscopy. *J. Chem. Phys.* **1997**, *107* (12), 4458–4467.
(30) Labazan, I.; Krstulovic, N.; Milosevic, S. Laser Vaporization of LiAlH4 Solid Samples. *Chem. Phys. Lett.* **2006**, *428* (1-3), 13–17.
(31) Everest, M. A.; Papadakis, V. M.; Stamataki, K.; Tzortzakis, S.; Loppinet, B.; Rakitzis, T. P. Evanescent-Wave Cavity Ring-Down Ellipsometry. *J. Phys. Chem. Lett.* **2011**, *2* (11), 1324–1327.
(32) Cotirlan-Simioniuc, C.; Ghita, R. V.; Negrila, C. C.; Logofatu, C. The Evanescent-Wave Cavity Ring-down Spectroscopy Technique Applied to the Investigation of Thermally Grown Oxides on Si(100). *Appl. Phys. -Mater. Sci. Process.* **2014**, *117* (3), 1359–1365.
(33) Kartouzian, A.; Thaemer, M.; Heiz, U. Characterisation and Cleaning of Oxide Support Materials for Cavity Ring-down Spectroscopy. *Phys. Status Solidi B-Basic Solid State Phys.* **2010**, *247* (5), 1147–1151.
(34) Egashira, K.; Terasaki, A.; Kondow, T.; Terasaki, A.; Kondow, T. Infrared Spectra of Organic Monolayer Films in a Standing Wave Measured by Photon-Trap Spectroscopy. *J. Chem. Phys.* **2007**, *126* (22), 221102.
(35) Terasaki, A.; Kondow, T. Continuous-Wave Cavity Ringdown Spectroscopy Applied to Solids: Properties of a Fabry-Perot Cavity Containing a Transparent Substrate. *J. Opt. Soc. Am. B-Opt. Phys.* **2005**, *22* (3), 675–686.
(36) Furr, N. How Failure Taught Edison to Repeatedly Innovate. *Forbes*.
(37) Leuchtner, R.; Harms, A.; Castleman Jr., A. Thermal Metal Cluster Anion Reactions - Behavior of Aluminum Clusters with Oxygen. *J. Chem. Phys.* **1989**, *91* (4), 2753–2754.
(38) RUATTA, S.; ANDERSON, S. Reaction of Aluminum Cluster Ions with Oxygen and Nitrous-Oxide - Energetics and Dynamics of Cluster Oxidation. *J. Chem. Phys.* **1988**, *89* (1), 273–286.
(39) Woodward, W. H.; Eyet, N.; Shuman, N. S.; Smith, J. C.; Viggiano, A. A.; Castleman Jr., A. W. Aluminum Cluster Anion Reactivity with Singlet Oxygen: Evidence of Al-9(-) Stability. *J. Phys. Chem. C* **2011**, *115* (20), 9903–9908.

(40) Halliday, D.; Resnick, R.; Walker, J. *Fundamentals of Physics*, 8th ed.; John Wiley and Sons, Ltd: USA, 2008.
(41) Andrews, L.; Kelsall, B.; Blankenship, T. Vibronic Absorption-Spectra of Naphthalene and Substituted Naphthalene Cations in Solid Argon. *J. Phys. Chem.* **1982**, *86* (15), 2916–2926.
(42) Andrews, L.; Keelan, B. Ultraviolet-Absorption Spectra and Photochemical Rearrangements of Benzyl and Tropylium Cations in Solid Argon. *J. Am. Chem. Soc.* **1981**, *103* (1), 99–103.
(43) Andrews, L.; Blankenship, T. Vibronic Spectra of Naphthalene and Naphthalene-D8 Cations in Solid Argon. *J. Am. Chem. Soc.* **1981**, *103* (19), 5977–5979.
(44) Harbich, W. "Soft Landing" of Size-Selected Clusters in Chemically Inert Substrates. *Philos. Mag. B-Phys. Condens. Matter Stat. Mech. Electron. Opt. Magn. Prop.* **1999**, *79* (9), 1307–1320.
(45) Fedrigo, S.; Harbich, W.; Buttet, J. Soft Landing and Fragmentation of Small Clusters Deposited in Noble-Gas Films. *Phys. Rev. B* **1998**, *58* (11), 7428–7433.
(46) Fedrigo, S.; Harbich, W.; Buttet, J. Optical-Response of Ag2, Ag3, Au2, and Au3 in Argon Matrices. *J. Chem. Phys.* **1993**, *99* (8), 5712–5717.
(47) Kartouzian, A.; Thaemer, M.; Soini, T.; Peter, J.; Pitschi, P.; Gilb, S.; Heiz, U. Cavity Ring-down Spectrometer for Measuring the Optical Response of Supported Size-Selected Clusters and Surface Defects in Ultrahigh Vacuum. *J. Appl. Phys.* **2008**, *104* (12), 124313.
(48) Liu, B.; Lee, K. Aerosol Generator of High Stability. *Am. Ind. Hyg. Assoc. J.* **1975**, *36* (12), 861–865.
(49) Veghte, D.; Altaf, M. Aerosol Discussions with Dan Veghte and Muhammad Altaf, 2013.
(50) Kopitzky, R.; Grothe, H.; Willner, H. Chlorine Oxide Radicals ClOx (x=1-4) Studied by Matrix Isolation Spectroscopy. *Chem.- Eur. J.* **2002**, *8* (24), 5601–5621.
(51) Fajardo, M.; Carrick, P.; Kenney, J. Matrix-Isolation Spectroscopy of Metal Atoms Generated by Laser Ablation .1. the Li/Ar, Li/Kr, and Li/Xe Systems. *J. Chem. Phys.* **1991**, *94* (9), 5812–5825.
(52) Goldberg, N.; Lubell, S. R.; Ault, B. S. Matrix Isolation and Theoretical Study of the Photochemical Reaction of CH3CN with CrO2Cl2 and OvCl3. *J. Mol. Struct.* **2005**, *740* (1-3), 125–131.
(53) Kornath, A.; Zoermer, A.; Ludwig, R. Formation of the Magic Cluster Na-8 in Noble Gas Matrixes. *Inorg. Chem.* **2002**, *41* (24), 6206–6210.
(54) Rabin, I.; Schulze, W.; Ertl, G.; Felix, C.; Sieber, C.; Harbich, W.; Buttet, J. Absorption and Fluorescence Spectra of Ar-Matrix-Isolated Ag-3 Clusters. *Chem. Phys. Lett.* **2000**, *320* (1-2), 59–64.
(55) Reber, A. C.; Khanna, S. N.; Castleman Jr., A. W. Superatom Compounds, Clusters, and Assemblies: Ultra Alkali Motifs and Architectures. *J. Am. Chem. Soc.* **2007**, *129* (33), 10189–10194.

Chapter 5

Conclusions and Future Outlook

The work recorded in this dissertation has focused on two goals: gaining a better understanding of aluminum cluster anion reactivity, and developing a new analytical technique (MICRDS) to bridge the gap between gas phase studies and condensed phase materials. Chapter 3 discusses the effects of doping aluminum cluster anions with boron atoms. In the same group as aluminum, boron is slightly smaller and was most often located in the center of the cluster surrounded by aluminum atoms. The central position of the boron allowed the clusters to relax into a more stable geometry. The changes to the reactivity or stability of the cluster due to the boron doping was almost entirely affected by changes in the cluster geometry which could lead to changes in the electronic structure of the clusters (e.g. $Al_{14}B^-$). In Chapter 4, the development of cluster matrix isolation cavity-ring down spectroscopy was detailed. Charge buildup due to accumulation of ions presents a significant barrier to the study of cluster ions unless other measures are taken to offset the charge buildup. Matrix clarity also presented a significant obstacle for UV-vis spectra. The quality of the matrix varied between trials some resulting in little to no light scatter and others with enough light scatter to prevent any observable signal. The potential remains for this technique to enhance our understanding of clusters with continued progress.

Throughout history the understanding of smaller scales has led to great advancement in society. From raising the standard of living with commercial products to saving lives with new medicines, nanotechnology has changed the way we live. Cluster

science is the next frontier of smaller scales, going from nanoparticles with thousands or millions of atoms, to less than 50. The ability to tailor the properties of materials through cluster assembly motivates many researchers in the cluster field.

The abundant information and knowledge that has been gained through the study of clusters is far from complete. Great strides have been made and continue to be made regarding the chemistry of clusters and their applications in materials. The future of cluster studies will most likely take a two-fold approach. First, the identification of clusters with advantageous properties for use in new materials must continue, using both experimental and theoretical methods. Accurate theoretical models and methods of predicting suitable clusters will facilitate identifying clusters with the most potential. Second, the development of techniques and methods that will provide the means to combine clusters into larger assemblies and eventually into bulk material with tailored properties. As the understanding of cluster chemistry expands, new materials with applications in catalysis, energy, optics, and more will emerge.

Appendix

Custom Equipment

A.1. Mirror Mount Exchanger

CRDS generally is set up for use for only a single wavelength. Full absorption spectra are only possible with the use of multiple sets of mirrors. Mirror reflectivity for CRDS generally ranges from 99.95-99.9985% depending on the specific coatings on the mirrors. The dielectric coatings used to achieve such high reflectivities are specific to a certain wavelength of light and the reflectivity diminishes according to Figure A.1 as the wavelength used deviates from the center wavelength[1].

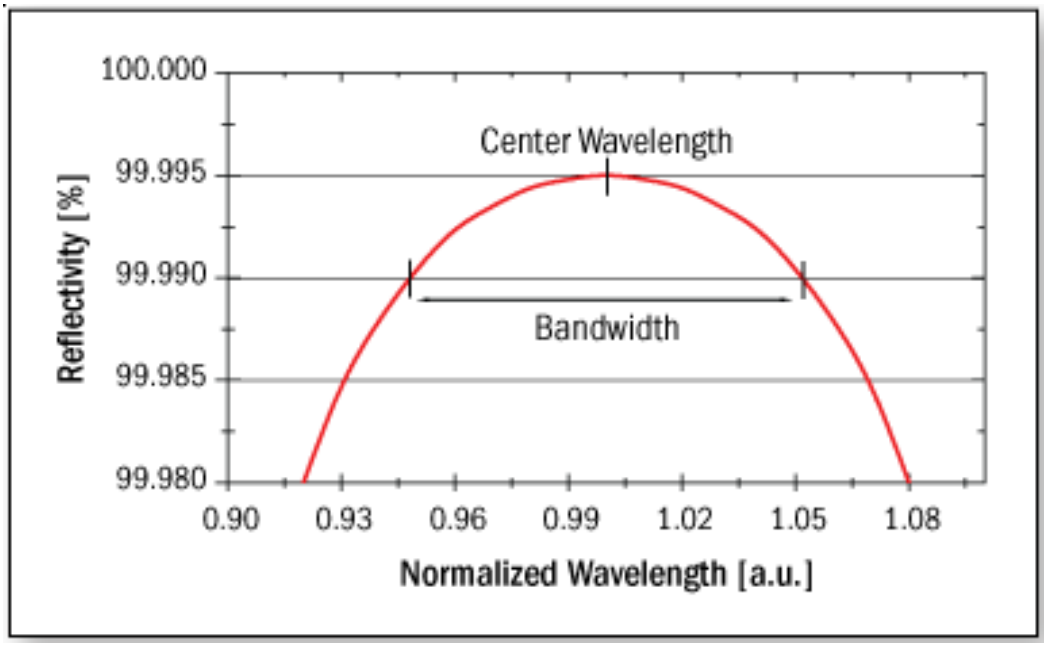

Figure A.1. The wavelength dependent reflectivity of cavity ring-down mirrors. The acceptable range will vary based on the specific dielectric coatings. Figure reprinted from reference [1].

Some sets of mirrors only maintain high reflectivities for a range of 40 nm while other sets may be useful for up to 100 nm.

The original mirror mounts used for the CRD instrument described in Chapter 4 were designed by William Woodward.[2] The mounts held one mirror each and were aligned using high strength rare-earth magnets that were coupled on the atmosphere and vacuum sides of a flange. The distance between mirrors is an important parameter in CRDS and Gimbal-style mounts are required to maintain the exact same distance between the mirrors regardless of any alignment changes. The mounts were only just sufficient and the two issues that necessitated the new mounts were 1) the mounts only held one mirror each, and 2) the coupling between the magnets often failed resulting in the need to vent the instrument and reset the mirror mount. Needless to say that anytime a high-vacuum instrument must be vented when not absolutely necessary is cause for concern.

For any CRD spectrum to have a range of greater than 100 nm, multiple sets of mirrors must be used. This presents a problem for vacuum instruments, as changing physical positions of objects within a steel chamber under vacuum can be quite difficult unless the instrument is vented. In the search to find such a mechanism, the work of Aran Kartouzian seemed to solve the problem. Kartouzian had a similar desire to use CRD in high-vacuum and achieve extended spectroscopic ranges. The design drawings are available in his doctoral thesis and are the foundation upon which the designs in this work

were built.[3,4] Two issues with the Kartouzian design prevented the use of his work. First, an individual mirror alignment is not possible while under vacuum. A course alignment of each mirror is provided before the instrument is pumped to vacuum. Once under vacuum, the alignment is optimized using two vacuum feedthroughs that adjust the plane of a disk plate onto which all the mirrors are attached. This alignment process leads to the second issue. If the plane of the disk is altered to provide fine adjustments in the alignment, the distance between each mirror set may be slightly different and different alignments of the same set of mirrors might result in a changing distance between the CRD mirrors.

Consulting with the Penn State Physics Machine Shop, a new design was built using concepts from both Kartouzian and Woodward. This design holds nine sets of mirrors compared to the 10 sets in the Kartouzian and 1 set in the Woodward designs and each is separately aligned in its own Gimbal-style mount that maintains the exact same distance between the sets of mirrors. The design consists of a disk plate (Figure A.2) onto which two sets of wedges (Figures A.3-5) (the wedge adjacent to the disk plate termed the sub-wedge and the wedge on top termed the wedge) are attached using springs. The flange onto which everything is mounted is shown in Figure A.6.

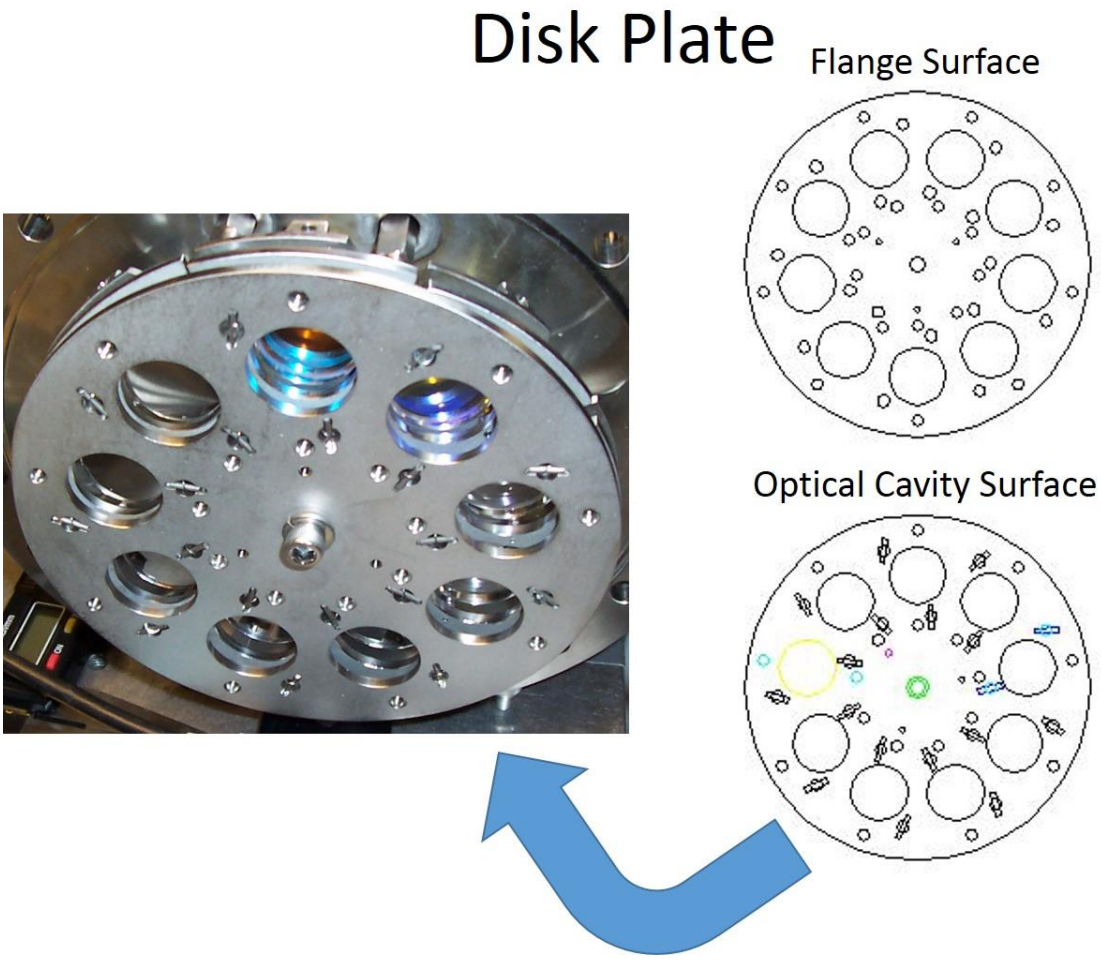

Figure A.2. A photograph and CAD drawings of the disk plate. The large circular holes are to accommodate the optical paths through the cavity. The smaller holes are for the ball bearing and spring assemblies. The springs are held in place by small rods that are placed in the rectangular insets in some of the smaller holes. The central hole is to attach the disk plate to the rotation vacuum feedthrough to enable cycling through the different mirrors.

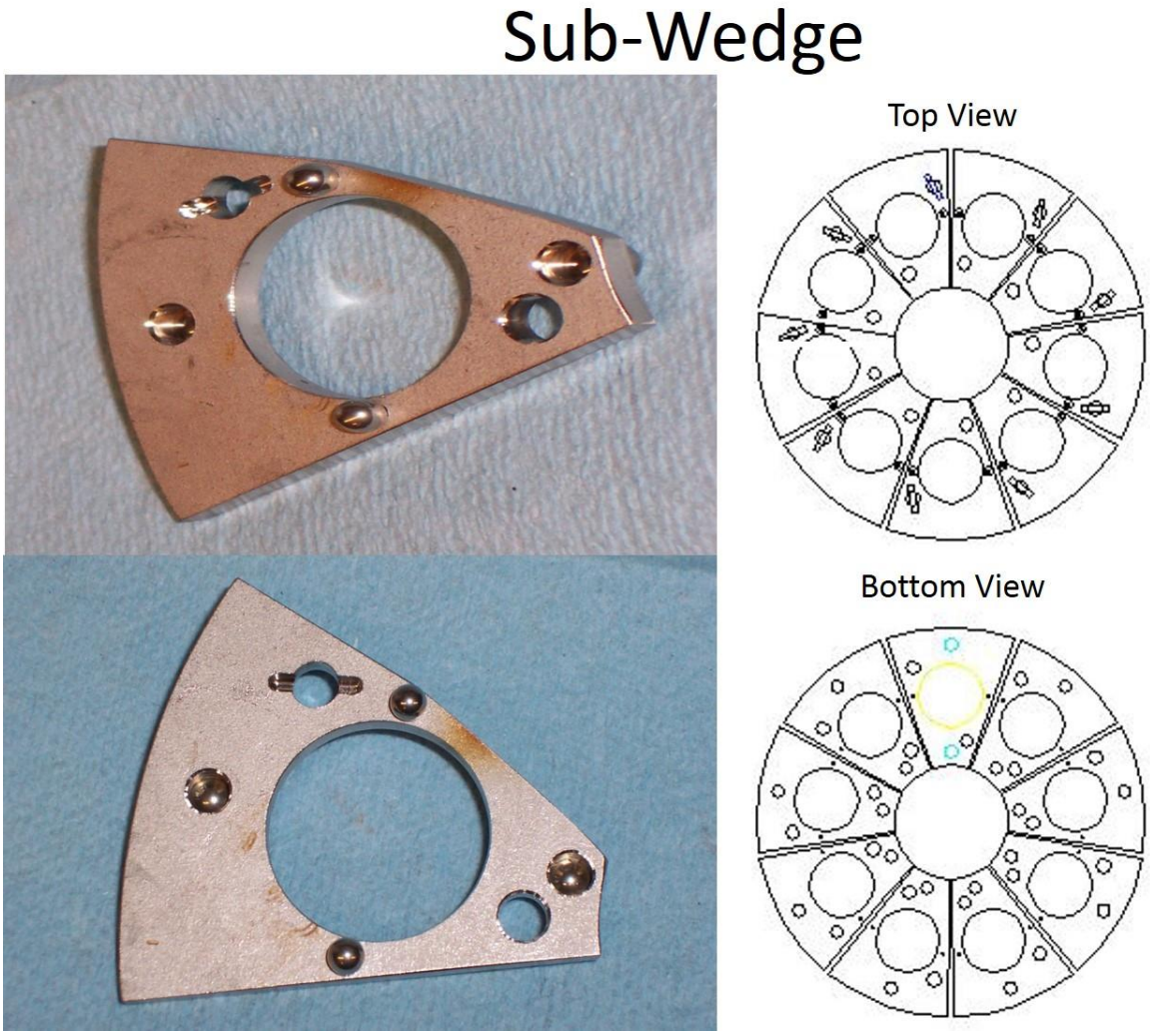

Figure A.3. Photographs and CAD drawings of the sub-wedge. The purpose of the sub-wedge is the alignment of the x-axis of the mirrors. Two ball bearings centered on the vertical axis separate this from the disk plate. Only one spring is needed to hold the sub-wedge to the disk plate and is placed in the hole with the rectangular cutaway (used for the rod which holds the spring).

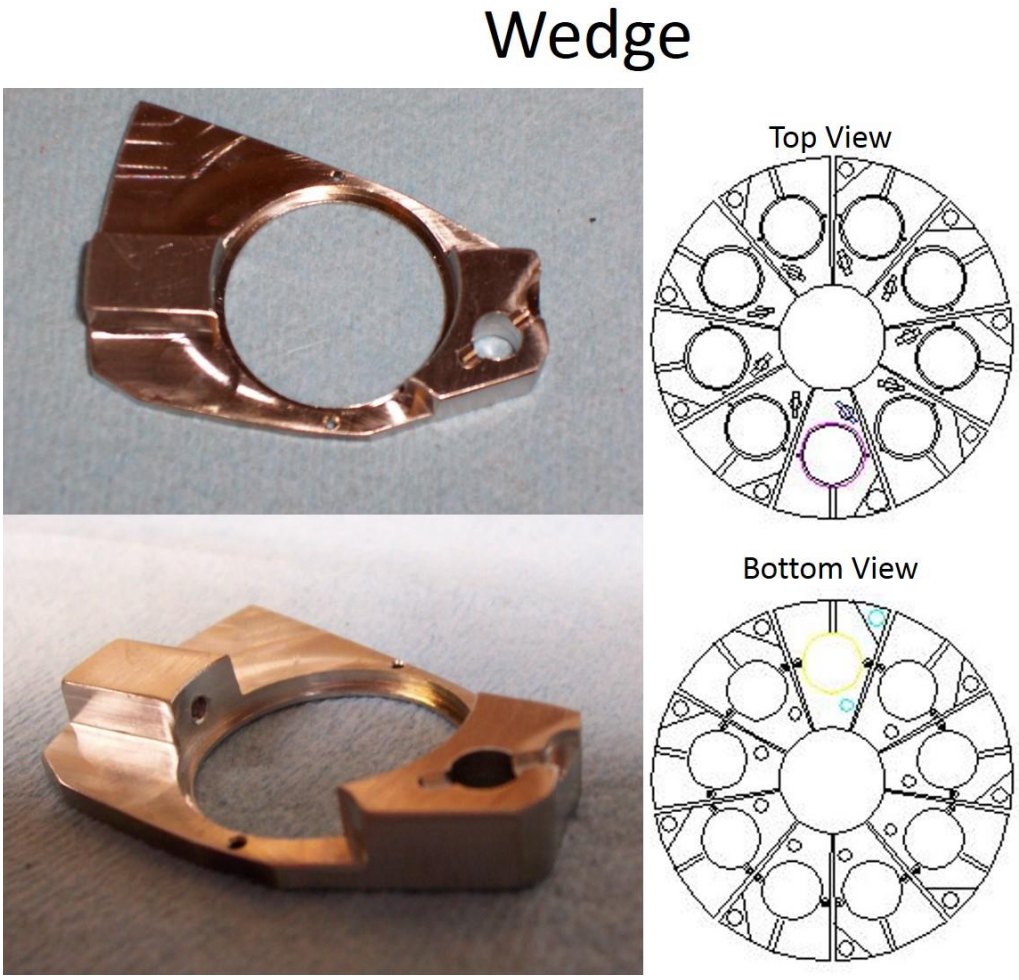

Figure A.4. Photographs and CAD drawings of the wedge. The purpose of the wedge is the alignment of the y-axis and holding of the mirrors. Two ball bearings centered on the horizontal axis separate this from the sub-wedge. Only one spring is needed to hold the wedge to the disk plate and is placed in the hole with the rectangular cutaway (used for the rod which holds the spring). This piece was initially too heavy for the spring which required the removal of excess material. The removal of the bottom right corner is to allow the rod which aligns the sub-wedge to pass without affecting the wedge.

Figure A.5. Photographs of the wedge/sub-wedge assembly simply to show how the pieces are coupled.

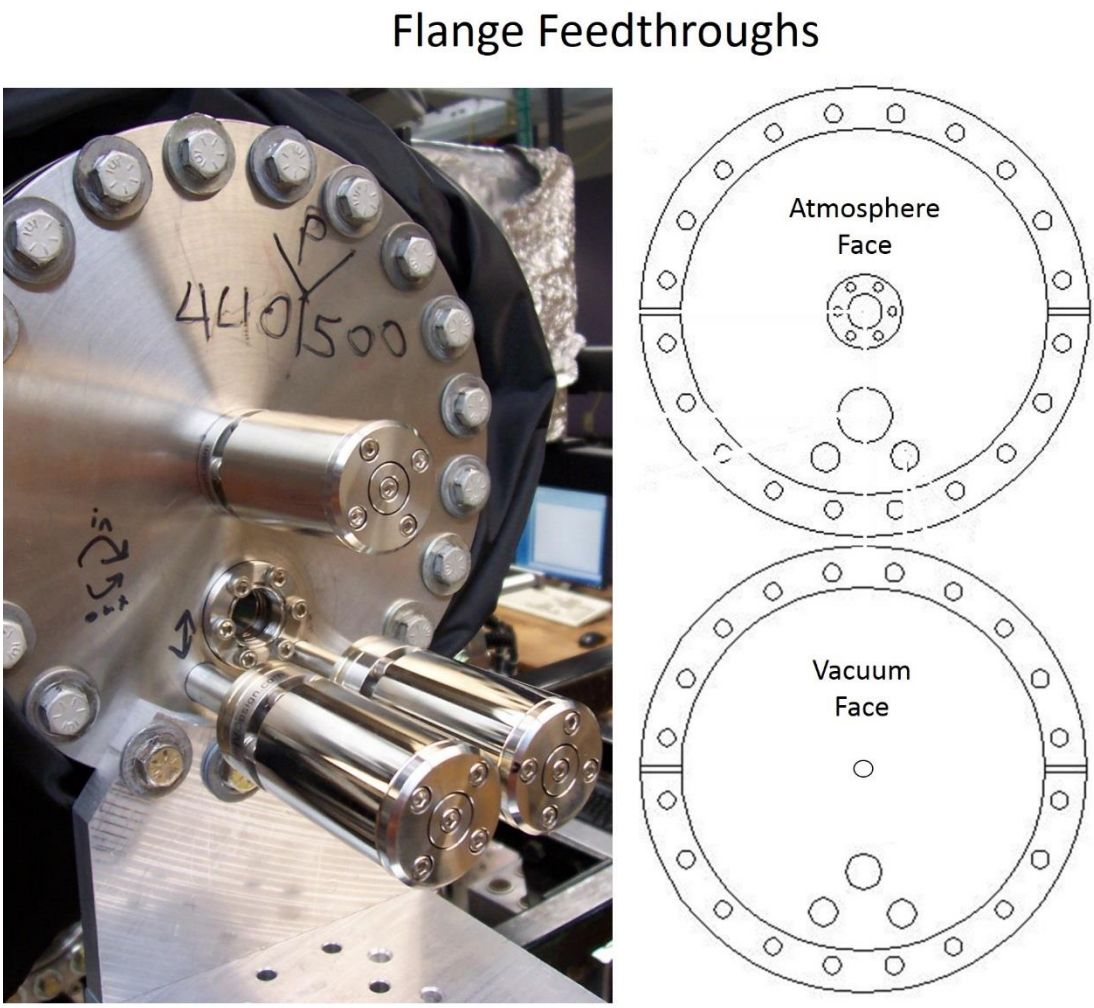

Figure A.6. A photograph and CAD drawings of the flange onto which the whole mirror mount assembly is connected. The central feedthrough provides the rotation of the disk plate to cycle through the mirrors. The other two feedthroughs (side by side) are the alignment mechanisms. A cylinder of stainless steel created extra distance between the feedthroughs and the disk plate to allow sufficient space for the threaded rod assembly to push and release the wedges/sub-wedges. The rods must be completely withdrawn before switching mirrors or they will displace the wedges and a venting of the instrument will be necessary.

Ball bearings are used to separate the sub-wedge from the disk plate and the wedges from the sub-wedges. The wedge and sub-wedge are necessary to form the Gimbal-style mount and allow alignment of each axis independent of the other. Each wedge piece holds a mirror. This entire assembly is attached at the center to a rod which is controlled by a rotation vacuum feedthrough (Kurt J. Lesker MD16TX000Z) which rotates the disk plate and positions each mirror in front of the optical window in the 8" flange. Two other rotation vacuum feedthroughs are attached to each flange and provide the alignment of each mirror by pushing or releasing on the wedge and sub-wedges. The rotation of the feedthrough is converted to translation of a rod using a threaded assembly where a rotating male thread with push and pull a female threaded square rod which is not allowed to rotate. This is the same process and design found in many vacuum systems with flow control such as Schlenk lines and vacuum bubblers. All components and pieces are made from 316 grad stainless steel for structural and vacuum integrity. Slight modifications were made to the wedges after they were built because the mass of the wedge overcame the strength of the spring when the assembly was placed vertically. Excess stainless steel was removed to reduce the mass until the springs were sufficient to hold the wedges in place.

The mirror mounts have worked well and saved weeks if not months of needless instrument venting and pumping down time. There remains one issue that had infinite resources been available at the time of design would make the mounts easier. Because the mirror wedges are aligned using rods that push and release, one axis is completely independent of the other but the other will inevitably adjust both axes as pushing or

releasing the sub-wedge will result in a change of position of the wedge. No economically feasible solution was found to solve this problem, though with enough money it would be a trivial issue. The only benefit this solution would cause is an easier alignment procedure. However, as the current alignment rarely takes no more than 30 minutes from scratch or 5 minutes between switching mirror sets, there is little room to insist on a solution.

The results of using the mirror exchanger for two sets of mirrors (440 nm and 500 nm) are shown in Figure A.7.

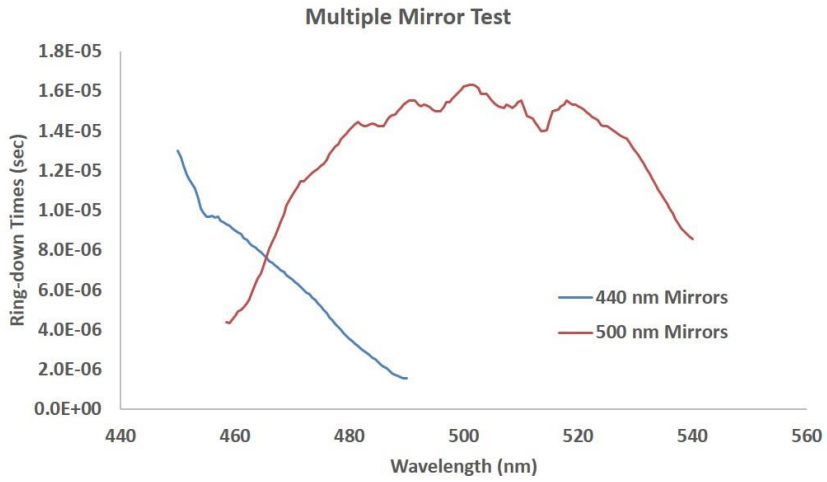

Figure A.7. Ring-down spectra using two sets of mirrors (440 nm-blue, 500 nm-red). The general trend of the signal matches that provided by the manufacturer (CRD Optics) in Figure A.1.

The ring-down times shown here are only to show the overlap between different sets of mirrors. The true ring-down times and thus the sensitivity of the instrument have since increased to near 60 μsec for 500 nm. Additionally, one wedge in the assembly was used

to hold a pin hole rather than a mirror to ensure that the laser passed through the center of both mirrors for optimal alignment.

A.2. Atomizer

As discussed in Chapter 4, a custom atomizer was built according to the specifications in Figure 4.11 and dimensions taken from a TSI Aerosol Generator 3076.[5] Included in this section are the drawings associated with the construction of the atomizer (Figure A.8). These drawings do not represent new designs or ideas but only to provide a detailed description of the atomizer used.

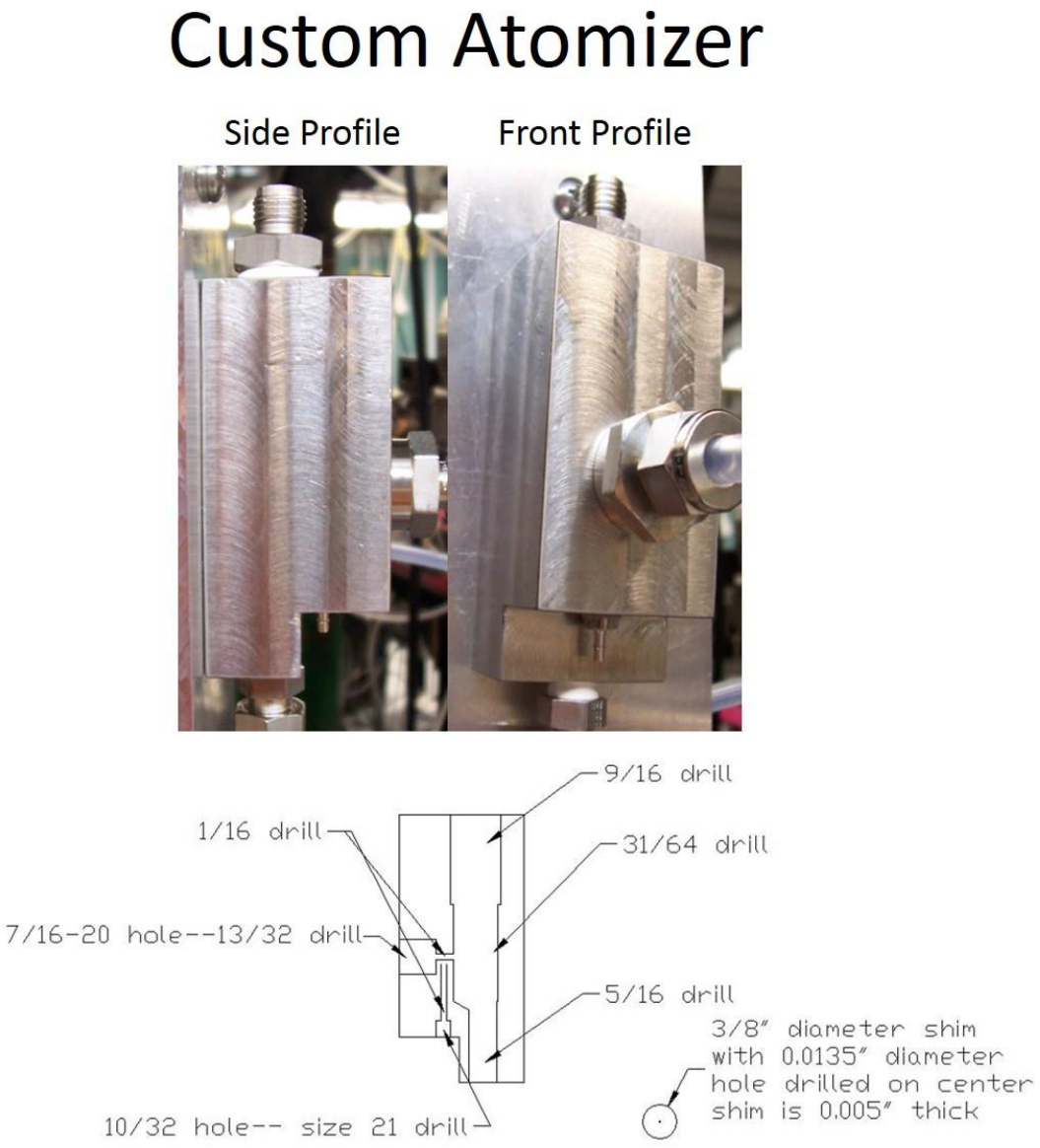

Figure A.8. Photographs and a CAD drawing of the aerosol atomizer. The 3/8" shim depicted in the CAD drawings is placed in the "7/16-20" opening to restrict the gas flow and increase the gas pressure.

A.3. References

(1) CRD Optics, Inc. CRD Mirror Reflectivity.
(2) Woodward, W. H. H. Aluminum Cluster Anion Reactivity: Applications in Energetic Materials and Catalysis. PhD Dissertation, The Pennsylvania State University: University Park, PA, 2011.
(3) Kartouzian, A. Optical Properties of Size-Selected Supported Metal Clusters Measured by Cavity Ring-down Spectroscopy. PhD Dissertation, Technische Universitat Munchen: Munich, Germany, 2010.
(4) Kartouzian, A.; Thaemer, M.; Soini, T.; Peter, J.; Pitschi, P.; Gilb, S.; Heiz, U. Cavity Ring-down Spectrometer for Measuring the Optical Response of Supported Size-Selected Clusters and Surface Defects in Ultrahigh Vacuum. *J. Appl. Phys.* **2008**, *104* (12), 124313.
(5) TSI Particle Instruments. Model 3076 Constant Output Atomizer, Instruction Manual, 2005.

Vita

Jordan Cesar Smith was born in Tomball, Texas on December 28, 1984. Within a year, his family moved to Burke, Virginia and then continued on to San Salvador, El Salvador; Inverness, Florida; Johannesburg, South Africa; and lastly to Naples, Florida where he attended Barron Collier High School, graduating in May 2003. He attended Brigham Young University, Provo for one year and then served as a missionary for the Church of Jesus Christ of Latter-day Saints in Tempe, Arizona for two years. He returned to BYU following his mission in 2006 and graduated with a Bachelor of Science in Chemistry and was married to Jennifer Laub in April of 2009. He began his graduate work at The Pennsylvania State University in August of 2009, where he joined the research group of A. W. Castleman Jr. and worked directly alongside Dr. William H. H. Woodward and Dr. Zhi-Xun Luo. During his time at Penn State he was blessed by the birth of two children: Tanner E. Smith and Alexander N. Smith and at the time of this writing is expecting a third child.